PHOTOSYNTHESIS AND HYPEROXIA

By

Christopher Collin Hall

A DISSERTATION

Submitted to
Michigan State University
in partial fulfillment of the requirements
for the degree of

Plant Biology—Doctor of Philosophy

2017

ABSTRACT

PHOTOSYNTHESIS AND HYPEROXIA

By

Christopher Collin Hall

Plants and algae in nature perform photosynthesis in a dynamically fluctuating environment, yet most mechanistic studies of photosynthesis take place in a static laboratory environment. Laboratory tools capable of simulating nature-like environments are required to identify the mechanisms which confer robustness to photosynthesis. To this end, I present three technologies for measuring photosynthesis in a simulated environment. The IDEA spectrophotometer provides detailed fluorometric and spectrophotometric measurements of individual plant leaves. The DEPI chamber cultivates small plants such as *Arabidopsis thaliana* in a reproducible simulated environment while simultaneously monitoring their photosynthesis by fluorescence image analysis. The ePBR cultivates microalgae in a simulated production pond environment.

These tools were employed to examine the mechanisms of hyperoxia sensitivity in an algal production pond setting. Such ponds are supplemented with mineral nutrients and CO_2 to maximize photosynthetic productivity. The high rates of day-time photosynthesis in these ponds inevitably leads to the accumulation of dissolved O_2 to hyperoxia, which inhibits the photosynthetic growth and productivity of algae despite the CO_2 supplementation. Using the ePBRs, I identified hyperoxia tolerant and sensitive strains of *Chlamydomonas reinhardtii* and compared their photosynthetic efficiencies in normoxia and hyperoxia ePBR cultivation. Photorespiration is often cited as a mechanism of hyperoxia sensitivity in algae, yet the hyperoxia sensitive strain was less prone to photorespiration than the tolerant strain and overall rates of photorespiratory glycolate production amounted to only a small fraction of the total light-dependent oxygen consumption observed in the sensitive strain. This indicates that the hyperoxia sensitive strain is diverting a larger fraction of its photosynthetic electron flux to the reduction of oxygen, possibly via the Mehler cycle or flavodiiron proteins. There also appears to be a trade-off between hyperoxia tolerance and low-CO_2 performance, in which case algae strain selection strategies based on maximum performance under air cultivation may be unintentionally selecting against pond hyperoxia performance.

This dissertation is dedicated to Irma Young, whose determination to pursue her dreams in spite of what was expected of her taught me to never be afraid of the pursuit of my own dreams.

ACKNOWLEDGEMENTS

IDEA spectrophotometer development team:

David Kramer, Jeffrey Cruz, Robert Zegarac, Christopher Hall, Ben F. Lucker, Magnus Wood

ePBR development team:

David Kramer, Robert Zegarac, Ben F. Lucker, Christopher Hall, Casey Abernathy, Joel Carpenter, Jeffrey Cruz

DEPI development team:

David Kramer, Jeffrey Cruz, Robert Zegarac, Christopher Hall, William Kent Kovac, Nathan Galbreath, William Norman, Oliver Tessmer, Lee Wang, Linda Savage, David Hall

Team Algae laboratory technicians:

Joshua Temple, Jacob Bibik, Joyce Goodluck, Liam Parsons, Kip Andrews

Special thanks to Quentin Béchet of Massey University for offering to model a hypothetical algal production pond in Altus, Oklahoma. Thanks also to Ivan Baxter of the Donald Danforth Plant Science Center for lending his NAP10 strain of *Chlamydomonas reinhardtii*.

A very special thanks to Professor David Kramer and to the other members of my PhD guidance committee: Professor Beronda Montgomery, Professor Yair Shachar-Hill, and Professor Christoph Benning.

A very personal thanks to Dr. Ben F. Lucker for encouraging words and constructive criticism.

TABLE OF CONTENTS

LIST OF TABLES

LIST OF FIGURES

KEY TO ABBREVIATIONS

AFDW	ash-free dry weight
AOA	O-(Carboxymethyl)hydroxylamine, also known as amino-oxyacetate
ATP	adenosine triphosphate
CCM	carbon concentrating mechanism
CEF	cyclic electron flux
Ci	inorganic carbon
CPC	compound parabolic concentrator
DEPI	dynmic environment photosynthesis imager
DIRK	dark interval relaxation kinetic
DNA	deoxyribonucleic acid
DOFS	diffused optics flash spectrophotometer
E-TADA	Ethernet-enabled Timing and Data Acquisition device
ECS	electrochromic shift
ePBR	environmental simulation photobioreactor
Fd	ferredoxin
$F_{\_}$	chlorophyll fluorescence intensity of a sample (note that _ represents a one-letter abbreviation of a particular condition when the measurement was taken)
FPGA	field-programmable gate array
G	generic constant
gH^+	conductivity (inverse resistance) of the thylakoid membrane to proton flux
GUI	graphical user interface
H^+	hydrogen or hydronium ions
HS medium	Sueoka's high salt medium
JSON	JavaScript object notation
LED	light emitting diode
LEF	linear electron flux
MB	megabytes

NADP+	nicotinamide adenine dinucleotide phosphate, oxidized
NADPH	nicotinamide adenine dinucleotide phosphate, reduced
NoFoSpec	non-focusing optics spectrophotometer
NPQ	non-photoreductive quenching
$NPQ_{(T)}$	non-photoreductive quenching calculated using a theoretical FV/FM value
PAM	pulse amplitude modulation
PAR	potosynthetically active radiation
pmf	proton motive force
ppm	parts per million
PQ	plastoquinone and/or plastoquinol
PSI	photosystem I
PSII	photosystem II
q_E	reversible component of non-photoreductive quenching
q_I	irreversible component of non-photoreductive quenching
q_L	fraction of photosystem II centers able to perform charge separation
ROS	reactive oxygen species
RPM	revolutions per minute
SNP	single-nucleotide polymorphism
UV	ultraviolet
vH^+	rate of proton flux through the thylakoid membrane
ΔpH	difference in pH across the thylakoid membrane
$\Delta\psi$	electric field across the thylakoid membrane
Φ_{II}	quantum yield of the photosystem II complexes in a sample

INTRODUCTION

The process of oxygenic photosynthesis captures light energy to assimilate inorganic carbon from the organism's environment. Conceptually, this process is divided into two interdependent sub-processes: the dark reactions and the light reactions. The dark reactions include the uptake of CO_2 by the ribulose-1,5-bisphosphate carboxylase/oxygenase enzyme (rubisco) and the regeneration of ribulose-1,5-bisphosphate via the Calvin-Benson cycle (see Michelet et al. 2013 for a comprehensive review of the dark reactions). The necessary NADPH and ATP for the Calvin-Benson cycle are supplied by the light reactions, wherein the photosystems utilize captured light energy to drive the thylakoid electron transport chain, reducing $NADP^+$ to NADPH. This transfer of electrons is coupled to the translocation of protons (H^+) from the chloroplast stroma into the lumen. The resulting H^+ flux builds a proton motive force (*pmf*), which drives ATP synthesis (see Blankenship 2002 for a detailed review).

In this work, I am primarily interested in measuring the light reactions of photosynthesis as a plant or alga responds to changes in its environment. These processes determine the overall energy input to photosynthesis, setting the upper limit for all downstream photosynthetic processes (as discussed in Ort & Melis 2011). However, the light reactions are prone to producing toxic reactive oxygen species, especially when the NADPH and ATP production by the light reactions does not match the demand from the dark reactions (Sharma *et al.* 2012). These constraints make photosynthetic organisms sensitive to environmental fluctuations, and the response of the organism to such fluctuations may be more important to photosynthetic productivity than its performance in any particular steady-state (as discussed in Suorsa et al. 2012 and Davis et al. 2016).

Here I present an introduction to fluorometric and spectrophotometric techniques for measuring the light reactions of photosynthesis, followed by three technologies which I developed for conducting these measurements in a simulated fluctuating environment, and finally I present my results from using these tools and techniques to determine how a hyperoxic environment challenges photosynthesis in the model alga *Chlamydomonas reinhardtii*.

A Review of Photometric Measurements of Photosynthesis

The discovery of plant chlorophyll fluorescence was made some time in the 19th century (not long after the discovery of the phenomenon of fluorescence itself), but the first detailed report of variable fluorescence in plants was made by Kautsky & Hirsch (1931). They reported that shining a bright light onto a plant caused the fluorescence to quickly increase and then slowly decrease to a steady state. This phenomenon came to be known as "the Kautsky effect" and later research would identify several features in the fluorescence signal that could be

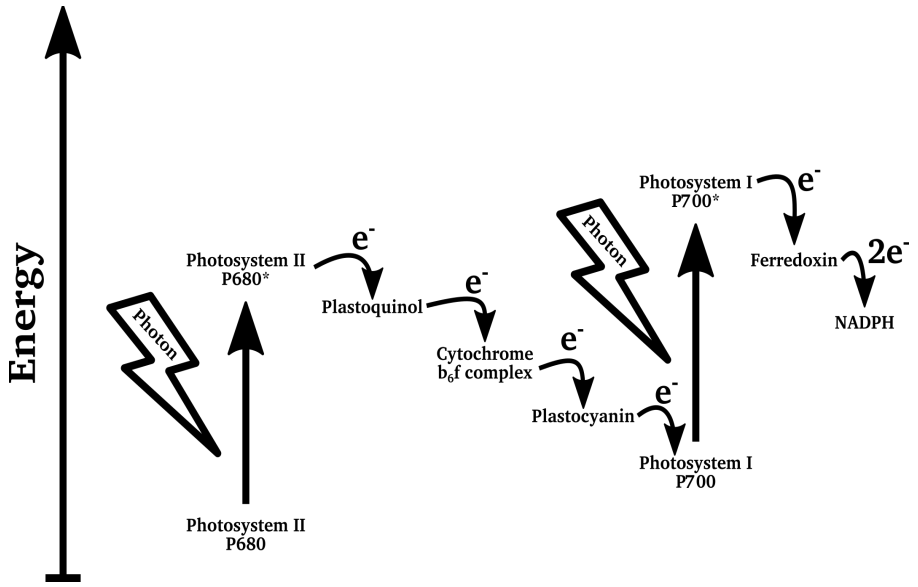

Figure 1: Z-Scheme model of photosynthesis. *The height of state in this electron transport chain is roughly proportional to its midpoint potential, which dictates the amount of potential energy stored in that state relative to the transfer of electrons through the chain. Curved arrows represent the transfer of electrons and the vertical arrows by each photosystem represent the change in energy from the ground state to the excited state caused by the absorption of a photon of light.*

attributed to different aspects of photosynthesis (as reviewed in Govindjee 1995 and Stirbet & Govindjee 2011).

The Light Reactions of Photosynthesis in Plants and Algae

When a molecule absorbs a photon of light energy, the laws of thermodynamics demand that the absorbed energy must go somewhere (the energy cannot be destroyed or otherwise disappear). For most non-fluorescing molecules, the absorbed energy is simply converted to heat. Some molecules can also dissipate the energy by emitting a photon whose energy is equal to the energy state difference between the energized state (called the "excited state") and the relaxed state (called the "ground state"). This mode of photon emission is called "fluorescence" (Valeur 2001). In a photochemical reaction, the absorbed light energy may also be dissipated by changing a chemical bond or transferring an electron to another molecule. Chlorophyll is a molecule that can do all three of these things and the competition between these three fates (heat, fluorescence, and photochemistry) determines the probability of each event occurring after a chlorophyll molecule absorbs a photon of light (Kitajima & Butler 1975).

In the photosystems of a chloroplast, chlorophyll molecules play a key role in photon absorption, photochemistry, and fluorescent emission. From a thermodynamic perspective, the light reactions of photosynthesis can be represented as a series of electron transfer reactions that cascade from the excited states of the photosystems

through several intermediate electron carriers to a carrier molecule that functions to shuttle the energy to where it is needed (for a detailed review, see Whitmarsh & Govindjee 1999 and Rochaix 2011). This depiction (Figure 1) of the light reactions as a cascade of energy states between the two photosystems is known as the Z-Scheme model of photosynthesis (Hill & Bendall 1960) because the energy boosts provided by the light-induced excitation of the photosystem reaction centers and the transfer chain between them form a sideways letter "Z" on the energy diagram. Note that the diagram in Figure 1 has been simplified for clarity and that there are many opportunities in this chain of events for non-productive or even destructive side reactions (e.g. triplet chlorophyll formation), the consequences of which will be discussed later in this chapter.

In the Z-Scheme model of photosynthesis, the thylakoid electron transport chain (diagrammed in Figure 2) is initiated by the excitation of the P680 chlorophylls in photosystem II (PSII) to the excited P680* state (typically from exciton energy that was transferred to the reaction center from the chlorophylls in the neighboring light harvesting proteins). From the P680* excited state, the energy can either be dissipated by conversion to heat, fluorescence emission, or donating an electron to the pheophytin molecule in the protein complex (charge separation), which quickly transfers the electron to the Q_A quinone. After donating an electron, $P680^+$ then pulls an

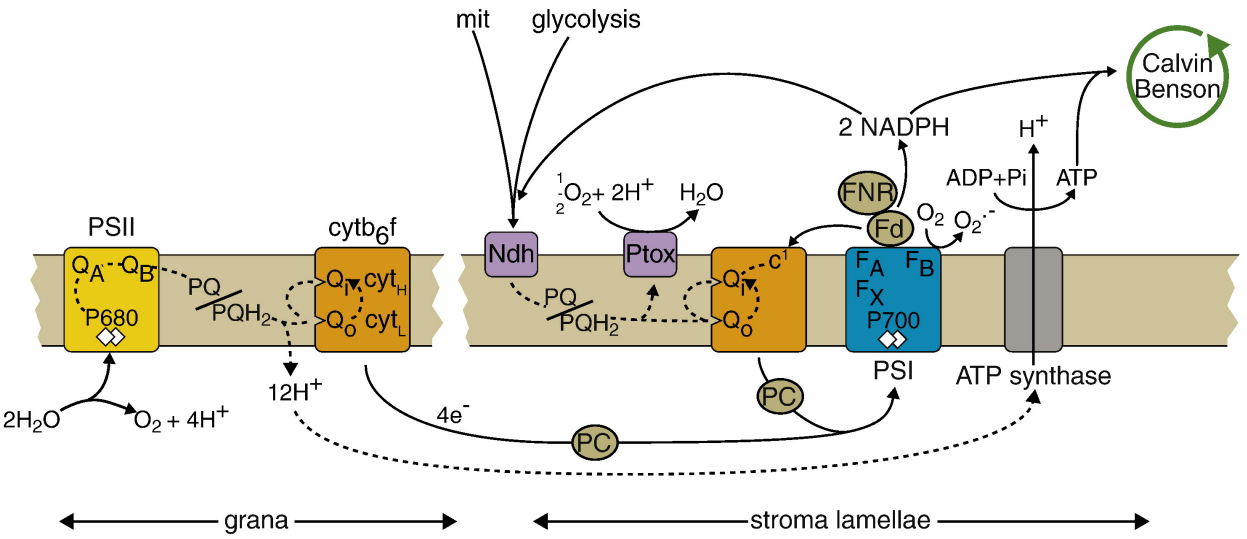

Figure 2: Diagram of the chloroplast electron transport chain. *Electrons are supplied to photosystem II (PSII) from the splitting of water in the oxygen evolving complex. Upon excitation of P680, en electron is transferred to the Q_A quinone which then reduces the plastoquinone in the Q_B site. The cycling of the plastoquinone (PQ) pool via the cytochrome b_6f protein complex ($cytb_6f$) moves the electrons from the PQ pool to plastocyanin (PC) and pumps more protons across the thylakoid membrane. PC moves by diffusion to dock with photosystem I (PSI). When P700 is energyized, the electron from PC to the iron-sulfer clusters (F_X, F_A, and F_B) and then to ferredoxin (Fd). The ferredoxin-NADPH oxidoreductase (FNR) protein uses Fd to reduce $NADP^+$ to NADPH. NADPH may also come from the mitochondria (mit) or glycolysis and the electrons of the NADPH pool may be fed back into the PQ pool by proteins such as Ndh. This figure is a reproduction of Figure 1 from Rochaix, J.-D. (2011). Biochimica et Biophysica Acta (BBA) - Bioenergetics, 1807(3), 375–383. Permission to use this figure in this work was kindly granted by the present copyright holder (RightsLink license #3979521430165)*

electron from the oxygen evolving complex to drive the oxidation of water and return to the P680 neutral ground state. If the Q_A site is still holding an electron from a previous charge separation event, it suppresses the occurance of a second charge separation, leaving only fluorescence or heat as the remaining routes for energy dissipation (Kitajima & Butler 1975).

From the Q_A site, the electron is then donated to Q_B, which takes two consecutive electrons (two different charge separation events) to be converted from a plastoquinone molecule to a plastoquinol, picking up two protons from the stroma side of the thylakoid membrane in the process. The Q_B plastoquinone/plastoquinol molecule is exchangeable with the pool of plastoquinones and plastoquinols embedded in the thylakoid membrane (aka the "PQ pool") (Crane 1959; Velthuys & Amesz 1974). In the optimal case, the reduced plastoquinol in the Q_B site detaches and enters the membrane pool and then an oxidized plastoquinone from the PQ pool binds to the recently vacated Q_B site, but it is important to remember that diffusion is a stochastic process and the ratio of plastoquinones and plastoquinols dictates the probability of whether the Q_B site will be re-filled by a plastoquinone ready for electrons or another plastoquinol. Because of this dependence on the overall oxidation level of the PQ pool, the fraction of PSII complexes with an electron sitting on their Q_A sites during photosynthesis reflects the ratio of reduced and oxidized plastoquinones in the PQ pool (Amesz *et al.* 1986).

On the other end of the PQ pool in the Z-Scheme model is the cytochrome b_6f complex. This protein complex transfers electrons from plastoquinols in the PQ pool to the electron carrier protein plastocyanin in a process known as the Q-cycle. When plastoquinol binds to the Q_O site of the b_6f complex, one electron transfers to plastocyanin while the other transfers to the b_L and then to the b_H hemes, depositing H^+ from plastoquinol on the lumen side of the thylakoid membrane. On the next turn-over of the b_6f complex, the previous b_H electron and the new electron both reduce the plastoquinone in the Q_i site, picking up H^+ from the stroma side of the membrane. In this way, the b_6f complex adds $2H^+$ into the lumen per electron transferred to plastocyanin. (see Cramer et al. 1996 for a detailed review of the cytochrome b_6f complex). What makes the cytochrome b_6f complex important to fluorescence measurements of photosynthesis is the fact that the transfer of electrons through the cytochrome b_6f complex is relatively slow, causing the PQ pool to become fully reduced (or nearly so) if a sufficiently bright light illuminates the chloroplast (reviewed in Baker 2008).

The plastocyanin proteins in the lumen form a pool of electron carriers whose function is to shuttle electrons from the cytochrome b_6f complex to photosystem I (PSI). Like PSII, the reaction center of PSI also

converts its absorbed photon energy to heat, fluorescence, or charge separation. Upon charge separation, the donated electron traverses over a couple of chlorophylls (commonly referred to as A_0 and A_1) to a series of iron-sulfur clusters before finally being transferred to the electron carrier protein ferredoxin (Takahashi & Katoh 1982; Moenne-Loccoz *et al.* 1994) (reviewed in Blankenship 2002). While we portray PSI as coming "after" PSII in the Z-Scheme model, it is important to keep in mind that PSI and PSII are simultaneously and independently activated by light and are transferring electrons at the same time, which means that the redox poise of electron carriers between PSII and PSI can be manipulated by preferentially exciting one photosystem more than the other.

The Kautsky Curve

Chlorophyll fluorescence offers the most direct non-destructive method to measure the light reaction of photosynthesis. For a given plant leaf or algae sample, the fluorescence yield (relative to illumination intensity) changes over time as the physiological state of the organism varies, changing the probability that an absorbed

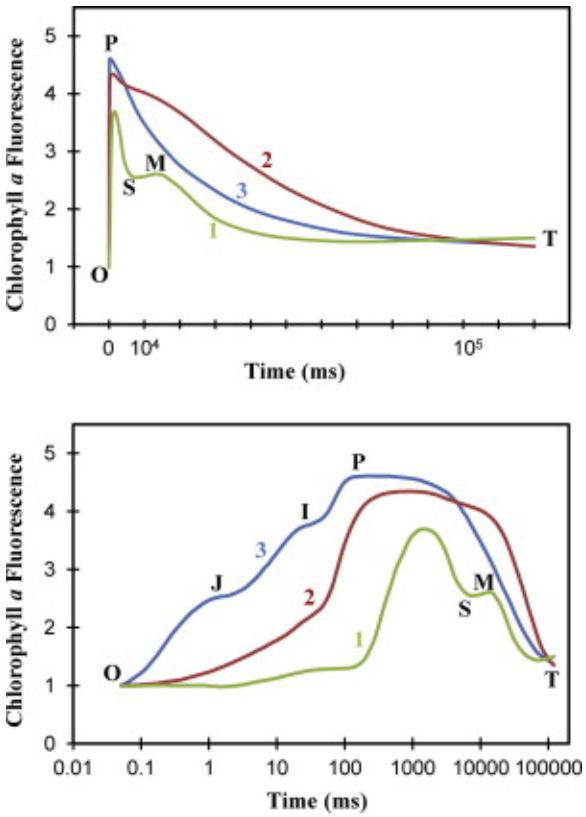

Figure 3: Depiction of the OJIPSMT Kautsky curve. *Representative fluorescence data is plotted on on linear (top) and logarithmic (bottom) time scales. The three lines show expected fluorescence intensity overtime for plant leaves exposed to low (1), moderate (2), and very high (3) light intensities (32, 320, and 3200 micromole photons per square meter per second, respectively). This figure is a reproduction of Figure 1 from Stirbet, A., & Govindjee. (2011), Journal of Photochemistry and Photobiology. B, Biology, 104(1–2), 236–57. Permission to use this figure in this work was kindly granted by the present copyright holder (RightsLink license #3963200417012).*

photon of light will contribute its energy to heat, fluorescence, or photochemistry. In the simple case of a dark-acclimated plant leaf (from a C3 plant) that is then suddenly illuminated with continuous light, the fluorescence of the leaf will quickly rise and then slowly decrease with several distinct phases. The trace of this fluorescence signal is known as a "Kautsky curve" and the 7 phases in the fluorescence signal are designated O, J, I, P, S, M, and T (Figure 3). For a detailed description of the Kautsky curve, see Stirbet & Govindjee (2011).

To summarize the Kautsky curve, it is divided into the fast OJIP portion which occurs on the timescale of milliseconds and the slow PSMT portion that occurs over the course of minutes. In the fast portion, the fluorescence yield rises from the origin (O) to the peak fluorescence yield (P) with two intermediate phases in-between (J and I). The O fluorescence yield is the yield when the maximum amount of photon energy is being used for photochemistry and therefore the smallest amount of energy is dissipated as fluorescence (Stirbet & Govindjee 2011). From this initial fluorescence value of O, the fluorescence yield quickly rises as the capacity for photochemistry in PSII decreases due to the backlog in the electron transport chain as a result of slower downstream processes (most notably the turn-over of the cytochrome b_6f complex). If the illumination intensity is sufficiently bright to saturate the transport of electrons in the thylakoid membrane, then the fluorescence peak yield P is reached. This is the fluorescence yield when photochemistry is completely backed-up and practically all photon energy is dissipated as either fluorescence or heat (as reviewed in Stirbet & Govindjee 2011 and Baker 2008).

After the fluorescence peak P, the fluorescence yield in the Kautsky curve eventually decreases to the terminal fluorescence yield T, often with intermediate steady states (S and M). There are many mechanisms contributing to this decline in yield, but the essence of what is happening during this portion of the Kautsky curve is the acclimation of the plant to the illumination light intensity. This acclimation process can include the induction of protective mechanisms that quench the photon energy or even a loss of functional photosystems due to photodamage (Schreiber *et al.* 1986).

Pump-Probe Fluorescence

While the Kautsky curve is still used as a technique for studying photosynthesis (for example, in Marečková et al. 2016, Pandey & Gopal 2012, and Vredenberg & Pavlovič 2013), it is very difficult to compare experiments performed at different light intensities, and low light intensities will never saturate the plastoquinone pool, thus preventing the measurement of the peak fluorescence yield. Furthermore, if one wants to examine how photosynthesis recovers in the dark (for example, to monitor repair after photodamage has occurred), then

continuous illumination fluorescence is simply not an option.

The solution is to decouple the light that drives photosynthesis (the actinic light) from the light used to measure fluorescence (the measuring light) using the pulse-probe technique. The pulse-probe technique uses a series of very short measuring light pulses (typically between 1 and 100 microseconds long) to measure fluorescence while filtering out the fluorescence caused by the actinic light, either by briefly shuttering the actinic light for the duration of the measuring light pulse or by electronically filtering the signal from the photodetector. Since the measuring pulses are short and dim enough as to not cause any significant amount of photosynthesis on their own, one can measure the fluorescence yield in the dark and therefore obtain information about the recovery of photosynthesis in the dark (as deomonstrated in Joliot & Joliot 1984 and Kramer & Crofts 1990).

Measuring the Light Reactions of Photosynthesis via Fluorescence

The relationship between chlorophyll fluorescence and the processes of the light reactions of photosynthesis are derived from the Stern-Volmer model of fluorescence quenching (as described in Kitajima & Butler 1975 and Lavergne & Trissl 1995), where the fluorescence quenchers consist of heat dissipation (d), electron transfer to the plastoquinone pool (p), and non-photoreductive quenching (NPQ, also known as “non-photochemical quenching”). The rate constants for these processes are denoted with the *k* prefix (e.g. k_d for the heat dissipation rate constant). Figure 5 presents a diagram of the Stern-Volmer model and how it relates to the parameters shown in Figure 4.

Aside from the biological processes of interest, the fluorescence intensity is also dependent on the intensity of the probing light, the optical efficiency of the measurement instrument, the geometry of the sample, and the ratio of light harvesting proteins per photosystem reaction center (discussed in Lavergne & Trissl 1995 and Kramer & Sacksteder 1998). Assuming that none of these parameters change significantly over the timescale of the measurement, they can be lumped together into a generic constant (G). Thus the yield of fluorescence (Y_F) and the observed fluorescence intensity (F) are related by the following formulas:

Eq. 1: $$Y_F = \frac{k_F}{k_F + k_d + q_L \times k_p + k_{NPQ}}$$

Eq. 2: $$F = G \times Y_F$$

Where the parameter q_L represents the fraction of PSII centers able to perform charge separation (in other words, q_L represents the concentration of undamaged PSII reactions centers whose Q_A site is unoccupied), as

described in the “lake model” of photosystem inter-connectivity presented in Kramer et al. (2004).

A single fluorescence measurement does not provide enough information to resolve all of the values, but we can manipulate the experimental conditions to resolve the parameters from only a few different fluorescence measurements (see Figure 4). For example, the k_{NPQ} component can be eliminated from the equation by keeping the leaf/alga sample in the dark for sufficient time for the organism to undo any regulatory quenching and repair any damage to the photosystems (F_O in Figure 4 and Figure 5). The k_p term can be eliminated with a sufficiently bright light such that the turnover of PSII overtakes the activity of the b_6f complexes and saturates the plastoquinone pool such that no more electrons can enter into the plastoquinone pool (F_M and F_M' in Figure 4 and Figure 5) (as reviewed in Baker 2008). In mathematical terms, this is described by the following equations:

Eq. 3: $$F_M = G \times \frac{k_F}{k_F + k_d}$$

Eq. 4: $$F_O = G \times \frac{k_F}{k_F + k_d + k_p}$$

Eq. 5: $$F_M' = G \times \frac{k_F}{k_F + k_d + k_{NPQ}}$$

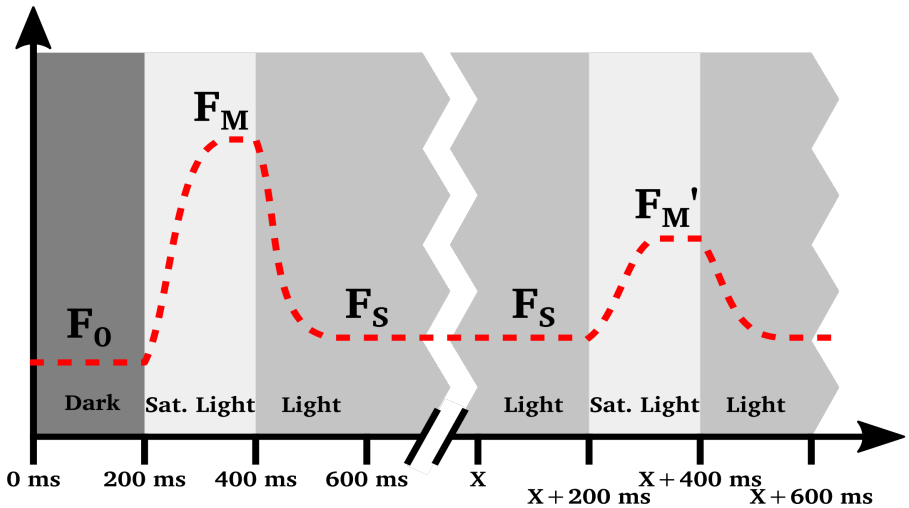

Figure 4: Example pulse-probe fluorescence experiment. *The fluorescence states F_O, F_M, F_S, and F_M' are useful for calculating various parameters with the Stern-Volmer model of fluorescence quenching in photosynthesis. Prior to the start of this experiment, the plant/algae sample is typically kept in complete darkness for minutes to hours to achieve complete relaxation of regulatory non-photoreductive quenching. The background illumination begins with darkness and then switches to a super-saturating illumination, which is then followed by some period of time at growth-light (or experimentally varied) illumination. During the growth illumination, periodic super-saturating pulses are delivered to measure the F_M' parameter. In most cases, the decrease in fluorescence signal from F_M to F_M' is caused primarily by the induction of non-photoreductive quenching.*

Eq. 6: $$F_S = G \times \frac{k_F}{k_F + k_d + q_L \times k_p + k_{NPQ}}$$

The k_d term from the Stern-Volmer model cannot be easily eliminated, but it is theorized to simply be the inherent inefficiency of the photosystem and therefore assumed to be a constant value.

Noticeably absent from the Stern-Volmer model of chlorophyll fluorescence is the consideration of PSI fluorescence. This is because charge separation in PSI is not generally inhibited by an electron sitting in the downstream electron pathway (unlike in PSII) and therefore the yield of fluorescence from PSI does not change significantly under most conditions (Trissl 1997), though it does contribute about 30-40% of the steady-state fluorescence signal (Pfündel 1998; Franck *et al.* 2002).

Yield of PSII (Φ_{II})

The quantum yield of PSII, or Φ_{II}, is a measure of the fraction of PSII complexes that are ready to use the energy of a photon to send an electron into the electron transport chain. It is typically measured with a series of measuring pulses over the course of two light treatments, each light intensity lasting about 200 ms: growth light intensity for the F_S measurement followed by a saturating light intensity for the F_M', as shown in Figure 4. Φ_{II} is

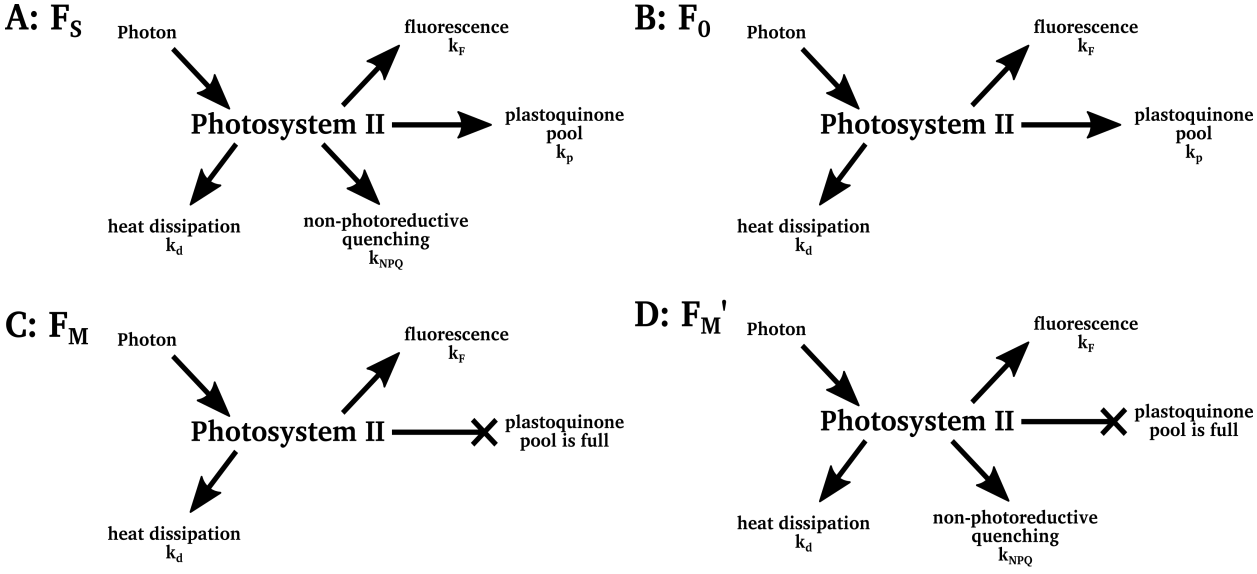

Figure 5: Diagram of the Stern-Volmer model of chlorophyll fluorescence. *In the steady-state (panel A), the energy from an absorbed photon has four fates: unregulated dissipation as heat (k_d), regulated non-photoreductive quenching (k_{NPQ}), transfer of an electron to the plastoquinone pool (k_p), or fluorescence re-emission as a photon (k_F). Given a sufficiently long period of dark acclimation (panel B), all regulatory quenching is relaxed, removing non-photoreductive quenching as a possible fate for an exciton of energy. Super-saturating illumination of such as dark acclimated chloroplast (panel C) will soon saturate the plastoquinone pool and leave only fluorescence and unregulated heat dissipation as the means for dissipating absorbed light energy. Given the same super-saturating illumination to a chloroplast that is not dark acclimated (panel D) is like the previously mentioned situation, except that some of the energy will be dissipated by any regulatory non-photoreductive quenching. The fluorescence signal associated with these four states are referred to as F_S, F_O, F_M, and F_M', respectively (see Figure 4).*

calculated as shown in Eq. 7 and ranges from about 0.83 down to zero, depending on the light intensity and the induction of fluorescence quenchers (such as NPQ). If the sample has been dark-acclimated immediately prior to this measurement (steady-state "illumination" is darkness), then the F_s value is recorded as F_O and the F_M' is the F_M for the experiment. This maximal Φ_{II} value is known as F_V/F_M (short for variable fluorescence over maximum fluorescence, Eq. 8) and it is important when calculating the induction of NPQ (Kitajima & Butler 1975; Joliot & Joliot 1984) (reviewed in Genty et al. 1989 and Baker 2008).

Eq. 7: $$\Phi_{II} = \frac{(F_M' - F_S)}{F_M'}$$

Eq. 8: $$F_V / F_M = \frac{(F_M - F_0)}{F_M} \approx 0.83$$

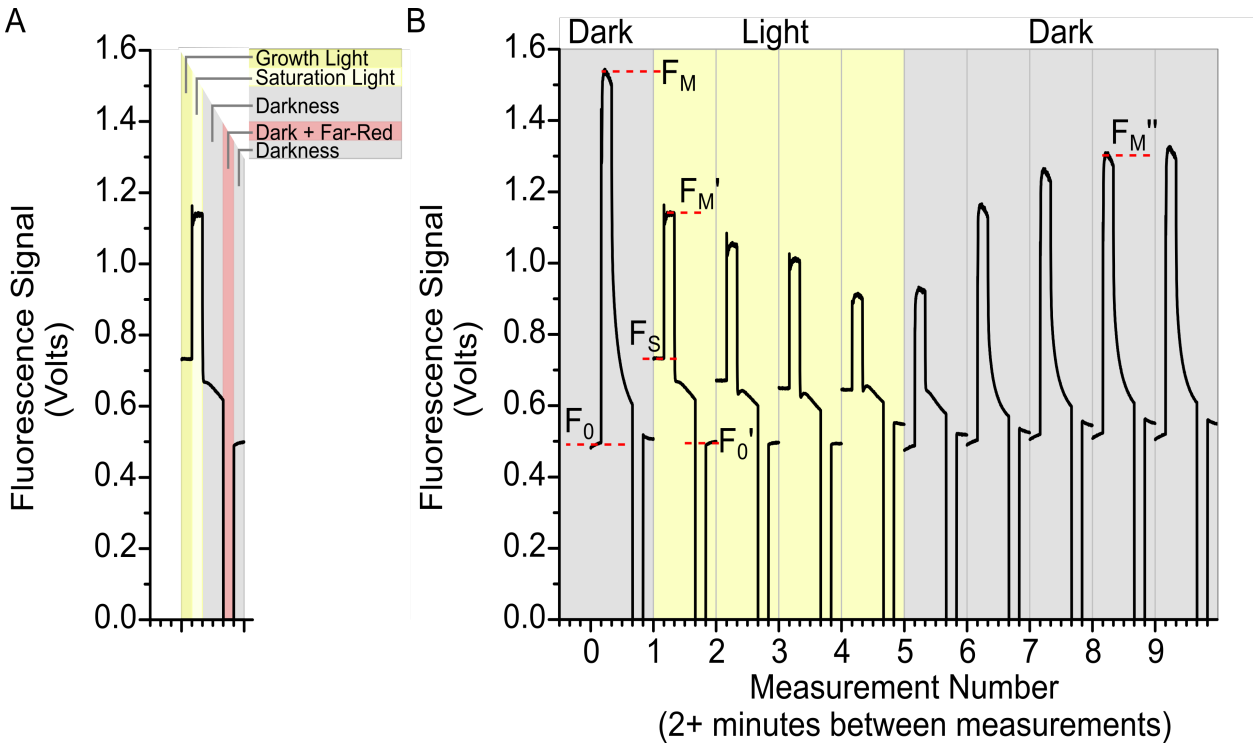

Figure 6: Example fluorescence data trace. *For each measurement (panel A), the background illumination is cycled through growth illumination (or darkness), saturating light intensity, darkness, darkness with far-red illumination, and darkness again. Background growth illumination is immediately restored after the measurement. Note that the fluorescence detector is blinded by the far-red illumination and therefore the fluorescence signal during this pulse cannot be resolved. In an example experiment (panel B), a cuvette of C. reinhardtii culture is dark acclimated for 30 minutes followed by the F_M measurement. Then the growth light is set to an intensity of 490 µmol photons/m^2/s periodic measurements, and then the growth light is set to darkness for another time period with periodic measurements. The partial recovery of the maximal fluorescence (F_M'') suggests that a portion of the induced non-photoreductive quenching is the result of irreversible changes to photosystem II (e.g. photodamage).*

By itself, Φ_{II} only measures the state of PSII, but if the light intensity is also known, then one can estimate the total linear electron flux (LEF) with the following formulation:

$$\text{Eq. 9:} \quad LEF = i \times A \times fraction_{PS2} \times \Phi_{II}$$

Where i is the light intensity, A is the absorptivity of the sample, and $fraction_{PS2}$ is the fraction of absorbed light which stimulated PSII, generally assumed to be 0.4 (Melis & Thielen 1980).

This estimate also does not account for the effective size of the light harvesting antenna per photosystem (which may vary between two different samples), but nevertheless proves useful when examining the responses of a sample over time or through a sequence of light intensities (Genty *et al.* 1989).

Non-Photoreductive Quenching

When plants and algae experience stress, especially high-light stress, Φ_{II} decreases both because of the accumulation of oxidative damage to the photosystems and because of the induction of quenching mechanisms to protect the photosystems from further damage. The combined quenching from these processes is referred to as non-photoreductive quenching (NPQ, aka non-photochemical quenching). The total amount of NPQ can be determined by the decrease in Φ_{II}, calculated as follows:

$$\text{Eq. 10:} \quad \Phi_{NPQ} = \frac{(F_M - F_M')}{F_M}$$

If the sample is given a dark recovery period of about 10 minutes, then the recovery of Φ_{II} in the dark indicates how much of the NPQ was regulatory (i.e. reversible quenching) and how much was "damage" (i.e. irreversible quenching)[1]. These components of NPQ are known as q_E and q_I respectively (reviewed in Müller et al. 2001). The q_E component is mediated by the xanthophyll cycle, wherein the enzyme violaxanthin de-epoxidase conerts the carotenoid pigment violaxanthin into zeaxanthin. Once formed, the zeaxanthin efficiently dissipates the energy of excited chlorophylls in the PSII complex (reviewed in Demmig-Adams & Adams 1996 and Cruz et al. 2005). The q_I component of NPQ arises from the inactivation of PSII reaction centers by reactive oxygen. This occurs when the Q_A site is reduced for an extended amount of time (usually because the PQ pools is unusually reduced), presenting an opportunity for charge recombination in PSII, which in turn can lead to the formation of the triplet chlorophyll. Triplet chlorophyll can then transfer its excitation energy to molecular oxygen, forming singlet oxygen, which then

1 The term "damage" is used in quotes reflecting ambiguity over whether the process of q_I should be categorized as damaging or protective. These disabled PSII complexes are efficient quenchers and may have evolved to fail in a particular manner as to protect the other photosystems from further damage, as Aro et al. (1993) discusses in their review of photosystem repair.

oxidizes the PSII protein (Hideg *et al.* 1994; Triantaphylidès *et al.* 2008) (reviewed in Krieger-Liszkay 2005).

The equations for partitioning NPQ into q_E and q_I using fluorescence measurements (see Figure 6) are as follows:

Eq. 11: $$q_E = \frac{\left(F_M'' - F_M'\right)}{F_M'}$$

Eq. 12: $$q_I = \frac{\left(F_M - F_M''\right)}{F_M'}$$

There are a few caveats to the measurement of NPQ, however, as this technique for measuring NPQ can be thrown-off by the dissociation of the light-harvesting proteins from the PSII complex, a process called state transitions (Bonaventura & Myers 1969). The effect on the fluorescence signal is similar to quenching, but the mechanism is a decrease in the effective light harvesting area per photosystem rather than a quenching of the photosystems. Microalgae such as *Chlamydomonas reinhardtii* are particularly prone to state transitions if cultured with organic carbon or if the culture media is depleted of oxygen (e.g. by respiration in the dark) (Finazzi *et al.* 1999; Subramanyam *et al.* 2006; Lucker & Kramer 2013). In this case, the alga can be encouraged to re-associate their light harvesting proteins to the PSII complexes by illumination with far-red illumination for a few minutes. This preferentially stimulates PSI over PSII, oxidizing the electron transport chain. An unidentified phosphatase is believed to sense the oxidation of the PQ pool and then promote the re-association of the LCHII antenna proteins with PSII (see Bonaventura & Myers 1969 and Goldschmidt-Clermont & Bassi 2015).

$NPQ_{(T)}$

Since NPQ is associated with stress responses in plants and algae, it would seem like a practical measurement for a field researcher to use when assessing plants in their outdoor environment. Yet this is simply not practical (and often impossible). The reason is that the F_M parameter necessary for the calculation of NPQ requires a very long (usually overnight) dark acclimation period to satisfy the “no NPQ” assumption of the Stern-Volmer model of F_M. We cannot shutter the sun for 8 hours prior to each measurement and setting up a fluorometer for each leaf before dawn would be both prohibitively expensive and extremely impractical.

If we had an alternative method to measure F_M without an extended dark interval, then one could measure NPQ anywhere and anytime. As demonstrated in (Tietz *et al.* 2017), one can use the knowledge that the maximal Φ_{II} should be 0.83 to calculate the “theoretical” non-photoreductive quenching ($NPQ_{(T)}$), essentially deriving the F_M

value rather than measuring it directly.

Eq. 13: $$NPQ_{(T)} = \frac{4.88}{\left(\frac{F_M'}{F_0'}\right) - 1} - 1$$ (Tietz *et al.* 2017)

The challenge with $NPQ_{(T)}$, however, is the introduction of a new fluorescence signal that needs to be measured: F_O'. The Stern-Vomer model of F_O' is the same as for F_O except that some of the energy may be diverted into NPQ:

Eq. 14: $$F_O' = G \times \frac{k_F}{k_F + k_d + k_p + k_{NPQ}}$$

F_O' can be obtained by briefly exposing the sample to far-red illumination (absent any other source of background light), which will cause disproportionately more photosystem I turnover relative to PSII turnover, thereby oxidizing the plastoquinone pool and thus freeing the Q_A sites on practically all of the PSII complexes (q_L = 1) (Kramer *et al.* 2004). It usually takes only a few hundred milliseconds for the far-red illumination to sufficiently oxidize the plastoquinone pool.

With $NPQ_{(T)}$, it is now possible to estimate non-photoreductive quenching on-demand and in natural environments. It will be interesting to see whether this phenomenon turns out to be as important in nature as it appears to be in a laboratory setting.

The Electrochromic Shift

Several steps in the Z-Scheme model of the photosynthetic electron transport chain transfer protons across the thylakoid membrane, generating an electrochemical potential. This potential is known as the proton motive force[2] (*pmf*) because it drives protons through ATP-synthase enzymes embedded in the thylakoid membrane, synthesizing ATP. There are two components that make up the *pmf*: a differential pH across the membrane (ΔpH) and an electric field across the membrane (Δψ). The pH component is formed by the relative concentrations of protons on either side of the membrane, as per the definition of pH ($pH = -\log_{10}[H^+]$). Since the protons carry an electric charge, the accumulation of positive proton charges inside the lumen also generates an electric field (see Figure 7). The total *pmf* potential is described by the Nerst equation:

2 Both chloroplasts and mitochondria have a *pmf* to drive ATP synthesis. This work will only discuss the *pmf* in the context of the chloroplast.

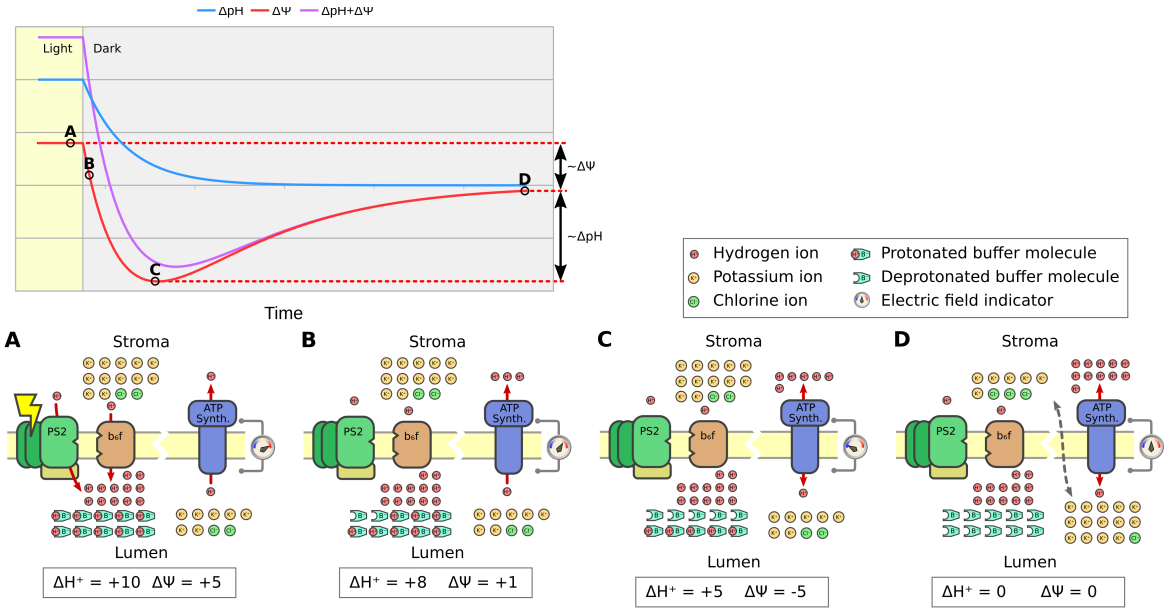

Figure 7: Diagram depicting the use of the electrochromic shift (ECS) to parse the pH and electric field components of the chloroplast proton motive force (pmf).

Top: pH (ΔpH) and electric field (ΔΨ) components of the pmf at the transition from growth illumination to darkness. Note that the A520 absorption changes are proportional only to the ΔΨ, yet the dark recovery of the ΔΨ relates to the partitioning of the two components (dotted lines). The ion movement at specific time points (labels A-D) are depicted below.

Bottom: In the illuminated steady-state (A), the light reactions pump protons into the lumen, establishing both a pmf consisting of an electrical potential (ΔΨ) and a proton chemical potential (ΔH^+, used in place of ΔpH for the sake of simplicity). Immediately after the light shuts off, the rate of H^+ into the lumen is zero, but the rate of H^+ continues unabated, such that the rate at a time shortly after the light shange (B) can be taken as the steady-state H^+ flux. As protons rapidly exit the lumen through the ATP-synthase, both the ΔH^+ and the ΔΨ collapse, but due to the buffer capacity of the lumen, each proton has a much greater effect on ΔΨ than ΔH^+. Thus the ΔH^+ quickly drives the protons out until the ΔΨ is reversed and equal to the remaining ΔH^+ (C). The magnitude of the change in the field from the steady-state to this point is approximately proportional to the total pmf. After this point, the ΔH^+ and ΔΨ remain equally opposed as other ions (potassium and chlorine shown here) slowly cross the membrane until equilibrium is finally reached (D). The more of the steady-state pmf that is stored as ΔH^+, the more counter-ion movement it takes to drain the pool of buffered H^+

Eq. 15: $$pmf = \Delta\Psi + 2.3\frac{RT}{F} \times \Delta pH$$

The strength of the lumen *pmf* and its partitioning into pH vs electric field components plays an important role in protecting plants and algae from accumulating damage during photosynthesis (as discussed in Kramer et al. 1999, Cruz et al. 2005, and Davis et al. 2016). A sufficiently strong Δψ could electroporate the membrane (Weaver 1995) and even a physiological relevant Δψ can be strong enough to make PSII more prone to producing toxic reactive oxygen species (Davis *et al.* 2016). As for the pH, should the lumen acidify to pH 5 or lower, then catastrophic damage will occur to proteins inside the lumen and as well as the thylakoid membrane (Katoh &

Takamiya 1964; Krieger *et al.* 1993). In addition, the pH inside the lumen signals the photoprotective mechanism known as q_E and affects the turnover rate of the cytochrome b_6f complex (reviewed in Witt 1979, Kramer et al. 1999, and Cruz et al. 2005).

One notable and important difference between chloroplasts and mitochondria, both of which make ATP using a *pmf* to drive H^+ though ATP-synthase, is that while the mitochondria store their *pmf* as mostly $\Delta\psi$ (Nicholls 1974), chloroplasts keep their *pmf* as mostly ΔpH (Kramer *et al.* 1999). This means that the thylakoid membrane is permeable to other ions, allowing the flow of counter-ions to dissipate the electric field generated by the flux of H^+ ions into the lumen. Exactly which ions are allowed through the thylakoid membrane and by what mechanisms is still the subject of active research and debate (see Spetea & Schoefs 2010 and Checchetto et al. 2016).

With the *pmf* and its components playing such a vital role in the chloroplast, it is not surprising that plants and other photoautotrophs have several mechanisms to control and regulate the *pmf*. They can regulate the flow of H^+ into the lumen by quenching the capture of light energy, thereby reducing the turnover of the electron transport chain, and they can regulate the flow of H^+ out of the lumen by adjusting the activity of the ATP-synthase enzymes. On the input side, the NPQ mechanism q_E is activated by a drop in the lumen pH, providing a negative feedback loop to protect against over-acidification of the lumen. Since the *pmf* in the steady-state is mostly ΔpH, this is also a negative feedback regulator of the overall *pmf* (Briantais *et al.* 1979). On the other side of the equation, regulation of the ATP-synthase controls flux of H^+ out of the lumen. Under some conditions, such as low CO_2 stress, plants will reduce a regulatory disulfide bridge on the gamma subunit of the chloroplast ATP-synthase to slow down its activity, raising the *pmf* (Kanazawa & Kramer 2002; Cruz *et al.* 2005; Kohzuma *et al.* 2012). It might seem counter-intuitive to suppress ATP production in this way, but it is necessary to acidify the lumen enough to induce the protective q_E NPQ mechanism to prevent further harm that would result from an over-reduction of the electron transport chain (Kanazawa & Kramer 2002).

One can measure the *pmf* and the activity of the ATP synthases in the chloroplast by kinetic absorption spectroscopy. As per the theory of electrochromism (Liptay 1969), the presence of an electric field across the thylakoid membrane shifts the absorption spectrum of the carotenoid pigments embedded within the thylakoid membrane. This electrochromic shift (ECS) manifests as a change in the absorbance of the sample when measured with green light of 520 nm in wavelength (Gorkom *et al.* 1974; Chylla *et al.* 1987). However, the *pmf* in the chloroplast is partitioned mostly as a pH gradient rather than an electric field, so instead of analyzing the steady-

state ECS signal, we employ the dark interval relaxation kinetic (DIRK) technique (Witt 1979). Described in detail in Kramer & Sacksteder (1998), this techniques involves measuring the changes in ECS absorption when the growth light is briefly shuttered. With the flux of H^+ into the lumen suddenly halted, the initial rate of H^+ efflux continues as it was during the previous steady-state, and as the H^+ ions flow out of the lumen, the corresponding change in the electric field is reflected in the decay of the ECS (as shown in Figure 8). This initial decay can be approximated as a first-order exponential decay:

Eq. 16: $$Y(x) = Y_0 + A \times e^{-(x-x_0)/\tau}$$

After fitting the above first-order exponential decay curve (where Y is the A_{520} absorption change and x is time), one can estimate steady-state proton flux (vH^+), ATP-synthase proton conductivity (gH^+), and the overall *pmf* with the following formulas:

Eq. 17: $$vH^+ = \frac{A}{\tau}$$

Eq. 18: $$gH^+ = {}^{1}\!/_{\tau}$$

Eq. 19: $$pmf = A$$

Note that the vH^+ and *pmf* equations are estimates that depend on the absolute absorption (A) of the sample. Since the absolute absorption is also going to be influenced by light scattering and other optical properties of the sample, it is usually not possible to compare two different samples (no two leaves have identical light scattering, for

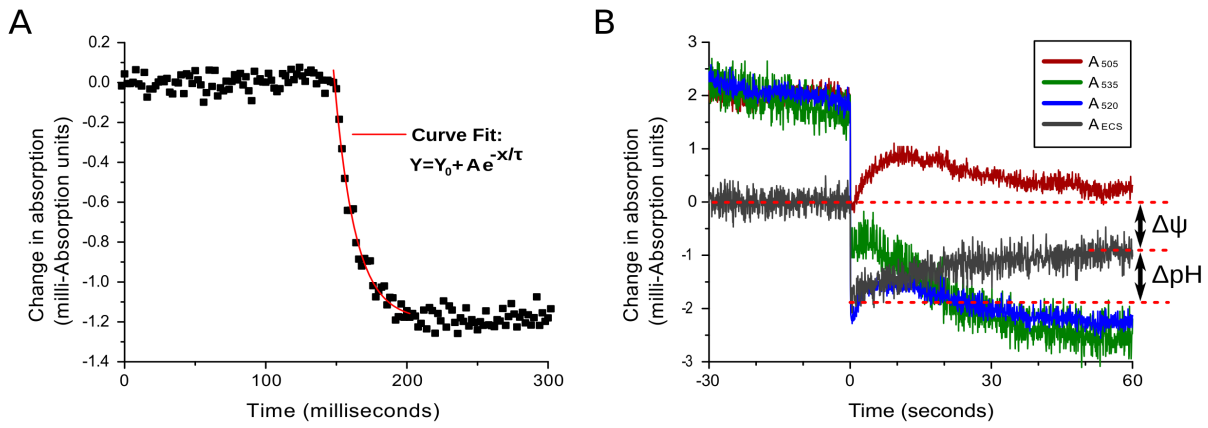

Figure 8: Analysis of electrochromic shift data. *The initial decay in the A_{520} absorption signal (panel A) fit with a first-order exponential decay. The parameters τ and A from this fit are used to calculate proton flux, proton conductivity, and pmf magnitude. An extended dark interval absorption signal is deconvoluted using the formula $A_{ECS} = A_{520} - 0.5 \times A_{505} - 0.5 \times A_{535}$ (Cruz et al. 2001) (panel B). The partial recovery back towards the illuminated steady state indicates the partitioning between the ΔpH and the ΔΨ components of the pmf at the time of the light to dark transition.*

example). This makes gH^+ the most useful of these calculations and its value reflects the regulation of the chloroplast ATP-synthases. When the ATP-synthase activity is down-regulated to build up a higher *pmf*, for example, the conductivity value gH^+ will decrease.

A variant of the DIRK technique is the parsing trace, which works by extending the dark interval out for a minute or longer. In the parsing trace, the ECS absorption will partially recover to a new dark steady-state (discussed in Kramer et al. 1999 and Kramer et al. 2003). While this may look like a paradoxical regeneration of the *pmf* in the dark, it actually reflects the diffusion of counter-ions into the lumen after the ΔpH and Δψ across the membrane became equally opposed to each other (the local minimum of the ECS signal marks the start of this equal opposition point). If all of the *pmf* potential were stored as a ΔpH during the illuminated steady-state (as might be the case if counter-ions were completely free to permeate through the membrane in the light), then the dissipation of the ΔpH would require an equal magnitude of counter-ions crossing the thylakoid membrane, thus bringing the ECS

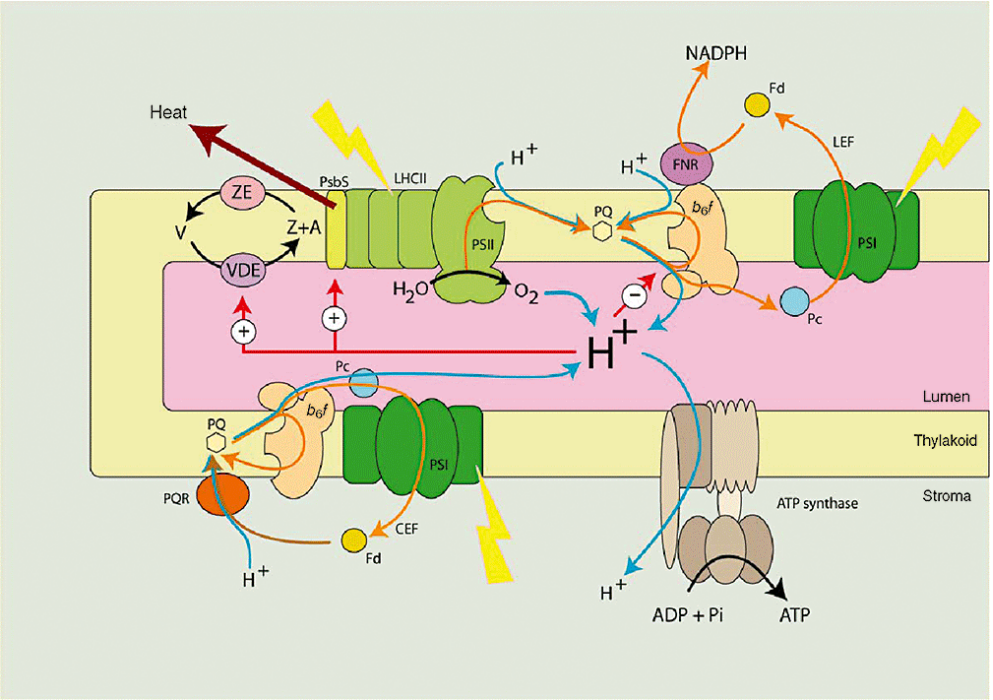

Figure 9: Diagram of electron flux (orange arrows) and proton flux (blue arrows) through the thylakoid membrane. *over the course of linear electron flux (upper membrane) and generic cyclic electron flux (lower membrane). As electrons are shuttled from photosystem II (PSII) through the cytochrome b_6f protein complex (b_6f), there is a net translocation of protons (H^+) from the stroma to lumen. Some of the regulatory effects controlled by the accumulation of H^+ in the lumen are indicated with red arrows. In particular, the reduced pH inhibits the turnover of b_6f and activates non-photoreductive quenching in the PSII antenna proteins and stimulates the conversion of violaxanthin (V) into antheraxanthin (A) and zeaxanthin (Z). In cyclic electron flux, electrons from ferredoxin (Fd) are used to reduce the plastoquinone (PQ) pool via PQ-reducing enzyme (PQR). This is a reproduction of Figure 1 from Baker, N. R., Harbinson, J., & Kramer, D. M. (2007). Plant, Cell & Environment, 30(9), 1107–1125. Permission to use this figure in this work was kindly granted by the present copyright holder (RightsLink license #3977661036402).*

absorption back to the steady-state level. However, some of the *pmf* may be partitioned as Δψ, in which case it takes fewer counter-ions to dissipate the ΔpH and the ECS falls short of returning to the steady-state level. In this way, the partitioning of *pmf* into ΔpH and Δψ can be estimated by comparing the dark ECS absorption to the illuminated steady-state absorption level (reviewed in Kramer et al. 1999, Kramer et al. 2003, and Bailleul et al. 2010). Figure 7 provides a simulated demonstration of the parsing trace to show exactly why the ECS signal works this way.

It is important to note that when using DIRK to measure the partitioning of the *pmf*, one needs to measure the ECS signal at multiple measurement wavelengths (such as A_{520} and A_{535}) to account for non-ECS changes in optical properties that can occur on the seconds to minutes time-scale (as shown in Figure 8, panel B) (discussed in Gorkom et al. 1974, Kramer & Sacksteder 1998, and Cruz et al. 2005).

Cyclic Electron Flux

Taken together, the measurements of the fluorescence and electrochromic shift (ECS) of a plant or alga reveals the relative fluxes of electrons and protons through the thylakoid membranes in the chloroplast. If the tranfer

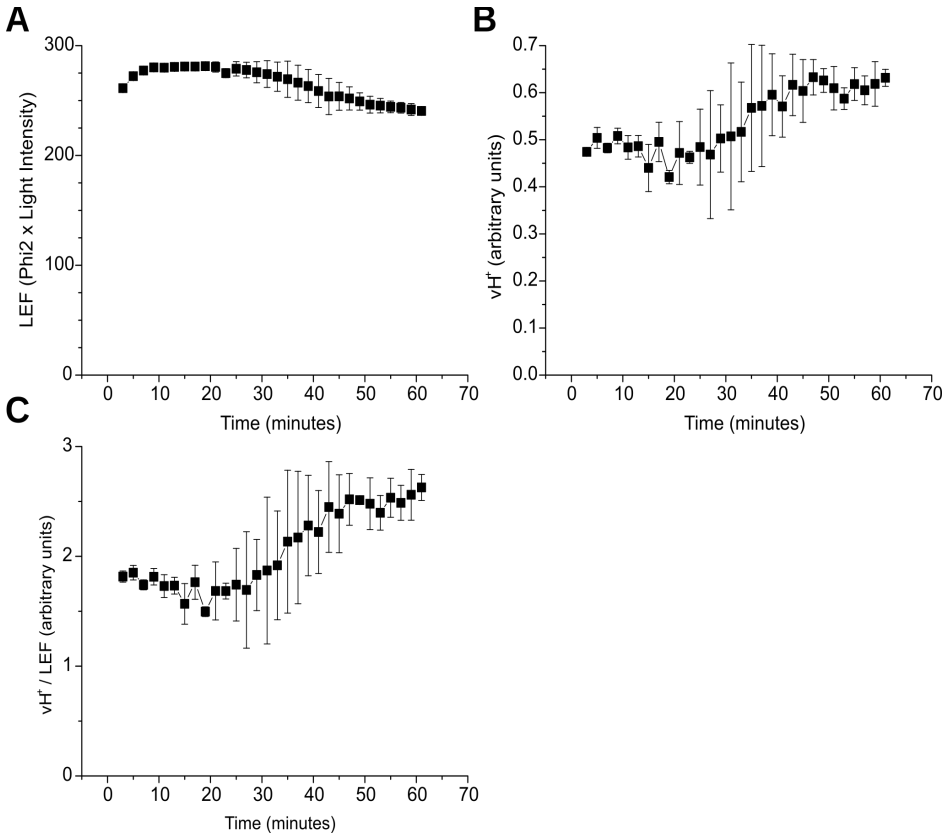

Figure 10: Induction of cyclic electron flux (CEF) in C. reinhardtii in response to depletion of inorganic carbon in the media. *Over the course of an hour in a stirred cuvette at constant light intensity, the yield of photosystem II (Phi2), gradually decreased (panel A) while the proton flux through the thylakoid ATP synthases (vH^+) increased (panel B). Thus the flux of protons relative to the flux of electrons increased (panel C) indicating an increase in CEF. Note that the ratio of CEF to linear electron flux (LEF) at time 0 is unknown as this experiment lacks a zero-CEF (or zero-LEF) control.*

of electrons through the electron transport chain were a strictly linear process, then 4 H^+ are pumped into the lumen for every electron that goes from water to NADPH, resulting in an ATP:NADPH ratio of approximately 1.3. However, the Calvin-Benson cycle consumes ATP and NADPH at a ratio of 1.5, and abiotic stresses may drive the demand for ATP even higher (especially in organisms with a carbon-concentrating mechanism). To generate extra ATP to make-up for this shortfall, plants and algae cycle the electrons from NADPH back into the chloroplast electron transport chain, pumping more H^+ into the lumen as the electron is once-again shuttled through the cytochrome b_6f complex (see Figure 9 for a diagram of CEF pathways) (reviewed in Baker *et al.* 2007 and Kramer & Evans 2011). The occurrence of cyclic electron flux (CEF) can be estimated by combining the chlorophyll fluorescence measurements with the ECS measurements to plot the vH^+ versus the LEF. The hallmark of CEF is an increase in vH^+ relative to LEF, as shown in Figure 10. Like NPQ, cyclic electron flux (CEF) is an important indicator on how the plant is adjusting its photosynthesis to handle a stressful environment.

CHAPTER 1: MEASURING PHOTOSYNTHESIS BY FLUOROMETRY AND SPECTROPHOTOMETRY

In the introduction, I laid out the theoretical basis for the measurement of the light reactions of photosynthesis by a combination of fluorometry and absorption spectrophotometry, but designing a measurement instrument capable of performing these measurements is not a trivial task. The engineering challenge is even greater if one intends to perform these measurements in a fluctuating environment, as this requires that the instrument be flexible enough to manipulate the sample environment and automated enough to do so reproducibly.

Building upon previous instrument designs (see Kramer & Crofts 1990, Kramer & Sacksteder 1998, and Sacksteder et al. 2001), Professor David Kramer, Jeffrey Cruz, Robert Zegarac, and myself set out to build a new combined fluorometer/spectrophotometer instrument. We faced three major design challenges: utilizing a new generation of high-power light emitting diodes (LEDs), safer and cheaper precision electronic timing hardware, and updated software to fully utilize the new hardware. I was responsible for the latter two tasks.

The older instruments used the PulseBlaster from SpinCore Technologies Inc. to deliver high precision electronic timing control, but its price was becoming unsustainable expensive and it lacked a fail-safe mechanism for protecting connected hardware from damage should the host computer unexpectedly reboot. I recognized that the PulseBlaster's high-precision timing function could not be replicated in a standard microprocessor, but such a feature was possible with a less common architecture known as a field-programmable gate array (FPGA). Using a Naxsys 2 FPGA prototyping board from Digilent Inc., I implemented in FPGA logic a digital circuit capable of replicating the functions of the PulseBlaster at one-tenth the cost. My design also incorporated a fail-safe feature that has since saved several instruments from damage.

The software used to run our instruments was originally written my Professor David Kramer and already functional. However, the code suffered from its age and no longer worked reliably on current versions of Microsoft Windows. In order to keep the software usable on both new hardware and newer Windows operating systems, I restructured parts of the software to use a newer programming paradigm known as object oriented programming. The end result was fewer crashes and the ability to run on newer computers.

With new software, FPGA timing hardware, and new electronics with high-power LEDs, our new instrument became the workhorse for most of our photosynthesis measurements. In this chapter I present our new instrument, the IDEA spectrophotometer, as well as a brief discussion of remaining challenges and opportunities for future development.

PREVIOUS TECHNOLOGIES

The development of any technology is an iterative process. The following instrument designs were a major influence on the design process for the IDEA spectrophotometer.

Jolliot's PAM Fluorimeter

The first standardized instrument design for measuring photosynthesis by pulse-probe fluorometry was the pulse amplitude modulation (PAM) fluorometer designed by Pierre Joliot in the early 1980's (Joliot *et al.* 1980; Joliot & Joliot 1984). It featured a sample chamber with ports for aiming light sources and detectors at a leaf or cuvette sample held in the center of a dark chamber. One port would shine the actinic light onto the samples while another port provided a pulsed measuring beam that would be recorded by detectors attached to yet another port. If the port for the measuring beam is directly across from the detector, then the absorption changes can be measured with the appropriate choice of optical filters.

Dr. Kramer's D.O.F.S. and NoFoSpec

One of the problems with measuring plant leaves in a Joliot style instrument is that the leaf scatters most of the light that hits it, so if one is measuring absorption through a leaf in the Joliot style sample sample chamber, most of the light is scattered away from the detector and the signal is therefore very weak. Furthermore, changes in the light scattering properties of the sample during the experiment will create a false signal that appears to be a change in absorption (Kramer & Sacksteder 1998). To solve this problem, Drs. Kramer and Sacksteder developed the diffused optic flash spectrophotometer (DOFS) and its successor, the non-focusing optics spectrophotometer (NoFoSpec). The DOFS and NoFoSpec hold the sample sandwiched between two optical-acrylic light guides. At such close proximity, most of the scattered light enters the light guide and is directed to the photodiode detectors (Sacksteder *et al.* 2001), minimizing signal loss and artifacts caused by changes in the sample’s light scattering properties.

The LI-6400XT

LI-COR Incorporated began selling their LI-6400 instrument in 2001 (LI-COR Inc. 2016). This and later models of their LI-6000 series of portable gas analyzers include a pulse-probe fluorometer in the leaf chamber. Like the DOFS, the LI-6400 minimizes the air-gap between the leaf sample and the optical equipment. However, the LI-6400 does not measure absorption through the leaf and the choice of measuring colors is limited. While these limitations make the LI-6400 a poor choice for developing new techniques for measuring photosynthesis, the quality

of its CO_2 gas analyzer resulted in the LI-6400 becoming the benchmark standard for photosynthesis measurement instrumentation in the United States of America.

THE IDEA SPECTROPHOTOMETER

According to the "time is money" principle (Franklin 1961), home-brew instrumentation is ***not*** cheaper than purchasing expensive equipment such as the LI-6400XT from LI-COR Inc., so the development of a new scientific instrument is not to be considered lightly. In this case, development was driven by the need for a single modular platform that could be used for measuring photosynthesis in very small leaves of mutant *Arabidopsis thaliana* lines as well as normal *A. thaliana* leaves and liquid algae or chloroplast suspensions. We also sought to capitalize on recent advances in high-power LEDs to improve the sensitivity and reproducibility of the previous NoFoSpec design (Hall *et al.* 2013).

Design Goals

Our primary design goal of the integrated diode emitter array spectrophotometer (IDEA spectrophotometer) was to consolidate the physical and electronic hardware design of the NoFoSpec to make the IDEA spectrophotometer both more modular and easier to build. To make it more modular, we standardized the physical parts for mounting everything in a line along a length of T-slotted extruded aluminum rail, thus new modules could be inserted and anchored by simply sliding it into place. We also designed and commissioned mass producible housing cases to house the electronics without the need for drilling holes into generic project boxes. On the

Figure 11: Photo of the optical assembly of an IDEA spectrophotometer. *All optical components are mounted in a line on a rail of T-slotted extruded aluminum, which allows for easy installation and removal of components.*

electronics front, the circuits were all redesigned to use surface-mount electronic components. These components can be assembled by pick-and-place robots and many circuit board manufacturers will (for an additional fee) pre-assemble the circuit boards with expert care. Not only did this save substantial human assembly time, but it also reduced the amount of troubleshooting time after instrument assembly because the circuit board manufacturers generally have high quality assembly robots (and experienced operators).

The second goal in the IDEA spectrophotometer design was to improve the quality and sensitivity of the fluorescence and absorption signals. A major source of noise in the NoFoSpec instruments was due to the warming of the LED emitter over the course of the measurement. Robert Zegarac, our electrical systems developer, was able to solve this particular problem by replacing the heat-sink elements that we had been attaching to the back of our LED emitters with a circuit board made from aluminum instead of plastic. With the circuit board itself acting as a heat-sink and using newer models of high-power LEDs, the warming artifact from the LEDs virtually disappeared.

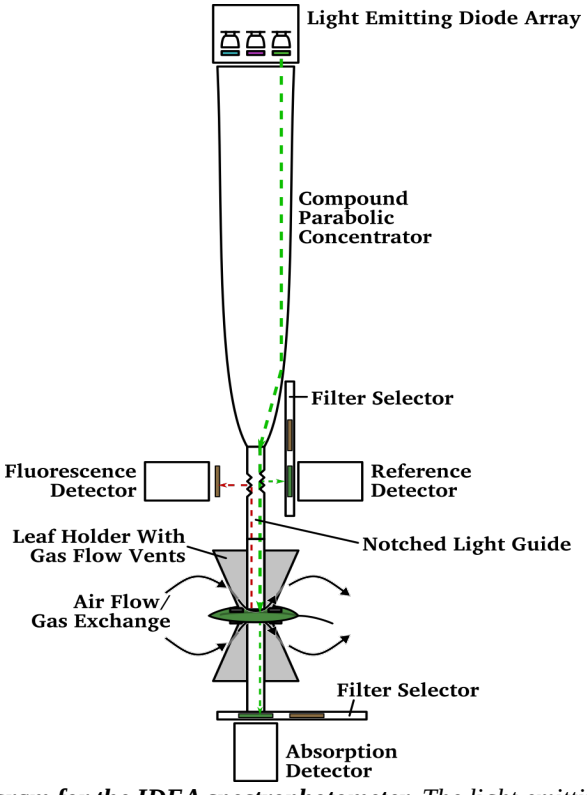

Figure 12: Optical design diagram for the IDEA spectrophotometer. *The light emitting diode array houses seven high-power LEDs with reflecting optics and individual optical filters. The light from these LEDs is collected in the compound parabolic concentrator, which funnels the light to a notched light guide. The notches scatter some of the light to the reference and fluorescence detectors. A collar around the light guides cushions the leaf sample and has vents designed to flow air/gasses across the front and back surfaces of the leaf. An appropriate selection of optical filters in front of the detectors ensures that the fluorescence detectors do not pick-up the measuring pulses and that the absorption and reference detectors do not pick-up fluorescence.*

Modular Physical Structure

The IDEA spectrophotometer is made modular by mounting all modules to a length of T-slotted aluminum rail (pictured in Figure 11). When needed, the modules can slide out of position for repairs, modifications, or the addition of new hardware. We also used a 3D printer to produce adapters to incorporate other scientific instruments and hardware, such as oxygen probes or optical filter changers.

Optical Design

To accommodate multiple light sources, the IDEA spectrophotometer uses a compound parabolic concentrator (CPC) to collect the light emitted by all of the LEDs without creating an image of the diode array. In conjunction with the light guide, this efficiently diffuses the light as it delivers the light to the sample (Figure 12). Avoiding uneven illumination across the sample is very important to ensure that both the illumination light and measurement probe lights are interacting with the same surface of the sample.

Electronic Design

The fluorescence yield and absorption is measured from very brief (20-100 microsecond) pulses of measuring light without shuttering the actinic light. For this to work, the analog signal from the detector's photodiode is electronically filtered to reject high-frequency noise via a long-pass RC filter and reject the background fluorescence signal produced by the actinic light via a short-pass RC filter. The combination of long and short pass RC filters (aka a band pass filter) enhances the signal to noise ratio, but makes the precision of the electronic timing more important, for reasons described in the next section.

Precision Timing

The RC filters on the photodiode detectors dampen signals that are not associated with the measuring pulse, but the voltage signal of interest rises and decays during each measuring pulse rather than remain constant for the duration of the measuring pulse (Figure 13). Therefore highly consistent and precise timing of LED emitters and detector circuits is required, as any variation in the sampling time relative to the measuring pulse time will result in sampling different points on the curve of each measuring pulse and introduce noise to the recorded data.

Traditionally, accurate timing of electronic events is handled by a microprocessor, also known as a "microcontroller" or a "system-on-a-chip" (SOC). Microprocessors are inexpensive, ubiquitously available, and easy to program, but the requirement for jitter-free timing is problematic. The reason is that common microprocessor architectures do not include assembly instructions for waiting an arbitrary number of microprocessor clock cycles

before moving on to the next instruction in the stack. The usual approximation of a clock-cycle counter is a loop that constantly checks and increments an integer, but the overhead of the loop reduces the precision, especially if mixing timing controls on different timescales (in our case, we need to control the different interconnected electronic circuits on the second, millisecond, and microsecond time scales). Many microcontrollers contain timers that can be used to schedule code execution and thereby achieve accurate timing, but these timers work by interrupting the microprocessor, a process that introduces extra computation and can reduce the precision of the timing and may even introduce jitter. Another problem that is inherent in the design of all microprocessors is that RAM access is itself an assembly instruction whose execution time is indeterminate because high-speed RAM technologies (such as DDR RAM) have independent internal state machines that may or may not be ready to provide data when the microprocessor requests it. Thus consistently precise timing is simply impossible if the timing regime cannot be pre-loaded in its entirety into the lowest-level memory cache of the microprocessor. Even on a high-end desktop

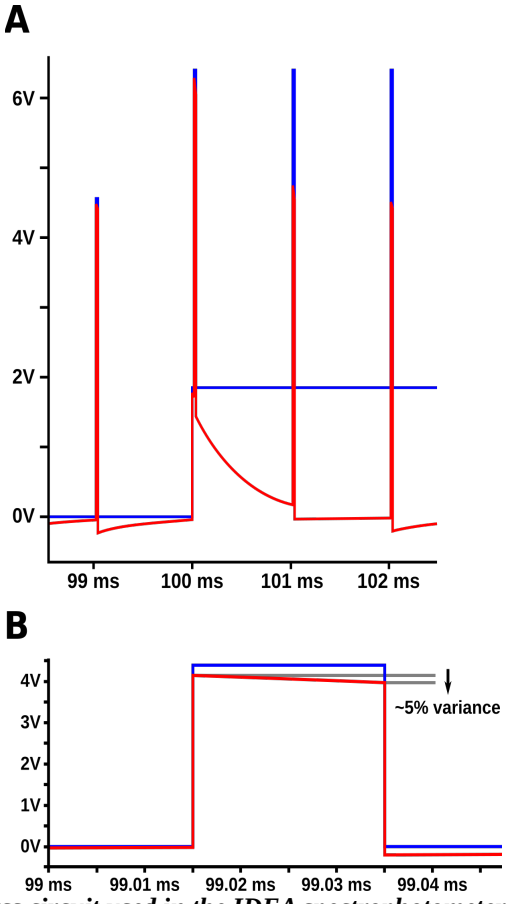

Figure 13: Simulation of band-pass circuit used in the IDEA spectrophotometer. *The unfiltered signal is shown in blue while the electronically filtered signal is in red. This filter preserves the transient changes caused by the measuring pulses while rejecting the changes in the background illumination after approximately 1 ms (panel A). During the simulated measuring pulse (panel B), the filtered signal droops by roughly 5% over 20 microseconds.*

computer, this cache is only a few megabytes in size and the cache of a microcontroller is rarely more than a couple kilobytes. For comparison, it is quite common to run experiments on the IDEA spectrophotometer with over 10,000 timing events, which would need a RAM cache of at least 640KB.

To meet the precise timing requirements for the IDEA spectrophotometer, I decided to use a field-programmable gate array (FPGA) instead of a microprocessor. FPGAs can be programmed to specify the exact digital logic to be executed on every cycle of the microchip's crystal oscillator, making it an excellent choice for time-sensitive digital circuitry.

The ChrisBlaster

Previously, the Kramer Lab had used a device called the PulseBlaster, purchased from Spin Core Technologies Inc., to provide the precise digital timing for the NoFoSpec. However, the PulseBlaster suffered from a few design flaws, most notoriously was the fact that it floated all of its output bits when unpowered, causing all of the lights controlled by the PulseBlaster to turn on at full power whenever the computer rebooted. This was more power draw than our power supply could handle and serious equipment damage has occurred on multiple occasions when the instrument computer rebooted unexpectedly.

I replaced the PulseBlaster with an FPGA program on a Nexsys 2 FPGA prototyping board purchased from Digilent Inc. and this replacement timing device came to be known as the ChrisBlaster. The design goals for the ChrisBlaster were as follows:

- Cycle 32 of the digital output pins through the digital output sequences specified in IDEA spectrophotometer protocols
- Provide jitter-free timing of the digital output sequences with the same precision and accuracy as the crystal oscillator driving the FPGA clock
- Equipment safety features such as having the digital outputs be grounded by default instead of floating
- Software interface that is easier to program than the PulseBlaster API

The ChrisBlaster met these goals with a design that could store up to 256 IDEA spectrophotometer protocols in the static RAM (SRAM) provided on the Nexsys 2 circuit board and then run them from the SRAM on command. The core of the design featured two digital output sequence stacks, dubbed Loopers, that could be loaded by the control logic with up to 256 digital output events. When active, a Looper module would repeat the stack of digital output events for a specified number of repetitions. When a Looper is done repeating its stack, the other

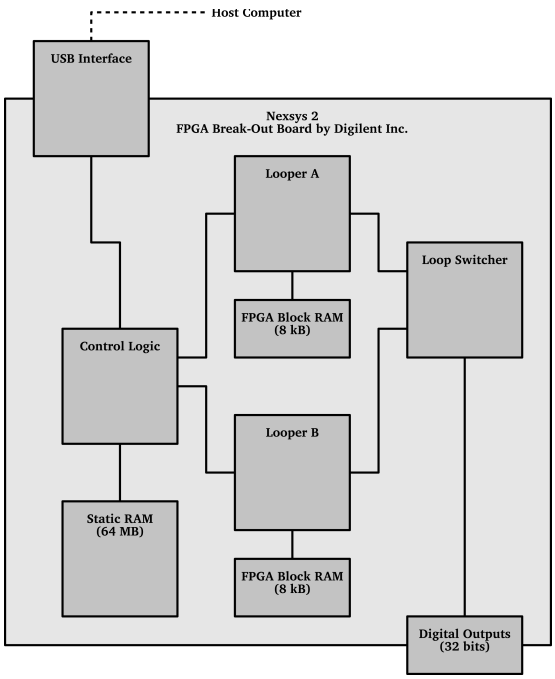

Figure 14: ChrisBlaster FPGA design schematic. *An on-board microcontroller forwarded the USB communications from the host computer to the control logic module. This module used a complex finite state machine to handle RAM access and process binary commands sent from the host computer via the USB serial stream. The sequence of digital output events was queued up in two identical "looper" modules so that one looper could run while the other was filled with the next batch of digital output events. The loop switcher module ensured seemless page-flipping between the two loopers and synchronized the bit changes to the clock oscillator for maximum precision.*

Looper is activated. Thus a Looper can be loaded with the next stack of digital output events without interrupting the sequence of digital output events controlling the hardware. The analogous technique used in computer graphics is called page-flipping[3]. A schematic of the ChrisBlaster FPGA program is shown in Figure 14. The ChrisBlaster software source code is included in Supplemental Files 1.

The ChrisBlaster times each digital output event by counting FPGA clock oscillations. Thanks to the parallel nature of the FPGA, changing digital outputs, incrementing the timing counters, and swapping Looper modules all happen simultaneously without introducing any delays. Because all of the logic is synchronized to the edges of the crystal clock oscillator, the timing of the bits will always be exactly as specified and is therefore jitter-free[4].

3 Page-flipping is an algorithm used in computer graphics where there are two graphics memory buffers for each screen. While the program is drawing images to one memory buffer, the other is sent to the screen. As soon as the program is done drawing to the buffer, the buffer memory pointer used by the screen is flipped to point to the newly filled buffer and the pointer used for the next draw cycle is flipped to the other buffer.

4 Jitter-free here means that there is no variance in the timing introduced by the digital logic of the design. The synthesizer tools used to program the FPGA predict that the internal transistors of the FPGA will introduce variance on the order of tens of picoseconds.

This ChrisBlaster design and Nexsys 2 FPGA was incorporated into the IDEA spectrophotometer and was also used to drive the timing of events in the Dynamic Environment Photosynthesis Imager (DEPI) prototypes and instruments (described in detail in Chapter 2).

The E-TADA

While the ChrisBlaster was quickly incorporated into a variety of instruments that also have precise timing requirements, it's utility and reliability were limited by several factors. The first problem I encountered in adapting the ChrisBlaster to other equipment was that the ChrisBlaster was tailored to the particular use-case of the IDEA spectrophotometer. IDEA spectrophotometer measurement protocols are divided into stacks, each of which contains only a few dozen digital output events and is repeated up to several hundred times before moving to the next stack. This led to a page-flip buffer design that closely matches the IDEA spectrophotometer protocols, but it does not easily allow for other timing models such as a FIFO queue or serial communication protocol. The ChrisBlaster also suffers from the fact that it relies on USB for communication. USB is an abbreviation for "Universal Serial Bus", but only the hardware behavior of USB is standardized to the point of universality. For a device that is not considered a human interface device (i.e. anything that is neither a mouse, keyboard, speaker, nor memory drive), there is no universal software driver[5]. Worse, we discovered that USB hardware is prone to losing its communication connection with the host computer when the USB cable is hit by the electromagnetic field produced by the high-power LED lighting system in the DEPI instruments. The final and most important driver for creating a ChrisBlaster successor was the discontinuation of the Nexsys 2 FPGA prototyping board.

With all of the above problems with the ChrisBlaster in mind, I set about designing the Ethernet-enabled Timing and Data Acquisition device (E-TADA). In additional to all of the design goals of the original ChrisBlaster, the E-TADA had the following additional goals:

- Constructed using only open-source hardware (and software) such that we could send the schematics to a manufacturer to produce it should our current suppliers stop production
- Communicate over ethernet LAN, which is designed to be fault tolerant and resistant to electromagnetic interference (Spurgeon 2000)
- Support for the I^2C serial communication protocol used by many off-the-shelf digital control circuits

5 The LibUSB project is an open-source library designed to provide a universal software library for writing USB drivers and USB to serial TTY drivers are now built into the majority or recent operating systems, so one could plausibly argue that these constitute universal USB drivers and therefore my claim regarding the absence of a universal driver is false. Even so, using these libraries is not simple and the increasing security restrictions on Microsoft Windows makes it ever more complicated to communicate with custom hardware via USB.

such as digital-to-analog converters

- Built-in support for a high-precision analog-to-digital converter microchip so that the E-TADA can acquire data as well as deliver precision timing (removing the need for additional USB hardware)

To meet these design goals, I came up with a design that incorporated the open-source Raspberry Pi microcomputer and the open-source Numato Mimas FPGA break-out board, using the MAX11100 ADC chip for analog data capture. In this design (diagrammed in Figure 15), the Raspberry Pi serves as the ethernet interface for the E-TADA and provides bidirectional I^2C communication backed by the internal hardware of the Raspberry Pi and the field-tested open source hardware serial drivers of the Raspberry Pi's Linux operating system. The Raspberry Pi also serves as the memory buffer for the E-TADA as it feeds the digital output events to the FPGA by high-speed Serial Peripheral Interface (SPI) protocol. Within the FPGA, the stack-based design of the ChrisBlaster has been replaced with a first-in-first-out (FIFO) queue. Digital timing events can be read from the front end of the FIFO while new ones are simultaneously added to the rear end.

The E-TADA uses ethernet LAN instead of USB, which was designed to handle EMP and connection

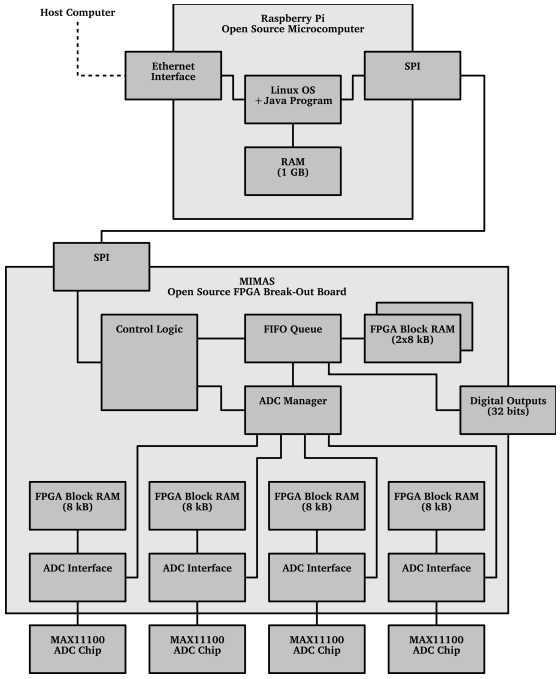

Figure 15: E-TADA design schematic. *Communication with the host computer over ethernet is managed by a Raspberry Pi microcomputer running a full Linux operating system. The program on the microcomputer uses the SPI connection to communicate with the FPGA. Since the microcomputer handles most of the memory management, the control logic module in the E-TADA is less complex than that of the ChrisBlaster. Digital output events are queued in a first-in-first-out (FIFO) data structure utilizing FPGA block RAM units. Four independent ADC manager modules can be physically connected to MAX11100 ADC microchips for up to four channels of analog data capture.*

disruptions without interrupting communication. The TCP and UDP network protocols used by the E-TADA are the same underlying mechanism for transmitting data across the entire internet as well as every home and business computer network. Few digital technologies have been so thoroughly tested and standardized. As such, no software drivers are needed to interface the E-TADA and the communication between the desktop computer and the Raspberry Pi uses human-readable JavaScript object notation (JSON), an open-source data format standard for which there are many high-quality open-source software tools.

A copy of the E-TADA hardware specifications and design are included in APPENDIX A. The full E-TADA software project is included in Supplemental Files 2.

Software Design

For all of the careful hardware design of the NoFoSpec and IDEA spectrophotometers, it is the software control that made these instruments the workhorses of the Kramer Lab. Experiments are scripted using a custom scripting language created by Prof. David Kramer. By using scripts instead of direct manual control, we are able to keep a library of scripted experiments to use and modify. Starting with a working script reduces the amount of time that it takes to setup an experiment and the automated nature of script execution reduces the manual labor involved in running a photosynthesis experiment and increases the precision of the experiment. Another important feature of the software is its graphical user interface (GUI). By seeing the data plots and data analysis while the experiment is still in progress, it is much more likely that the experimenter will catch a human or hardware error early enough that there is still time to salvage the experiment without compromising the sample or data.

Analysis Automation

It is simply too tedious to use a spreadsheet graphing program such as Microsoft Excel or Microcal Origin to hand-process the data traces from the spectrophotometers, although seeing the raw data is helpful in identifying equipment or experimental problems. I saved a great deal of time by writing my own data analysis software tailored to my most frequent IDEA spectrophotometer experiment. I chose JavaScript for my scripting language because its free-form object creation simplified the process of automating the formula-fitting portion of the data analysis. My formula fitting algorithm is not based on any particular theory, as I opted for an easily implemented “brute-force” approach that has sufficient performance on modern desktop hardware to home-in on the best fit formula within a second or two:

```
var fitFormula = {
    C: new Array(0,1,1), // coefficients Y0, A, and tau
    f: function(x) {
        return this.C[0] + this.C[1] * Math.exp(-1 * x / this.C[2]);
    },
    toString: function(){
        return this.C[0]+" + "+this.C[1]+" * Math.exp(-1 * x / "+this.C[2]+")"
    }
};

function improveFit(x,y,formula,delta, maxIterations){
    // adjust the variables by the delta amount in decrease the Chi-squared value
    var lastChi;
    var iterations = 0;
    do{
        lastChi = err(x,y,formula);
        for(var i = 0; i < formula.C.length; i++){
            var oldC = formula.C[i];
            var upC = formula.C[i]+delta;
            var downC = formula.C[i]-delta;
            var currentChi = err(x,y,formula);
            formula.C[i] = upC;
            var chiPlus = err(x,y,formula);
            formula.C[i] = downC;
            var chiMinus = err(x,y,formula);
            if(chiPlus < currentChi && chiPlus < chiMinus){
                // increase the variable
                formula.C[i] = upC;
            } else if(chiMinus < currentChi){
                // decrease the variable
                formula.C[i] = downC;
            } else {
                // no change
                formula.C[i] = oldC;
            }
        }
        iterations++;
    } while (lastChi > err(x,y,formula) && iterations < maxIterations);
    return iterations;
}

function err(x,y,formula){
    var sum = 0;
    for(var n = 0; n < x.length && n < y.length; n++){
        var t = x[n];
        var d = y[n];
        var sim = formula.f(t);
        sum += Math.abs(sim - d);
    }
    return sum;
}

var iterations = 0;
for(var l = 0; l < 10; l++){
    iterations += improveFit(xData,yData,fitFormula,0.1,1000);
    iterations += improveFit(xData,yData,fitFormula,0.01,100);
    iterations += improveFit(xData,yData,fitFormula,0.001,100);
    iterations += improveFit(xData,yData,fitFormula,0.0001,100);
    iterations += improveFit(xData,yData,fitFormula,0.00001,100);
    iterations += improveFit(xData,yData,fitFormula,0.000001,100);
}
```

Though the above formula fitting code is far from elegant and does not utilize any mathematical techniques that could improve performance, it was able to adequately extract the tau, initial slope, and amplitude parameters from my ECS DIRK traces. When I expanded the script to include automated file parsing and averaging, I was able to compute the Φ_{II}, NPQ, gH^+, and vH^+ at every measurement in one of my IDEA spectrophotometer experiments

(about 80 measurements over 2 hours) in less than 10 seconds and even create a summary spreadsheet with the average and standard deviations for experimental replicates. Before I wrote the script, this task would take me about 6 hours using spreadsheet software.

An IDEA spectrophotometer experiment script and its corresponding data analysis JavaScript are included in APPENDIX B. Supplemental Files 3 contains a complete project for the execution of data analysis JavaScript code.

Impact

More than a dozen IDEA spectrophotometers have been built, some of which have been shared with collaborators so that they can perform these measurements in their own laboratories. It is the go-to platform for photosynthesis measurements in the Kramer Lab (along with the DEPI chambers, see Chapter 2) and it continues to evolve as it is used to develop new techniques for measuring photosynthesis (such as the $NPQ_{(T)}$ presented in Tietz et al. 2017).

THE FUTURE OF PHOTOSYNTHESIS MEASUREMENT

In developing the IDEA spectrophotometer, it has become clear that there are technological limitations that need to be overcome for the field of photosynthesis research to make more significant advancements. These limitations fall into the categories of automation, scalability, and accessibility (Goff *et al.* 2011; Spalding & Miller 2013). Fortunately, there is progress being made in all of these fronts at Michigan State University and in the wider community of plant scientists.

Automation

We live in the Information Age, where most of the mundane details of life are handled by computers, from making coffee in the morning to paying the bills and soon even driving the car to work (Garling 2015). Yet much of our scientific research is still very hands-on. While that's unavoidable when pushing the envelope of human knowledge, nearly all of our tools are computer driven and the data is recorded in digital files. In my experience, very little labor is spent handling the sample compared to operating the instrument and analyzing the data (analyzing ECS data can be particularly time consuming). The challenge of automation is to get the most value out of the researcher's time by minimizing the amount of human input necessary to go from sample to results.

Automating an experiment requires unsupervised computer control over three kinds of tasks: running the experiment, validating the data quality, and analyzing the data. In the first category, running the experiment, the

solution is to make our scientific instruments scriptable. To this affect, the IDEA spectrophotometer and the NoFoSpec that came before it operate using a human-readable scripting language such that most experiments on these instruments only need infrequent human input to add chemicals or perform other wetware tasks. Yet they still fall short because the scripting language does not conform to any common standard (such as Python or JavaScript) and the recorded data is not automatically transferred to the experimenter's data analysis computer. A future iteration of this instrumentation will almost certainly include the ability to push data to a local or even cloud-based data server for instant access on the experimenter’s desktop computer.

Data quality control means knowing when a hardware failure or human error has compromised an experiment. Unfortunately, automating data quality control is a very difficult problem. Researchers with enough experience measuring chlorophyll fluorescence can often diagnose a problem with the hardware or experimental setup just by looking at the fluorescence data, but there is not yet a simple way to teach this kind of experience to a computer. Presently available machine learning software may be up to this task, but doing so would require a significant investment of time and technical expertise (Domingos 2012). Until then, the simplest way to check data quality is to compute the standard deviation of the analyzed results from several repetitions of an experiment. Assuming that the majority of experiments are conducted without problems (and no inherent flaws in the experimental design), then an unusually large standard deviation on a set of replicate experiments could indicate a problem in one or more of the experiments in that set.

Data analysis is often the most time-consuming step in performing an experiment, and fortunately it also is the easiest to automate. When I was using the NoFoSpec instrument to measure algal samples in a variety of conditions (including hyperoxia), I decided to write a program to run data analysis scripts written in the JavaScript language. These scripts shortened my analysis time per experiment from a few hours to less than a minute. While this was fantastically successful in increasing my productivity, my software was tailored to my own experiments and skill-set such that my colleagues were not able to use my analysis software on their own data. This anecdote demonstrates that automated data analysis can reap huge benefits but requires an investment of technical expertise to create a pipeline from data files to data results. Developing a more general-purpose solution will require a close collaboration between the laboratory and professional software developers.

Scalability

There is an increasing desire to study the interplay between multiple environmental factors on

photosynthesis. Teasing apart such multi-factor phenomena requires collecting a huge amount of data, either from a great diversity of conditions or from a huge number of plants, thus requiring an instrumentation platform that can be scaled up for high through-put (Spalding & Miller 2013). The barriers to scaling up are typically cost, trained labor, and data management (as discussed in Araus & Cairns 2014, Phillips 2010, and Goff *et al.* 2011). If the instrumentation is designed for automation (as described in the previous section), then the labor and data management issues are lessened.

Reducing the cost of scalability requires considerations towards both scaling-up and scaling-down instrument production. On the scaling-down side, rapid prototyping technologies, especially 3D printers, dramatically reduce the time and cost of developing an instrument from its first working prototype to something that can be reproduced. In this process, it is important to be able to rapidly go through several iterations of the design until it not only performs well but is also easy to assemble and use. When it comes to scaling-up, simple software/I.T. design decisions can make a big difference. For example, our NoFoSpec and IDEA spectrophotometers communicate with the controlling computer via USB while the environmental simulation photobioreactors (described in detail in Chapter 3) use ethernet. In theory, up to 255 USB devices can be connected to a single computer, but the electronic specifications for USB only support cable lengths of up to a few meters (Penttinen 2015) so in practice only a few instruments can be plugged into a single computer (and in reality, the present IDEA spectrophotometer control software only supports one instrument per computer), whereas ethernet communication can easily handle hundreds of devices spread across large distances (Spurgeon 2000).

Accessibility

High throughput experiments often collect more data than is strictly necessary to answer the original research question and there may be new insights hidden in the extra data. What the original experimenter considers to be noise may be a goldmine of information for a different kind of question. A famous example of this is the revolution in the field of asteroseismology brought about by the starlight intensity data from the Kepler Space Telescope; data which is little more than signal noise to those hunting for exoplanets (Koch *et al.* 2010). Another example is the discovery that the cosmic ray background in the MINOS neutrino detector in Minnesota correlates to the movement of the polar vortex (Osprey *et al.* 2009). Such discoveries are only possible because the large amounts of data collected by these instruments is stored in a database that is accessible to other researchers in a format that can be compared with other databases.

The trend to collect experimental data into online databases is going to continue and may soon be the default for data storage. In addition to enabling serendipitous discoveries, these databases enable the use of so called "big data" information processing algorithms (Domingos 2012). Technology giants like Google and Microsoft and many others have invested tens of billions of dollars (USD) in developing software that can scan huge amounts of data to pick-out associations that are too subtle or have too many variables to be found by a human mind (according to Google, Microsoft 2016b, Amazon 2016, and Domingos 2012). These efforts are now producing software products and services that could be used to mine science databases to perform virtual experiments with real data.

Another important component to making data accessible is allowing interested non-scientists to access and even contribute to the data. What these "citizen scientists" have to offer is their broad geographic distribution and the collective time that they can volunteer as the sum of many small time commitments. When it comes time to test a laboratory model of plant photosynthesis in nature, a community of citizen scientists can quickly expand the scale of the experiment across a whole country or even continent (Sullivan *et al.* 2014). Building such a community requires a savvy social media campaign, a continuous presence to keep people interested, and a research question that personally touches the community (Austic 2016). Getting usable data from the community also requires careful design of both the experimental procedures and the instrumentation involved so that it is user-friendly and accessible to the layman. For example, the PhotosynQ project developed an inexpensive portable plant fluorometry instrument based on the IDEA spectrophotometer and distributed hundreds of devices to their multinational citizen science community. The PhotosynQ instruments automatically upload all data that they collect to a website which is accessible to anyone (Kuhlgert *et al.* 2016). They have put research quality photosynthesis measuring tools in the hands of farmers and it is likely that this partnership between researchers and lay-people will yield discoveries that are not just profound, but also useful to people outside the scientific community.

CHAPTER 2: IMAGING PHOTOSYNTHESIS

The development of the dynamic environment photosynthesis imager chamber (DEPI chamber) started as a request to build a single-pot fluorescence imaging apparatus for Dr. Deserah Strand for use in an *A. thaliana* mutant screen. At the time, we were also actively developing the IDEA spectrophotometer (described in Chapter 1) and the environmental simulation photobioreactor (ePBR, described in Chapter 3), and there was a convergence of ideas: What if we could measure photosynthesis by chlorophyll fluorescence, like we do with the IDEA spectrophotometers, using a camera, like in this pot screener, in a simulated environment, like in the ePBRs?

From this convergence came a vision of a modified plant growth chamber that used computer controlled lighting and temperature to reproducibly replay outdoor weather in the growth chamber while watching the light reactions of photosynthesis adjust to these natural fluctuations in real-time. Realizing this vision pushed the limits of many technologies. We were operating outside the design assumption of the available digital cameras, driving more than 80 kilowatts through hundreds of high power LEDs, and commanding growth chambers to replay real-world weather. To make it all work in unison, I led a small team of programmers to create the control software. I designed the flow of control for the DEPI chamber and personally wrote the first prototype software module for each piece of hardware. Undergraduate computer science students Will Norman and Lee Wang made further improvements to the software after the hardware design was finalized. In addition, I worked with the electronics designers Robert Zegarac and Nathan Galbreath to interface the ChrisBlaster FPGA (described in Chapter 1), which synchronized the lights and cameras in the DEPI chamber.

Development on the DEPI chambers continues, but it has already transformed the way the Kramer Lab conducts plant research. In this chapter, I present this new technology along with the reasons for its development and our goals for future iterations.

THE NEED FOR NEW TECHNOLOGY

The previous chapter introduced the use of fluorometry and spectrophotometry to infer various aspects of the chloroplast electron transport chain in plant samples. The instruments used to conduct such measurements (e.g. the IDEA spectrophotometer) operate using only 1 to 3 photodiode detectors and thus do not provide any spatial information about the photosynthesis of the plant, potentially missing heterogeneous or development-dependent phenotypes. To get a figurative picture of photosynthesis in the whole plant, we need to take a literal picture of the whole plant.

Why Measuring One Leaf Is Not Enough

When using instruments that can only measure a single leaf at a time, leaf selection becomes a major source of bias, especially in plants with relatively small leaves such as *A. thaliana*. There will almost inevitably be a bias towards “easy to measure” leaves, which are typically more mature and farther from the center. While merely having such a bias can complicate the interpretation of the data, it also predicates your analysis on the assumption that the “hard to measure” leaves are of negligible importance. With imaging, however, all of the leaves visible to the camera are represented and thus the importance or non-importance of very young and very old leaves can be accounted for.

If set up properly, a fluorescence imaging system can perform its measurements without any physical contact between the instrumentation and the plants. The benefits of such a non-contact measurement are two-fold. First, by avoiding any mechanical perturbation of the plants, the plants will not activate any mechanically sensitive responses and therefore the measurement will not be biased by such behaviors. For example, many plant species close their stomata when jostled (Biddington 1986), possibly leading to an under-estimate of *in situ* carbon assimilation and linear electron flux (LEF) (Golding & Johnson 2003). The other major benefit of a non-contact imaging system is that the fluorescence measurements can be made frequently and at regular intervals, enabling the detection of transient phenotypes. One example of this is the 2014 report by Dr. Elham Attaran, which showed a short-lived interruption of LEF in *A. thaliana* several hours after exposure to the bacterial toxin coronatine (Attaran *et al.* 2014).

At the MSU-DOE Plant Research Laboratory, we sought to create a system that could manipulate plant growth environments to simulate natural natural environments (as well as artificially exaggerated environments) and simultaneously measure hundreds of whole plants with non-contact fluorescence measurements. To this end, we designed and built a system of cameras and LEDs to perform high throughput fluorometry measurements in a plant growth chamber.

Application of IDEA Spectophotometer Techniques to High-Throughput Imaging

Despite the technical differences, measuring the light reactions of photosynthesis by fluorescence imaging is very similar to fluorometric techniques employed by the instruments described in Chapter 1. In essence, you can consider every pixel in the fluorescence image sequence to be like an individual fluorometer data trace. Plotting the value over time for a single pixel (or a region of pixels) will even produce the familiar F_S+F_M curves produced by

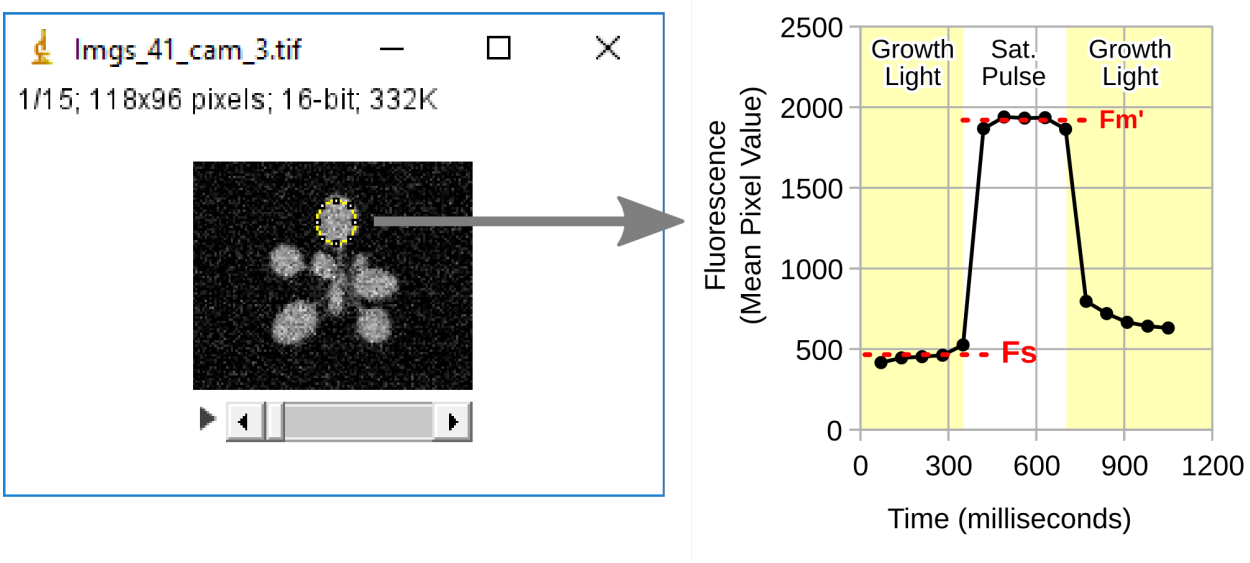

Figure 16: Relationship between DEPI camera images and fluorescence parameters. *The first image of a series of 15 fluorescence images for a single* Arabidopsis thaliana *pot (left) was cropped from an image set containing 32* A. thaliana *pots. Using the image analysis program ImageJ, one leaf was selected (represented by a yellow oval) and the fluorescence intensity of that leaf was plotted over time during the course of a single Φ_{II} measurement (right). During the measurement, the background light started at growth light intensity, then increased to a saturating light intensity, and then returned to the growth light intensity. The extrapolated fluorescence parameters F_S and F_M' are marked in red.*

instruments such as the IDEA spectrophotometer (as shown in Figure 16).

Calculating photosynthetic parameters such as Φ_{II} and NPQ from a series of images involves performing "image math". Essentially, image math involves taking a sequences of images over time, assigning a numerical value to each pixel (i.e. the brightness value of the pixel), and then generating a new image where each pixel's value is the result of applying mathematical operations to the corresponding pixels on different images in the image sequence. For example, an "image multiply" operation, such as C = A×B, would involve multiplying each pixel in image A by the value of the pixel in image B with the same (X, Y) coordinate and then saving the result as a pixel in image C. There are software tools such as ImageJ (used in Figure 16) that are specialized for performing image math.

The algebraic formulas are the same as described in Chapter 1 (summarized in Table 1).

Accounting for Plant Growth and Movement

Plants are not stationary and as they grow and bend, any image-based measurements of the chlorophyll fluorescence is going to suffer from the fact that the same pixel in two different measurements may no longer be measuring the same portion of the leaf. This becomes especially problematic for the calculation of non-photoreductive quenching (NPQ) because the calculation typically references the dark acclimated maximal

Fluorescence Parameter	Calculation	Leaf Movement Artifact
Φ_{II}	$(F_M' - F_S) \div F_M'$	No
NPQ	$(F_M - F_M') \div F_M$	Yes
q_E	$(F_M'' - F_M') \div F_M'$	Yes
q_I	$(F_M - F_M'') \div F_M'$	Yes
$NPQ_{(T)}$	$4.88 \div ((F_M' \div F_0') - 1) - 1$	No
$q_{E(T)}$	$NPQ_{(T)} - q_{I(T)}$	No
$q_{I(T)}$	$4.88 \div ((F_M'' \div F_0'') - 1) - 1$	No

Table 1: List of commonly used fluorescence parameters that the DEPI system can measure. *This table shows each of the formulas used to calculate these parameters and whether or not each parameter is distorted by leaf movements on the minutes timescale.*

fluorescence (F_M) that can only be measured once at the start of the day. The solution to this problem is to use the "theoretical" calculations such as $NPQ_{(T)}$ (described in Chapter 1, see also Tietz *et al.* 2017). These alternative calculations eliminate the need to reference fluorescence images taken at different times so long as the leaves are effectively stationary over the course of the one-second fluorescence measurement.

Dynamic Environment Simulation vs a Plant Growth Chamber

The growth chambers commonly used for growing *Arabidopsis thaliana* and other common lab plant species were designed to maintain a static environment with relatively low growth light intensity on a simple on-off diurnal cycle. Natural environments, however, are highly dynamic, and as a result photosynthetic organisms have evolved a number of protective mechanisms to cope with fluctuations in the environment (reviewed in Kanazawa & Kramer 2002, Cruz *et al.* 2005, and Murchie & Niyogi 2011). Some of these mechanisms appear to be redundant or unnecessary in a laboratory environment, yet their absence causes a substantial increase in plant mortality when transplanted to outdoor cultivation. Such is the case for the *A. thaliana* mutants lacking the PGR5-mediated cyclic electron flux pathway (Suorsa *et al.* 2012).

THE DEPI CHAMBER

The ultimate design goal of the Dynamic Environment Photosynthesis Imager chamber (DEPI chamber) was to be able to monitor the light reactions of photosynthesis in real-time as the plants continuously adjusted their photosynthesis to survive in a fluctuating environment. This meant developing novel hardware and software systems for both the environmental controls and the fluorescence image data collection.

The Growth Chamber

The DEPI chamber has been designed around two models of commercially available plant growth chamber. For relatively small scale experiments (e.g. imaging a dozen or so *A. thaliana* plants at a time), we use Model-I

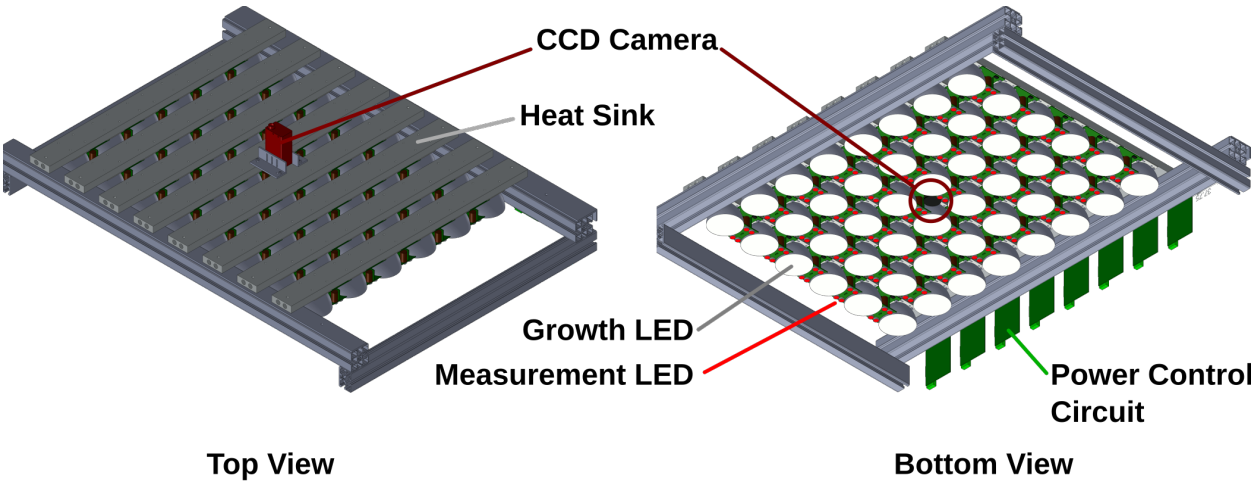

Figure 17: Diagram of DEPI solid-state lighting system. *LED circuit boards are attached to the underside of hollow aluminum heat-sinks which are designed to allow chilled water to flow through the internal space for efficient heat dissipation. The LEDs are arranged in series on each each heat-sink with larger white growth light LEDs surrounded by smaller red measurement pulse LEDs. At the end of each LED series is a power control circuit board, which contains a microcontroller that stores the necessary calibration data to convert the requested light intensity to the appropriate power draw for that particular series of LEDs. CCD cameras (only one is pictured above) are situated to extend between the heat-sinks and LED optics for a clear view of the planting area.*

series incubators by Percival-Scientific, and for larger scale experiments (e.g. hundreds of *A. thaliana* plants at a time), we use BigFOOT™ series plant growth chambers from BioChambers. All of our hardware is installed directly inside the chamber in the place of the growth chamber's original lighting system.

Lighting System

The key to successfully measuring the chlorophyll fluorescence with the DEPI chamber is its lighting system. In order to provide IDEA spectrophotometer style measurements to the chamber, the whole chamber must be lit-up with high-power fast-switching LEDs. To approximate outdoor weather, the continuous growth light needs to be white and needs to be able to maintain an illumination intensity of at least 2000 µmol photons/m^2/s (10-20 times brighter than what the growth chambers would normally provide). Furthermore, the F_M' fluorescence measurement requires an illumination intensity that is another ten-fold brighter, all the while still having the ability to shutter the light for microseconds at a time.

Solving this daunting technical challenge required installing dozens of aluminum heat-sinks and hundreds of high-power LEDs per chamber (pictured in Figure 17), with a peak power draw for the whole LED array on the order of a few dozen kilowatts. Each aluminum heat sink is lined with white (growth-light) and red (measuring pulse) LEDs and is cooled by chilled recirculating water. Since the power draw during the saturating light pulses far

exceeded the allowance of the building's power lines, we used an array of lead-acid batteries (12 watt-hour storage capacity) to buffer the DC power supplies for each DEPI chamber. High-power transistors and FPGA timing (using a ChrisBlaster device) enabled rapid and precise light intensity changes with a switch time of less than 20 microseconds.

Fluorescence Image Capture

The cameras used in the DEPI chamber are not standard RGB cameras. Aside from the fact that we want to measure fluorescence in the far-red spectrum rather than visible light, typical cameras also lack the sensitivity and bits-per-pixel resolution to adequately quantify the fluorescence. Instead, we use 12-bit gray-scale cameras (purchased from Hitachi and Allied Vision Technologies) and installed a RG-9 optical filter over the camera lens to filter out the visible light. To ensure that the cameras perform their image capture at precisely the right time, their exposure is set to externally trigger from a wire connected to the FPGA timing device.

In theory, the sequence of events would be the same in fluorescence imaging as in the IDEA spectrophotometer. However, the limitations of present camera technology introduce some additional complications. In particular, the IDEA spectrophotometer's detectors use electronic RC filtering to allow them to sample the fluorescence signal caused by the measurement pulse without shuttering the growth light. CCD and CMOS cameras, however, have no such filtering on their photodetector elements. Thus the pixels of the fluorescence imaging camera can only record the absolute light intensity value for each pixel. To get data that is comparable across multiple light

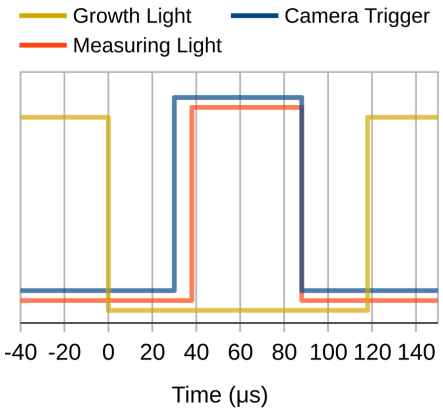

Figure 18: Timing diagram of light and camera events during a single measuring pulse. *To take a picture of the steady-state fluorescence, the growth light is disabled and the camera is left in the dark for approximately 30 µs to allow time for the CCD to discharge background noise that accumulated in the light. Then the camera trigger wire is set and another brief delay is introduced to account for jitter in the camera's image exposure start time. Then the measuring pulse is activated for 50 µs exposure time. Another dark period provides time for data read off the CCD before the growth light resumes.*

intensities, we opted to briefly shutter the growth light and use a pulse of fixed-intensity measurement light for each frame exposure of the camera. Building this capacity into the lighting system introduced considerable complexity into the hardware design and necessitated the inclusion of a precision timing device (such as the ChrisBlaster or the E-TADA) to precisely synchronize all of the light change and camera capture events (timing of events described in Figure 18).

Yet shuttering the growth light posed another problem for the cameras. In most camera applications, the viewing scene is either always brightly lit or is relatively dark between image captures and brightly lit only during image capture (e.g. a camera flash in a dark room). This is the assumption that went into the design and manufacture of the hardware inside practically all cameras, but our circumstances reverse this assumption: We have a brightly lit growth chamber and want to briefly shutter the growth light to take a picture illuminated only by the comparatively dim measurement pulse (i.e. a dark picture in a brightly lit room). Even with optical filters blocking the most of the growth light from the camera, enough growth light and steady-state chlorophyll fluorescence gets through the filter between pictures to stimulate the camera's detector (especially during the saturation light pulse) and the brief time between shuttering the light and starting the image exposure is not always long enough for the CCD to clear the "after-image". This introduces an artifact that resembles the vertical blurring iconic of a CCD camera pointed directly at a bright light source. Ultimately we could not reliably prevent this artifact and opted to mathematically remove the artifact by subtracting "background" reference images taken without activating the measurement pulses (as shown in Figure 19).

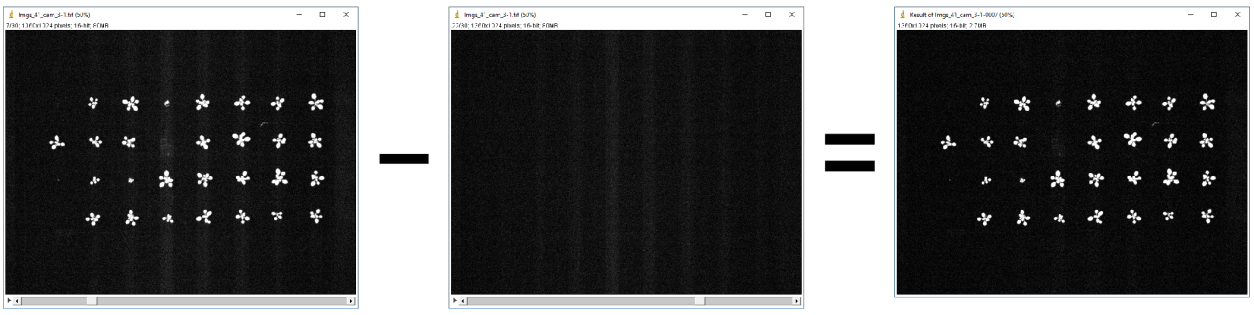

Figure 19: Removal of CCD "after-image" artifact by background subtraction. *When the background light is very intense, such as during a saturation pulse, the CCD cameras retain a residual "after-image" signal from the camera's view prior to the initiation of formal image exposure, appearing as faint vertical bands (left). A followup exposure taken with identical background light, but without the measuring light pulse, captures an image containing only the artifact (center). Performing a pixel-by-pixel subtraction of the artifact image (center) from the measurement image (left) produces an artifact-free image (right).*

Control Software

The software had to fulfill three challenges: first, reliable and precise control of the hardware to produce quality data; second, prepare and transmit the collected data for automated analysis; and third, provide a user interface for the scientists designing the experiments that is intuitive and flexible enough to create the experiments necessary for answering the interesting biological questions.

Reliability

We found it particularly challenging to achieve reliable operation of the cameras. Even in mundane usage, digital camera devices have a number of complex subtleties that must be accounted for in their operation, such as gamma settings and electronic shutter options (Allied Vision Technologies GmbH 2017). Our application of these cameras strays far from "normal" operation and therefore we had to contend with details that wouldn't normally be problematic (such as the "after-image" artifact described previously). Our approach to address these challenges was to separate the camera operation component of the software to its own sub-process that could be tested separately from the rest of the software and written in a different programming language that is more suited to low-level

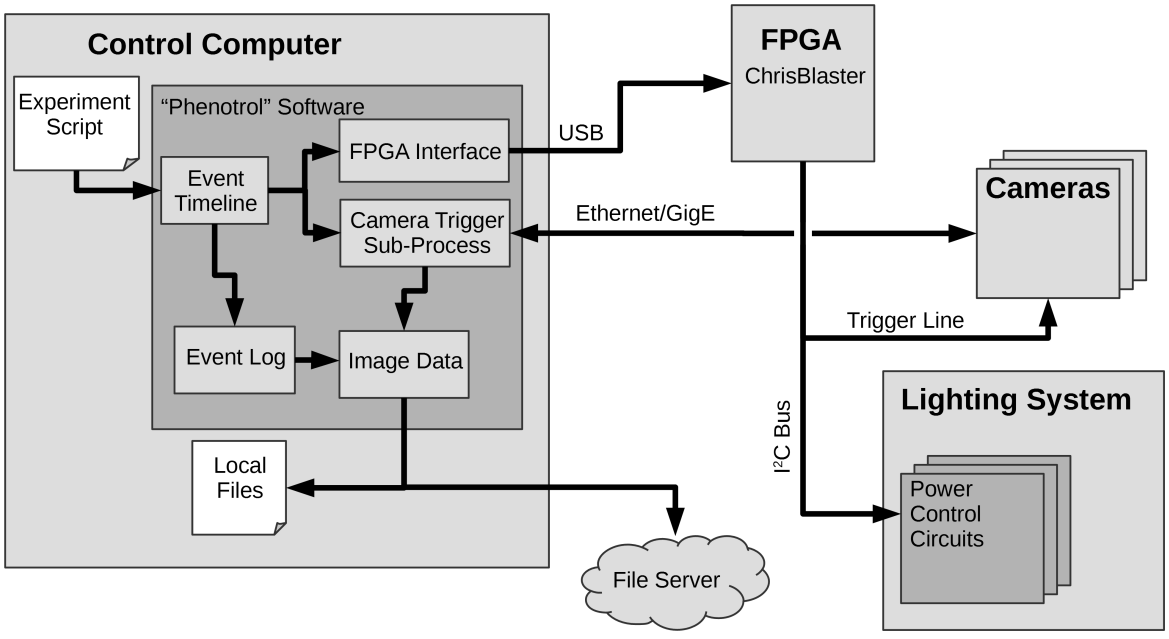

Figure 20: Diagram of software control in the DEPI system. *The direction of the arrows indicates flow of data from one component to another. Starting from an experiment described in JavaScript notation, the script is processed by the "Phenotrol" program to generate a timeline of scheduled events. This timeline is used to coordinate the ChrisBlaster FPGA board and the cameras to ensure that the lights (and other environmental controls) change as intended and collect data. The schedule of events is recorded in an event log file which can be parsed by data analysis software and this file is bundled together with the image data. The data is then saved onto the local file system of the computer and also uploaded over the local area network to the data analysis file server.*

optimizations (C++ programming language).

Figure 20 depicts the logical organization of the DEPI chamber control software.

Data Analysis

Part of the challenge of designing the data pipeline from DEPI chamber to analysis was the simple fact that we were developing the data analysis infrastructure from scratch at the same time as we were running experiments for scientific publication. This meant that it was vital that the data from an experiment be stored in a format conducive to both manual processing as well as automated processing. As such, it was decided that the sequence of images that constituted a single measurement would be collated into a single multi-page TIFF image. The TIFF images would be named for their chronological order in the experiment and stored with in an organization of files and folders that segregated the images by date and camera (as shown in Figure 21). This way, someone could easily import a day's worth of images for a single camera view into the image analysis program ImageJ for manual

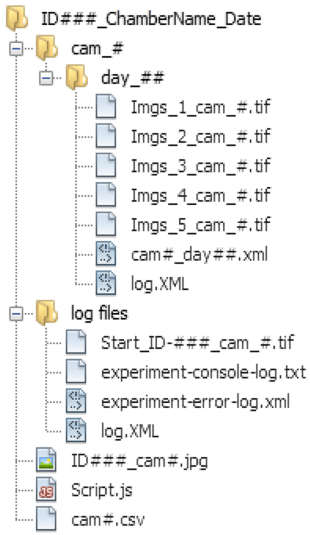

Figure 21: File structure of a DEPI experiment. *Note that # represents a camera number, ## represents a day number, and ### represents the experiment ID number. The .tif files are individual fluorescence measurements, where each file contains a series of 16-bit grayscale such as is presented in Figure 16.The .xml files contain the event log, which is either just the events relevant to the particular day (cam#_day##.xml) or the total of all events over the course of the experiment (log.XML). The ,jpg file contains a sample image taken at the start of the experiment to provide a convenient look-up of plant alignment. Script.js is the experiment described in JavaScript (filename will be actual name of the script file used), and cam#.csv is the selection file used to automatically associate each plant in the image with its identification information (e.g. accession ID or mutant name).*

analysis, and then apply the ImageJ analysis script from that view to the rest of the data set. After manually tweaking a ImageJ data analysis scripts to work reliably over several experiments, they were then incorporated into the development of new automated data analysis software specialized for the DEPI chamber.

User Interface

Like the NoFoSpec and IDEA spectrophotometer, the DEPI chamber was intended for script-based autonomous control. These scripts fell into two categories of dynamic environments: natural environment simulations and exaggerated stress environments. The main difference between these two types of experiments, from the perspective of the control software, is that natural environment simulations generally read from a schedule while an artificial environment tends to use a mathematical definition of the environment as a function of time. Credit belongs to computer programmer William Norman (an undergraduate whom we hired to assist in software development) for coming up with a strategy to cater to both of these types of experiments with the same script interface. William's solution was to separate the execution of the scripted experiment from its execution with an intermediary timeline data format. Thus "running" a script would generate a scheduled timeline of events (even for mathematical artificial environment). This timeline could then be visualized with graphs of light intensity and other environmental values to help the experimenter spot any bugs in their script (an example of this is shown in Figure 22). This separation also ensures that script bugs do not crash the control software mid-experiment (a common problem when working with the IDEA spectrophotometer).

The DEPI experiment script itself is a JavaScript file with DEPI chamber specific functions. JavaScript was

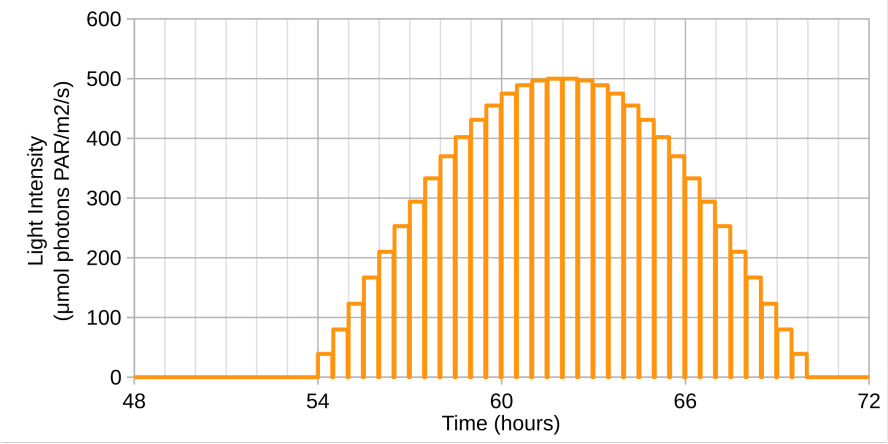

Figure 22: Illustration of a DEPI timeline. *When a DEPI experiment script is "compiled", the JavaScript engine inside the control program generates a schedule of events over time. In the above example, the light intensity component of a timeline for the third day of an experiment is shown. This day in the experiment features a sinusoidal approximation of a day-night cycle with light intensity changes every half-hour. The light intensity if brought to 0 for two minutes before each light change in order to acquire a F_M'' measurement for q_E calculations.*

chosen for this purpose because it is a relatively easy programming language for new DEPI chamber users to learn and was conducive to the development of web-based script generators which could generate functional DEPI chamber scripts from a graphical interface. The graphical interface is still a work in progress but we hope that it will be intuitive enough for a DEPI chamber user to be able to create an experiment without having to learn the JavaScript programming language.

FUTURE DESIGN GOALS

Building the DEPI chambers has always been a difficult balance between what kinds of experiments would generate the most interesting data versus the hardware and software that we could realistically build and operate reliably. From its current iteration, there are three distinct directions that we would like to develop further: scaling-up, more comprehensive environmental simulations, and 3D image analysis.

Scaling-Up

At present, the DEPI system is optimized for the model plant *Arabidopsis thaliana*. This decision was made for two reasons, the first being that it is the most common model for basic photosynthesis research and has a well-developed catalog of mutant libraries. But the second reason for focusing on *A. thaliana* was that it is essentially a 2-dimensional plant. Except when it is flowering, *A. thaliana* lies flat with its leaves horizontal. In the future, we want to apply the same DEPI techniques to crop plants, which ultimately are the plants that matter the most to the public.

The biggest challenge to assaying crop plants in the DEPI system is their physical size. Larger DEPI chambers are needed to assay the same number of crop plants as we presently can achieve with *A. thaliana*. Making the chambers larger increases the cost and potentially the complexity of the LED lighting system and the camera optics. This is especially true for tall plants such as camelina, wheat, or maize. Not only do tall plants require more vertical space, but they sway more with the air currents within the chamber. Techniques that rely on a daily reference image, such as the traditional NPQ calculation, simply cannot be used on tall plants as the leaves are not in the same location (or even orientation) with each measurement.

Even without accommodating new plants, substantially larger DEPI chambers could be a big breakthrough for *A. thaliana* DEPI experiments. Our large 5-camera BigFOOT™ DEPI chambers can simultaneously assay a few hundred young *A. thaliana* plants. This is enough to characterize the photosynthetic phenotypes of many mutants in parallel, but if the plant number could be increased to a few thousand plants at a time, then it would become feasible to screen entire libraries to characterize the photosynthetic phenotype of every gene knock-out in the whole *A.*

thaliana genome. Such a project would likely reveal as of yet unidentified interactions between photosynthesis and other plant processes.

A More Comprehensive Environment

The DEPI system has been used to discover new photosynthetic phenotypes by simply fluctuating the lights, yet light intensity is just one of several environmental parameters that are constantly fluctuating in a natural environment. The obvious next environmental parameters to add to the DEPI system are dynamic temperature and humidity control. These controls were part of the original DEPI specification, but are not yet fully implemented. Part of the problem lies in how growth chambers work. Many models cannot independently control the temperature and humidity as they use the air-conditioning unit to de-humidify. It is also vitally important to avoid condensation on the electronics to avoid damage to the DEPI system. Yet these problems are solvable, and we hope to eventually deploy a DEPI chamber that has dynamic independent control over temperature and humidity in addition to the lights. Such a chamber would then be able to replay recorded weather, allowing for an in-depth look at what features of a particular growing season caused the plants to be limited by photosynthesis and then test various treatments or mutations alleviate that limitation. A weather-playing DEPI chamber could also be used as a small-scale field trial, though the price-tag of the chamber might be greater than the cost of a standard outdoor field trial.

Another area where the current DEPI design could be improved is in the quality of the light. Presently, DEPI chambers use “cool-white” LEDs for the growth light. The light spectrum of these LEDs contains very little far-red and zero ultraviolet. Many plants use far-red to signal developmental changes such as flowering time and shade-avoidance (reviewed in Ballaré & Casal 2000 and Mockler *et al.* 2003). For one-week experiments, the lack of far-red is not a problem, but in longer experiments, the lack of far-red leads to abnormal development, especially when dealing with plants other than *A. thaliana* (as discussed in Lund *et al.* 2007). On the other side of the light spectrum, ultra-violet light presents a source of damage that outdoor plants must protect against. UV-B has been shown to be particularly damaging to photosystem II (Sicora *et al.* 2003), so our present estimates of photodamage based on our UV-free DEPI chambers may be under-estimations of what our plants would accumulate under equivalent outdoor conditions.

Another environmental control we would like to integrate, for practical reasons as much as for scientific ones, is automated watering and soil moisture detection. On the practical side, this would reduce the amount of manual labor required to run long-term experiments by keeping the plants watered without the need to open the

chamber. With one fewer experiment maintenance tasks, there would be one less point of failure. On the scientific question side, one of the biggest challenges facing agriculture today is the increasing frequency of droughts and dry weather due to global warming (as discussed in Adams *et al.* 1990 and Morton 2007). If automated watering was built into the DEPI system, then it would be possible to induce drought stress and examine how the plants respond to different soil moisture conditions. Even if this does not yield new insights into how to make plants more drought tolerant, it will reveal drought-associated photosynthetic phenotypes that could potentially be used to develop new remote-sensing applications for early-stage drought stress detection.

3D Imaging

The DEPI system provides a 2-dimensional picture of photosynthesis over time in a simulated environment. *A. thaliana* happens to be a 2-dimensional plant, but most plants are not. In the case of crop plants, the 3-dimensional architecture of the leaf canopy is particularly important, and many of the yield-improvements made in the past few decades were the result of breeding crops to optimize leaf canopy cover (to maximize area coverage and minimize leaf overlap) (Evans 1980). Yet a key question from the plant breeder's perspective is: how do you improve the net photosynthesis of the whole canopy? (discussed in Evans 1980 and Zhu *et al.* 2012) The first step towards answering this question would be to be able to measure whole-canopy photosynthesis. Modeling experiments have shown that the leaves beneath the top layer of foliage must be considered to arrive at an accurate measure of canopy photosynthesis (Wang & Leuning 1998), but the present DEPI system cannot see through the top layer to asses the photosynthetic activity of shaded leaves. If the DEPI system could image photosynthesis throughout the canopy in a stand of growing crop plants, then it could begin to answer this pressing question.

Imaging in three dimensions is not a trivial task and the bulk of the burden lies on the analysis software to make it work. In principle, all the DEPI system needs to do to have a 3-dimensional image is to take overlapping pictures from multiple angles (as described in Park & Subbarao 2005). The algorithms for doing this, however, are complex and require a lot of computation, especially if the exact position and orientation of all the cameras is unknown or subject to variation. Fortunately, there are many software companies who have already developed the expertise in 3D reconstruction, so it is likely that a partnership with such a company would be able to quickly add this feature to a DEPI system when we decide to go down this route.

CHAPTER 3: SIMULATING ENVIRONMENTS IN THE EPBR

In the previous chapter, I emphasized the point that it is important to grow and measure plants in an environment that is representative of the real world in order to better understand their photosynthetic behavior. This is even more true for microalgae, whose generation time is measured in hours rather than weeks. In the Kramer Lab, we were particularly interested in studying the relationship between an algal strain's photosynthetic efficiency and its performance in a commercial production setting. We soon discovered that none of the existing algal cultivation techniques or photobioreactors were suitable to this task, so we set out to create our own and share it with our collaborators in the National Alliance for Advanced Biofuels and Bioproducts (NAABB) consortium.

The core of the photobioreactor design team consisted of Ben Lucker, Robert Zegarac, and myself. I was in charge of designing the control systems for both the internal operation within each photobioreactor and the control of multiple photobioreactors by a desktop computer. My firmware and software design informed the design of the electronics by Robert Zegarac. Ben Lucker designed the physical hardware and requested specific features that he wanted to see in the software. After we were satisfied with the design and had built several generations of prototypes, we co-founded the company Phenometrics Inc. to produce and sell our photobioreactor to laboratories around the world.

In this chapter, I present our new photobioreactor, the ePBR, along with the rational for developing the ePBR and a discussion of various uses for the ePBR.

NEED FOR STANDARD CULTIVATION PLATFORM

While the procedures for growing common laboratory plants have become fairly consistent across the field of plant research, microalgal cultivation can vary considerably between different labs. As an aquatic micro-organism, many microalgal techniques share more in common with bacterial cultivation than with plant cultivation, and as a result many microalgal cultivation systems are little more than standard microbial growth systems with additional lighting. With such variation, it can be difficult to compare the results of similar experiments conducted in different laboratories, especially when the experimental question relates to light intensity.

Common Microalgal Cultivation Systems

Much of the established literature on microalgal photosynthesis was performed in batch cultures housed in whatever labware happened to be easily available. For university laboratories, this usually means Erlenmeyer flasks. The Erlenmeyer flask cultivation system is relatively simple, consisting of several flasks of liquid culture sitting

beneath a fluorescent lamp, each stoppered with foam or gauze punctured by a pipette to bubble filtered air through the culture medium. For a fast-growing microalga such as *Chlamydomonas reinhardtii*, a flask generally takes about a week to grow from inoculation to stationary phase density (Anderson 2005). However, it is difficult to precisely define the environment experienced by the algae in the flask, with its curved walls, diffuse lighting, the shading of the stopper, and a bubbling rate that may or may not be constant. An Erlenmeyer flask growth experiment, therefore, is only comparable to other Erlenmeyer flask experiments with a nearly identical setup, and not comparable to other culture systems or natural environments.

Another cultivation system is the 2-liter bottle culturing system, which is primarily used by aquarium fish and bivalve breeders to produce microalgae as food for other organisms (instructional tutorials found in Fischer 2008 and Marc 2013). In this case, the cultivators are not working in a fully stocked wet-lab and thus purchasing standard lab glassware would be an unnecessary expense. Instead they fill 2-liter soda bottles with culture medium and illuminate from the side with fluorescent lamps. When temperature control is needed, the bottles are submerged in a temperature-controlled water-bath (with transparent plexiglass walls). Compared to other culturing techniques, the soda bottles have the advantage of being cheaper than Erlenmeyer flasks and the water bath allows for experiments to be carried out at temperatures other than room temperature. However, like the Erlenmeyer flasks, it is difficult to define the light environment within the culture, so while the adding a temperature controlled water bath can make this system closer to a natural environment than an Erlenmeyer flask setup, it's light environment is still not well defined.

Plastic bag photobioreactors are used when very large quantities of microalgae are needed. Essentially, this is a tubular plastic bag filled with culture medium and inoculated with algae and then hung from a rack to grow either under artificial light sources (Lehmann *et al.* 2013) or outdoors (Rodolfi *et al.* 2009). When hung outdoors, these bags experience the full range of natural environmental fluctuations. This makes the plastic bag photobioreactor roughly equivalent to using a greenhouse for plant cultivation. However, plastic bag photobioreactors tend not to be used for lab bench scale experiments because it is very difficult to control the environment of a plastic bag photobioreactor. Thus plastic bag photobioreactors may be good for testing outdoor behavior in a strain, but are not good for predicting outdoor behavior based on a laboratory scale experiment.

All of the fore-mentioned cultivation systems require a bit of hand-waving when describing the environment in those systems as experienced by the individual alga. To solve this particular problem, the flat-panel

photobioreactor was invented (Photon Systems Instruments). In the flat-panel photobioreactor, the algal culture is sandwiched between two transparent walls with a short optical path length between them. Light from a matrix of LEDs illuminates the photobioreactor through the transparent panes and a steady stream of gas bubbles along the edge simultaneously provides gas exchange and mixes the culture via the air lift principle (airlift mixing is described in detail in Kiese et al. 1980). In essence, the flat-panel photobioreactor cultivates the algal culture in the shape of a leaf. The main benefit is that the light environment is clearly defined and easy to control and manipulate. With this system, one can define a natural (or artificial) environment from the perspective of an individual alga and then set the flat-panel photobioreactor to mimic that environment. On the other hand, this system may be simplifying too much. Microalgae do not naturally grow as a leaf and the gradient of light through their culture is an important feature of their environment. Whether the lack of a light gradient is a benefit or a problem depends on whether one is more interested in the behavior of the algae as individuals or of the culture as a whole.

"Natural" vs Lab Environment

One of our goals with the new platform was to be able to cultivate the algae in an environment that is comparable to an outdoor "natural" environment. Of course, the meaning of "natural" is very much dependent on context. An ecologist studying phytoplankton might define a "natural environment" as one that features a low-density of algae growing in a deep water column wherein mineral nutrients are growth limiting (Bainbridge 1957; Coale *et al.* 1996). A civil engineer who wants to use algae to clean-up nitrogen pollution from wastewater might instead define a "natural environment" as one that resembles a wastewater treatment pond or perhaps an urban storm drain system (Buhr & Miller 1983; Su *et al.* 2011). In our particular case, we are working in collaboration with algal

Figure 23: A lab flask full of* Chlorella sorokiniana *culture next to a decorative pond. *Both are rich in algae.*

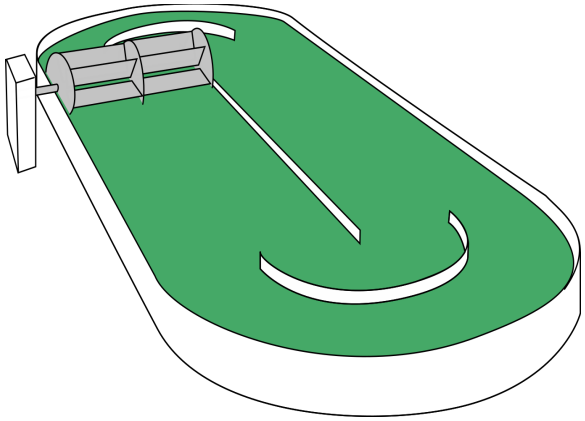

Figure 24: Drawing of a raceway algal production pond.

biofuel production laboratories through the NAABB consortium, so for us, the reference "natural environment" is that of a commercial algal production pond, such as a raceway pond (reviewed in Becker 1994 and Anderson 2005) like the one drawn in Figure 24. These ponds tend to be relatively shallow (typically less than 30 cm in depth), enriched with supplemental inorganic carbon (Ci), and the algae are cultivated to very high cell densities. Naturally these production ponds are outdoors, and thus are subjected to fluctuating light and temperatures as per the weather on any given day.

Unlike the static laboratory environment that is typically used to cultivate the algae, a core feature of all of the above descriptions of a "natural environment" is the fact that the algae must contend with an ever-changing environment. We have a particular interest in examining photosynthesis in such a fluctuating environment because the light reactions of photosynthesis contain a variety of protection mechanisms that operate on different timescales, including non-photoreductive quenching, light-harvesting complex dissociation (aka state transitions), protein repair, and changes in the photosystem stoichiometry (reviews of these processes can be found in Cruz et al. 2005, Wollman 2001, Aro et al. 1993, Cirulis et al. 2013, and Dietzel et al. 2008). Under static laboratory conditions, these protection mechanisms appear to have redundant or overlapping functions, but considering the differences between these different mechanisms may be important in a fluctuating environment.

The Importance of Geometry

The light environment in a production pond features a severe light gradient from the surface of the culture down to the bottom. This is a natural consequence of the fact that the culture is largely planar and the sunlight illuminating the production pond is highly collimated. Some have proposed that this light gradient is a major source of inefficiency, as the algae at the surface are experiencing sunlight intensities in excess of the light saturation point

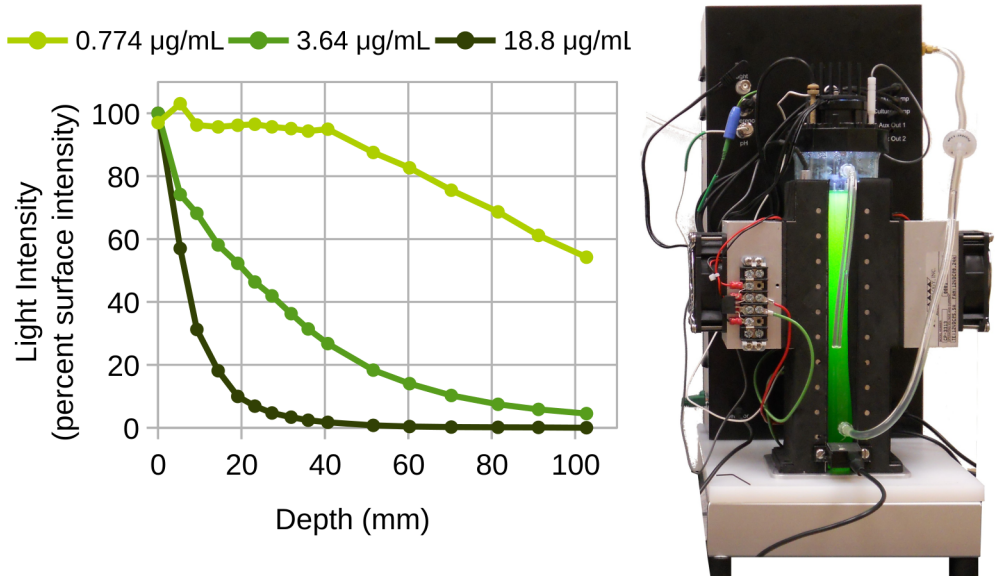

***Figure 25: Measurement of the light gradient in an ePBR culture of* Chlorella sorokiniana.** *The attenuation in light from the growth LED was measuring using an LR1 spectrometer (ASEQ Instruments) attached to a fiber optic inserted through a septum mounted on the bottom of a modified culture vessel (left). The measurements were made with three different densities of cultures: 0.774 µg chlorophyll/mL (light green), 3.64 µg chlorophyll/mL (green), and 18.8 µg chlorophyll/mL (dark green). Light gradients such as these are readily apparent to the human eye when a culture is viewed from the side (right).*

of photosynthesis while the algae near the bottom of the pond are light-limited (Huisman *et al.* 1999) (see Figure 25). The theory is that natural selection favors "weedy" algae that absorb more light than necessary to shade-out the competitors in the water column (Huisman *et al.* 1999). Experiments by Polle et al. (2002) have suggested that it may be possible to increase the per-surface-area productivity of a production pond by truncated light harvesting complex in the algae. This reduces the light absorbed per cell and reduces the severity of the light gradient (as discussed in Perrine et al. 2012). On the other hand, daylight varies throughout the day and the flexibility of the algae to acclimate to these changes may be more important than the absolute efficiency at any particular light environment.

Since our reference "natural environment" for our design is an outdoor production pond, we believe that it is important to incorporate the light gradient into our design. This required us to pay close attention to the geometry of the culture. A "nature-like" light gradient requires a collimated light source and a culture volume whose horizontal cross-section is constant (or nearly so) from top to bottom.

The Day-Night Cycle

Most algae species have circadian rhythms. The circadian clock in *Chlamydomonas reinhardtii*, for example, is known to regulate cell division, maintenance of the photosynthetic protein complexes, and other cellular

processes as well (reviewed in Mittag 1996 and Suzuki & Johnson 2001). Oftentimes, algal researchers regard this circadian regulation as an inconvenience, as it can cause measurements taken at different times of day could yield different results in the same assay. To bypass this, many researchers cultivate their algae under constant light for several days prior to the experiment to desynchronize the individual cell cycles (as discussed in Anderson 2005). However, two problems arise from this practice. First, by desynchronizing the cell cycles, any measurement taken is sampling a mix of different states, and should the algae have different responses to their environment at different stages in their cell cycle (e.g. exhibiting different phototaxis and chemotaxis behaviors at different times of day, as reported in Mittag et al. 2005), then such responses may be diluted out and missed. Secondly, circadian rhythms are notorious for being able to synchronize on even subtle changes in light intensity and may persist for several days even in the absence of any periodic stimulus (Kondo *et al.* 1991), so it is extremely difficult to truly desynchronize an algal culture. Thus comparing one desynchronized culture to another risks accidentally comparing a desynchronized culture to a synchronized one.

For all the inconvenience that the circadian rhythm places on the experimenters, there are advantages as well. Obviously the presence of a day-night cycle is a much closer approximation to a "natural environment" than continuous light. A less obvious benefit is that when the cultures are synchronized (and all assays are performed at

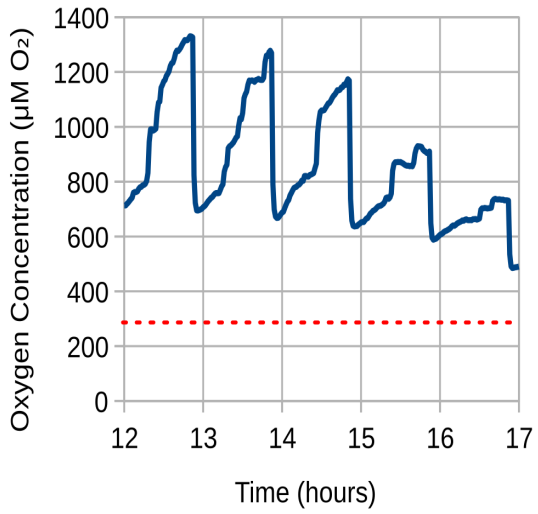

Figure 26: Oxygen concentration logged in an ePBR culture of* Chlamydomonas reinhardtii *over the course of one afternoon. *The culture was sparged hourly with 5% CO_2 enriched air for 1 minute every hour, causing a sudden drop in the culture's oxygen concentration at during sparge event. As the light dimmed from the sinusoidal day-night cycle (peak noon-time intensity of 2000 µmol photons/m^2/s), the rate of oxygen production by photosynthesis declined. The red dashed line indicates what the oxygen concentration would be if the medium were in equilibrium with the atmosphere (20 kPa oxygen partial pressure).*

roughly the same time of day), the algae are more consistent in their behavior, which improves the reproducibility of the experimental data (as discussed in (Lee & Fiehn 2008)). However, using a synchronized cell culture means that the experimenter must interpret the data in the context of the physiological state of the culture at the time of day when you took the sample. Both synchronized and desynchronized culture experiments have their place in a mechanistic study of photosynthesis.

Gas exchange

It is easy to overlook the importance of gas supply and diffusion when culturing micro-organisms, but gas exchange plays a critical role in the photosynthesis and growth of algae. Unless given as a solution of bicarbonate salt, the carbon needed for photoautotrophic growth must enter the culture medium from the gas phase. Furthermore, the O_2 produced by the photosynthesis of the algae tends to accumulate if the culture lacks efficient gas exchange with the air (Pulz 2001) (see Figure 26). Chapter 4 provides a detailed discussion about the consequences of O_2 accumulation in algal cultivation.

THE EPBR

We designed a new photobioreactor platform which came to be known as the environmental simulation photobioreactor (ePBR) (Lucker *et al.* 2014). The ePBR quickly became the primary cultivation platform for all algal experiments in the Kramer Lab and would also be adopted by several other laboratories around the world (for examples, see: Tamburic et al. 2014, Van Wagenen et al. 2015, Jallet et al. 2016, Do Nascimento et al. 2015, and Negi et al. 2016).

A copy of (Lucker *et al.* 2014) has been included in APPENDIX C with permission from the current copyright holder.

Design Goals

To create an algal cultivation platform capable of reproducibly simulating a pond environment on the bench-top, we needed the ePBR to reproduce sunlight intensities and outdoor temperatures and fluctuate these parameters to mimic natural weather. In addition, we needed a system with a geometry that provided a reasonable approximation of a water column in a production pond, and we also needed the ePBR to have a gas exchange system that would let us manipulate the gas environment and deliver CO_2 to the culture. In addition, we needed the ability to interface sensors such as the IDEA spectrophotometer with the algae culture and we needed this platform to be small enough and cheap enough for us to have several ePBRs to conduct parallel experiments.

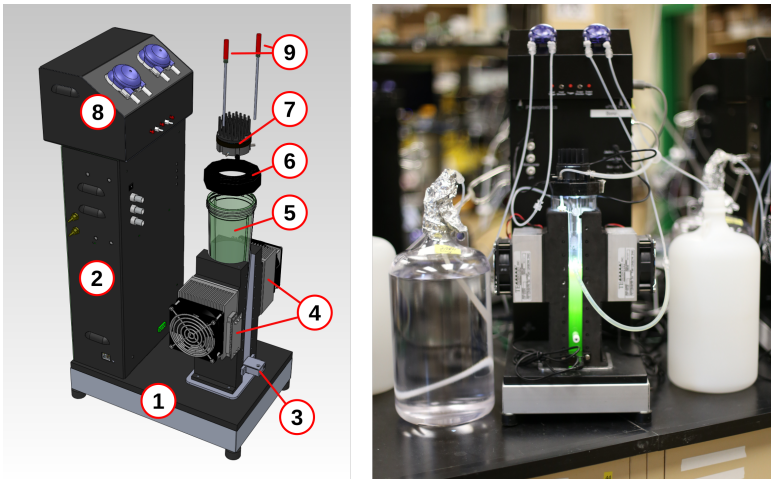

Figure 27: Diagram of ePBR hardware (left) and a photo of a single ePBR turbidostat (right). *The following components are highlighted on the diagram: base plate (1), tower (2), optical density sensor (3), peltier-effect solid state temperature controllers (4), culture vessel (5), culture vessel cap (6), growth light (7), turbidostat pumps (8), pH probe consisting of two half-cells that are inserted into the medium through holes in the culture vessel cap (9).*

Hardware

The hardware of the ePBR (diagrammed in Figure 27) can be divided into 5 components: culture vessel, jacket, growth light, tower, and base. Each was designed to provide a particular feature to the ePBR.

Culture Vessel

The culture vessel was designed to hold a cylinder of algae culture in rough approximation of the water column in an algal production pond. Measuring 30 cm tall, it can hold culture volumes as great as 500 mL, though for most experiments, we settled on using 350 mL volume (15 cm deep) cultures in the ePBRs.

Several practical considerations went into the design of the culture vessel. Most importantly, we chose medical grade transparent polycarbonate as the material for the culture vessel. Polycarbonate is able to withstand heat sterilization in a typical laboratory autoclave, thus allowing the user to sterilize the culture media in a sealed culture vessel and reduce the opportunities for contamination. Another feature of the culture vessel design is that its walls are thickened along two opposing sides. This provides enough depth to drill and tap holes for connections into the culture vessel, such as flow lines for a turbidostat or sparge stone. The cap likewise features dedicated spots for the addition of holes and probes.

Too keep costs down, we opted to turn to injection molding manufacturing for the culture vessel and its cap. One of the limitations of injection molding is that a tall object cannot have perfectly vertical sides or it will not be removable from the mold after the plastic sets. This necessitated that the culture vessel have a slight taper of a few degrees. While that is less than ideal for modeling the culture as a simple water column cylinder, the tapered sides allow the culture vessel to rest in the temperature control jacket like a fast-food cup in a cup-holder. This simplifies the assembly and maintenance of the ePBR.

Jacket

The aluminum jacket serves two purposes. First, it holds up the culture vessel and keeps it firmly in place. A vertical gap between the two halves of the jacket provides space for the connectors on the side of the culture vessel and visual access to the culture. Sensors, such as the optical density sensors, can be mounted to this gap via a series of screw holes along each edge. The second function of the jacket is to provide temperature control for the culture. It achieves this using a pair of peltier-effect solid-state heating/cooling elements and a pair of temperature sensors. One sensor monitors the temperature of the jacket and the other is inserted through the cap into the culture medium. Using an algorithm that I developed after much trial-and-error, the ePBR is able to control the temperature of the jacket to quickly change the culture temperature to meet the target temperature without a substantial overshoot, even if the target is rapidly changing, as is often the case in weather simulations (Figure 28).

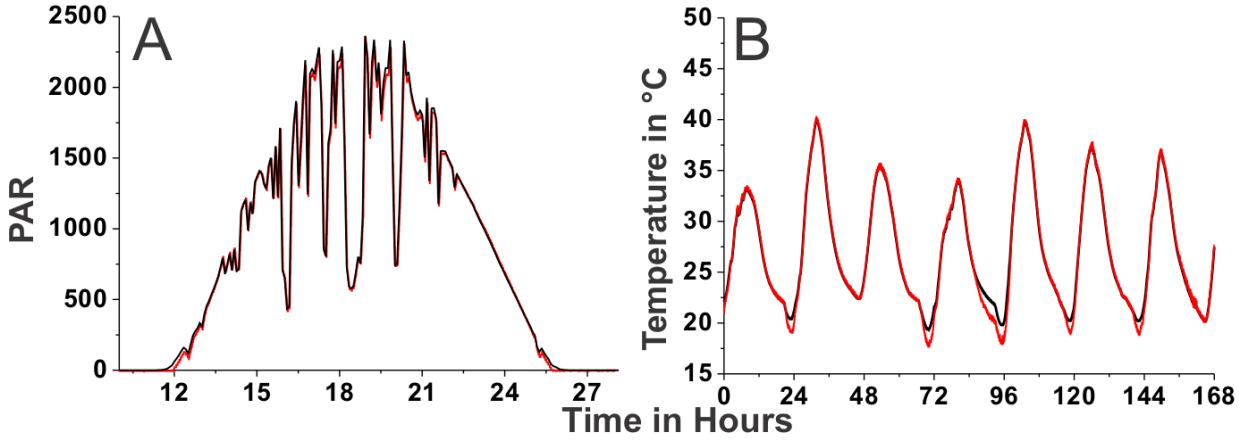

Figure 28: Accuracy test of light and temperature control in the ePBR. *Expected value is traced in black while the actual value that the ePBR was able to accomplish is in red. The light intensity control (panel A) is very accurate up to 2200 µmol photons photosynthetically active radiaion/m^2/s (PAR), though the accuracy suffers at very low light intensities. The ePBR was also able to track a dynamic temperature target, with undershoots of approximately 1°C when the intended temperature dipped rapidly below room temperature (panel B). This figure is a reproduction of Figure 5 from Lucker, B. F., Hall, C. C., Zegarac, R., & Kramer, D. M. (2014), Algal Research, 6, Part B, 242–249. Permission to use this figure in this work was kindly granted by the present copyright holder (RightsLink license #4060000845495).*

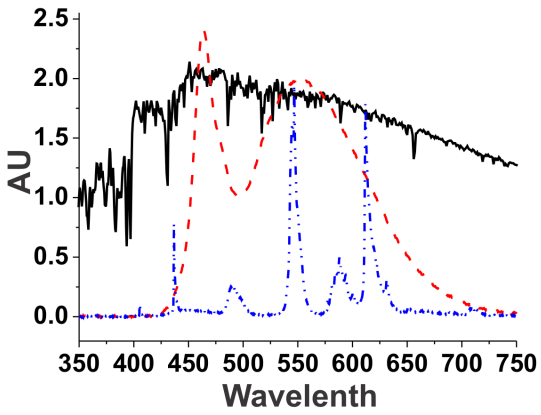

Figure 29: Comparison of light source spectra. *Shown here are the spectra for sunlight (black, solid), fluorescent lamps (blue, dotted), and the ePBR growth light (red, dashed). This figure is a reproduction of Figure 2A from Lucker, B. F., Hall, C. C., Zegarac, R., & Kramer, D. M. (2014), Algal Research, 6, Part B, 242–249. Permission to use this figure in this work was kindly granted by the present copyright holder (RightsLink license #4060000845495).*

Growth Light

The growth light consists of a high-power white LED, which offers several advantages over fluorescent and incandescent lighting. The most important practical feature of the LED is that its light intensity can easily be controlled by current-regulating circuitry. LEDs are also very bright, and our LED growth light can achieve light intensities equivalent to full sunlight. In comparison, fluorescence lamps are generally not dimmable and are not very bright, while an incandescent light of equivalent light intensity as our high-power LED would generate so much heat that active cooling would be required just to keep the culture from overheating. Another important feature of the white LED is that it is a closer approximation to the solar spectrum than a fluorescent lamp, though our LED light source is still weak in the green region of the light spectrum and lacks UV and far-red components (Figure 29). Perhaps a future LED product will offer a spectrum closer to natural sunlight.

The final feature to note about the ePBR growth light is that it has a collimating optic to collimate the light. As discussed previously in this chapter, a collimated light source is vital to reproducing a realistic light gradient in the culture, especially when dealing with a relatively small volume such as our culture vessel.

Tower

The tower houses the three circuit boards that control the ePBR and the power supply unit. One circuit board controls the growth light, another reads the sensors, and the third hosts the microcontroller and all of the peripherals that it needs to communicate with the local area network and with the other circuit boards.

Base

The base of the ePBR has three functions. First, it is a mechanically stable foundation that supports the weight and structure of each ePBR. Second, the base features a carved out impression matching the footprint of the jacket, thus holding the jacket firmly in place without the need of additional screws or other mounting components. Finally, the base houses the magnetic stirring motor used to stir the culture via a stir-bar. The speed of the stirring motor can be precisely controlled and we've found that stirring speeds in excess of 100 revolutions per minute (RPM) prevented the formation of a gradient of photosynthetic efficiency phenotypes, indicating that this mixing speed was sufficiently fast to homogenize the behavior of the whole culture (whether or not that's desirable depends on the research question).

Software

What makes the ePBR truly useful is the amount of automation that is built into this cultivation platform, and that automation comes from the software which runs the ePBRs. At the lowest level, there is software embedded into the microcontroller of the ePBR hardware to operate the ePBR. This software component is called the firmware. The higher-level program which offers a graphical user interface is the control program known as AlgalCommand. AlgalCommand runs on a standard desktop computer of any operating system.

Firmware

From the perspective of the microcontroller, sensors operation means setting digital output signals on command and then reading back the voltage of the sensor's electronic circuit. The simplest of these sensors is the optical density sensor. Mechanically, this consists of a paired infrared LED emitter and a detector located on the jacket such that the infrared pulses must pass through the culture to reach the detector. As the culture density increases, more of the light is scattered and thus less light reaches the detector. However, since there is a stir-bar in the bottom of the culture vessel, a raw measurement optical density sensor could be biased by the orientation of the stir-bar at that instant. To overcome this, the ePBR takes periodic measurements and reports the rolling average of the previous 10 minutes of sensor readings.

The temperature sensors pose a different challenge. There can be a significant temperature gradient within the aluminum block of the jacket while the peltier elements are running, making precise temperature control more difficult. The solution was to unpower the peltier elements for 10 seconds prior to measuring the jacket temperature, giving enough time for the temperature gradient to equalize and thereby get an accurate measure of the jacket

temperature, enabling accurate control of the culture temperature.

By far, the most difficult sensor to control on the ePBR is the pH sensor. pH probes work by measuring the electrical voltage potential across the pH probe's glass membrane relative to a silver chloride reference electrode (as explained in Hughes 1928 and Mirsky & Anson 1929). The problem is two-fold. First, since the probe relies on ion exchange with the thin glass bulb on the end of the probe, it is easily impaired by algae or other microbes sticking to the surface of the bulb and coating it with proteins and other macro-molecules (discussed in Munro et al. 1996). Cleaning the probes requires removing them from the ePBR and then re-inserting them, which risks contaminating the culture with foreign microbes. The second problem is that there are only so many ions in the reference electrode for exchange and they slowly diffuse out while the electrode is immersed in the medium. The electrolyte solution in the pH electrode can likewise change over time. In most pH probe applications, the pH probe and reference electrode are stored in the electrolyte solution to replenish these ions while the probe is at rest. The probe typically spends very little time immersed in the hypotonic sample solutions. For the ePBRs, however, we need the pH probe to operate continuously in constant immersion in the algae culture medium for weeks at a time. As the ions are depleted, the calibration of the pH probe can drift (or the probe may stop working completely) and re-calibrating the probe again requires the removal and re-insertion of the probes, another contamination hazard. These problems cannot be solved by the firmware or electronics of the ePBR, but the addition of calibration protocols to the firmware does at least make it possible to run week-long experiments with pH probes, if desired.

Besides operating the hardware, the other job of the firmware is to communicate with the host computer (which is running the AlgalCommand control program) over the ethernet local area network (LAN). The ePBRs use standard ethernet networking hardware for communication as it is not only inexpensive, but also durable and extremely reliable with built-in fault detection and correction. Using an all-in-one ethernet controller purchased from Lantronix Inc., each ePBR hosts a network socket to receive text-based commands from AlgalCommand and respond in kind.

The source code for the ePBR firmware can be found in Supplemental Files 4.

AlgalCommand

AlgalCommand is a software program which runs on a desktop computer connected to any number of ePBRs by a LAN. A network consisting of one AlgalCommand computer and multiple ePBRs is referred to as a matrix and is the basic organizational unit of the ePBR platform. Each ePBR in the matrix can be independently

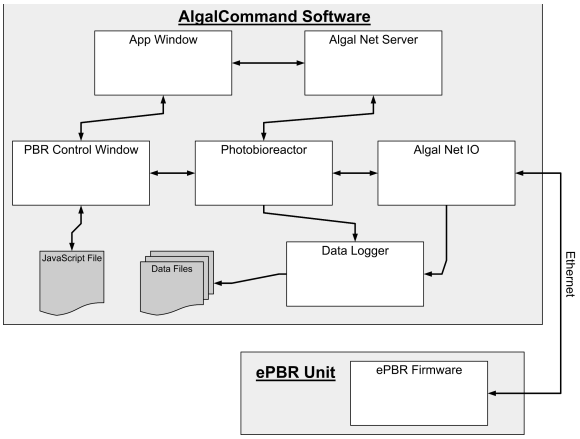

Figure 30: Diagram of the AlgalCommand software and its component modules. *Arrows indicate the flow of data between the different modules. The main module which handles the graphical user interface (GUI) is the App Window, which hosts a PBR Control Window for each ePBR unit that is detected on the ethernet local area network. The PBR Control Window manages both manual and script controls by passing the appropriate commands to the Photobioreactor module. Communication with the network is mediated by the Algal Net IO module, which sends and receives commands from the ePBR Firmware. The Algal Net Server manages the discovery and connectivity of the Photobioreactor modules. The Data Logger listens to the communications between the Algal Net IO and Photobioreactor modules to record all data events in the data log files.*

controlled and the AlgalCommand software provides graphical user interfaces for the sensors and environment controls. The interaction between all of the software components is depicted in Figure 30.

The environmental controls are light, temperature, stirring, and gas sparging. In the light controls, the day-length can be specified and the type of day can be either square-wave or sinusoidal (see APPENDIX D for a detailed description of the sinusoidal day-night algorithm). In either case, the day is centered on noon according to the computer's system clock. Under temperature controls, the ePBR can be set to static temperature or daily sinusoidal

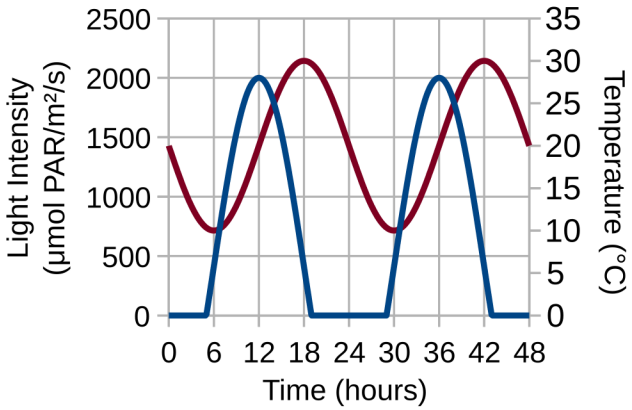

Figure 31: Light and temperature regime using the preset sinusoidal day-night and temperature cycles. *The light intensity was set to a 14:10 sinusoidal day:night cycle with a peak growth light intensity of 2000 µmol photons PAR/m²/s (blue). The temperature was set to 20°C with a daily temperature fluctuation of ±10°C (red).*

fluctuations (more complex temperature fluctuations are possible with the scripting feature described later in this chapter). An example of the sinusoidal light and temperature control is shown in Figure 31.

The stir-bar control consists of a simple speed selector.

The gas sparging controls received special attention in the design of AlgalCommand. As described in the previous section, the ePBR strives to imitate an algal production pond environment. In the outdoor production pond, gas injection happens at a single point in a circulating system, so from the perspective from the algae, the gas injection occurs periodically. Thus it would seem intuitive to simply toggle the gas valves on each ePBR every few minutes to replicate this behavior. However, gas mass flow controllers are very expensive and it is often the case that all of the ePBRs in a matrix would be connected to a single gas source. Thus if more than one ePBR sparges simultaneously from the same gas source, then all of the ePBRs would need their own individual flow controllers and the regulator on the gas source would need to support a flow rate high enough to simultaneously serve all ePBRs. Instead, AlgalCommand uses a time-sharing algorithm to coordinate the sparging of the ePBRs, ensuring that no two ePBRs sparge from the same gas source at the same time. This feature has greatly simplified the gas line plumbing for our ePBR matrices as well as reduced the cost of installing the gas infrastructure.

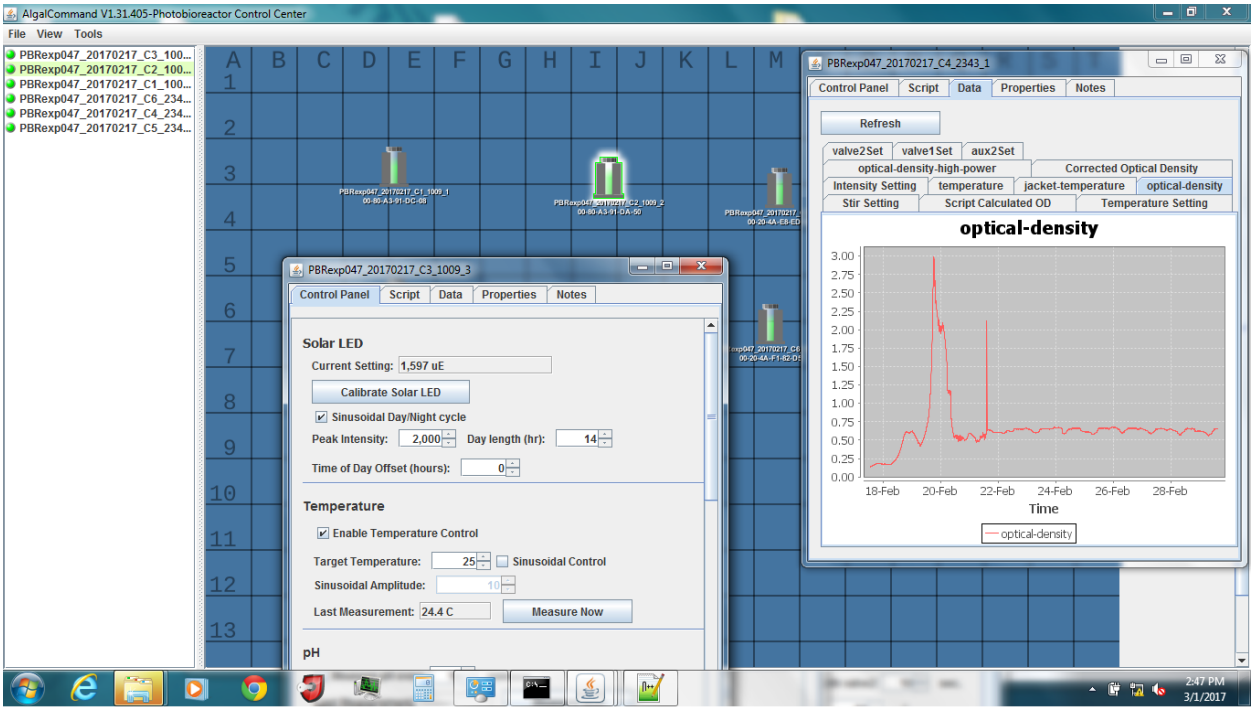

Figure 32: Screenshot from a computer running six ePBRs via AlgalCommand.

The sensor controls for the ePBRs include pH and optical density. For the pH sensors, AlgalCommand includes a calibration tool and a selector for the measurement frequency. More advanced uses of the pH probe (such as a pH-stat) require a script (see *script control* in the next section). The optical density sensor controls likewise allow the user to specify a measurement frequency, but the interface also includes options for running a sensor driven turbidostat. When turbidostat control is enabled, every time the optical density sensor reading exceeds the target threshold, the ePBR triggers a dose of dilution from the attached pumps to pump in a fixed volume of sterile medium (more on turbidostat operation later in this chapter). Note that the readings from the optical density sensors

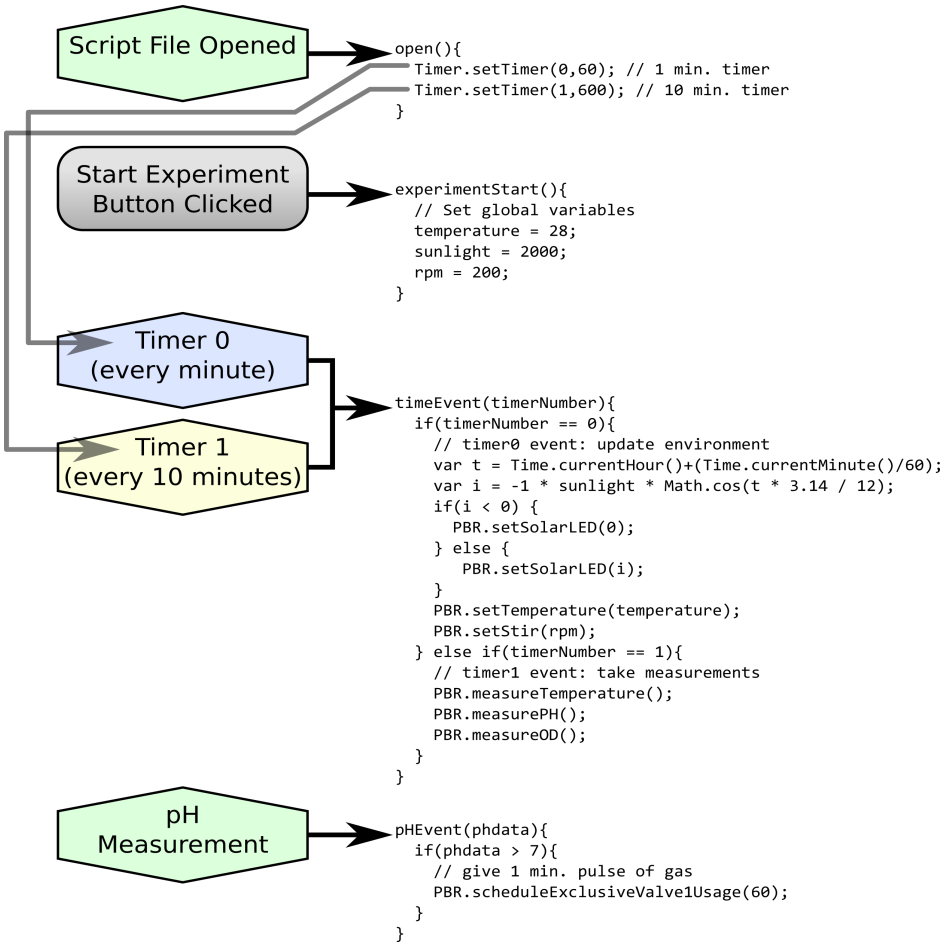

Figure 33: Diagram of an event-based script. *This particular example is a simple pH-stat script which implements constant stirring and temperature (200 RPM and 28°C respectively) and a 12:12 sinusoidal day-night cycle with a peak light intensity of 2000 µmol photons PAR/m^2/s. When the script file is opened, the* open() *function is called, which tells AlgalCommand to initialize two repeating timers numbered 0 and 1, such that timer 0 repeats every minute and timer 1 repeats every 10 minutes. When the "Start Experiment" button in the scripting GUI is clicked, the* experimentStart() *function is called, which sets the variables used for adjusting environmental parameters. Every time one of the two timers repeats, the* timeEvent(x) *function is called with the number of the timer passes as the parameter. The code inside the* timeEvent(x) *function updates the environmental paramters when the timer that triggered the event is timer 0 and initiates temperature, optical density, and pH measurements when the timer is timer 1. After the ePBR measures its pH, the* pHEvent(x) *function is called with the measured pH passes as its function parameter. In this example, the function tells AlgalCommand to schedule a 60 second sparge of gas through valve 1 if the pH is greater than 7.*

are a relative measure of optical density that should be used in conjunction with chlorophyll concentration or other direct measure of the culture density.

The source code for the AlgalCommand software can be found in Supplemental Files 5 and a screenshot from the software is presented in Figure 32.

Script Control

For simple growth experiments, the predefined environmental controls presented in the AlgalCommand GUI are sufficient, but more complex experiments are also possible using the scripting interface of AlgalCommand. Script files are written in the JavaScript programming language and unlike a traditional scripting system, the script is event-based rather than procedure. What this means is that instead of simply executing the script from top to bottom in the order as written, AlgalCommand calls functions from the script in response to events related to the ePBR. The advantage of such an event based scripting system is that it is now possible for the script to make decisions based on real-time data. For example, whenever an ePBR under script control takes a pH measurement, the *pHEvent(…)* function is called from the script with the just-measured pH value passed as the function parameter. That function could then test the pH value and decide whether to inject additional CO_2 into the ePBR (more on pH-stating later in this chapter).

APPENDIX E contains a copy of the official scripting documentation included with the AlgalCommand software distribution package.

MODES OF OPERATION

Batch Cultures

The simplest way to operate an ePBR is batch culture growth. In batch culture experiments, all ePBRs are inoculated with identical cell densities and then cultivated without the addition of new medium. The advantage of batch culture growth is its simplicity. If the goal is simply to grow a batch of algae for a single day of sampling or assays, then a batch culture my be acceptable. However, there are many drawbacks to batch culture growth. In a batch culture, each day is a different environment for the algae as their (often rapid) growth reduces the penetration of light into the culture and the nutrients in the medium are consumed. This makes it impossible to compare cultures of different ages (even if the age difference is only a few hours). The other problem is that the growth curve of a batch culture is very sensitive to the inoculation density and therefore any error in the cell count of the inoculum would be detrimental to the reproducibility of batch culture experiments.

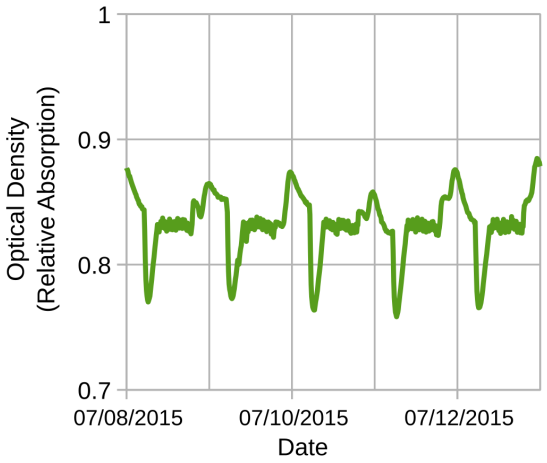

Figure 34: Optical density (OD) signal over the course of 5 consecutive days of an ePBR turbidostat. *This particular turbidostat houses a culture of* Chlamydomonas reinhardtii *strain NAP10 in high salt minimal medium, sparged hourly with 5% CO_2-enriched air, with turbidostat dilution during daylight hours only. The turbidostat target was set to maintain the culture at 5 µg chlorophyll/mL culture density. Note that the OD goes up for a few hours after the growth light turns off, indicating that the* C. reinhardtii *cells stored enough carbon during the day to grow after dark, and their OD dips rapidly upon first light in the morning. The cause of this morning dip is unknown.*

Turbidostating

Operating the ePBRs as turbidostats requires a significant amount of investment in hardware and methods, but the investment is usually well worth it. In a turbidostat, the Aux2 output of the ePBR is connected to a pumping system that can be triggered by a pulse of voltage on the Aux2 line. When triggered, the pump adds a predetermined volume of sterile medium to dilute the culture, and then withdraws from the overflow port to bring the culture volume back to the pre-dilution level. Such a setup requires pumps, carboys of sterile medium, waste collection, and lots of tubing to connect it together, as well as the development of lab-specific protocols for sterilization and operation. For all this effort, there are many benefits. First, since the turbidostat is returning the culture to the same culture density each day, the algae within the ePBR experience the same environment day after day. This allows the experimenter to perform different experiments or technical replicates of the same ePBR culture across multiple days and still have comparable results. This also prolongs the useful life of an algal culture from a single day (in batch culture operation) to several weeks. Sampling from the ePBR is also made more convenient in turbidostat operation because the experimenter can easily gather a fresh sample of culture from the overflow port. Another very important aspect of the turbidostat ePBR is the information gained by recording the number of pump dilutions triggered each day. From this information, one can calculate the volume diluted per day, and from that, measure the growth rate of the algae, with consecutive days under turbidostat operation providing technical replicates of the growth rate

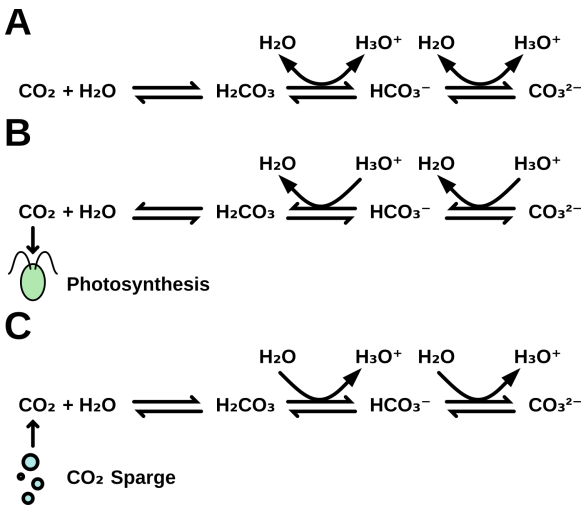

Figure 35: Chemistry of a pH-stat. *In water, inorganic carbon is in equilibrium between carbon dioxide, carbonic acid, bicarbonate, and carbonate (panel A). When algae perform photosynthesis, they consume the carbon dioxide in the medium, shifting the equilibrium in such a way as to reduce the concentration of H_3O^+, increasing the pH of the medium (panel B). When the pH rises, a pH-stat sparges the medium with carbon dioxide, which shifts the equilibrium the other way and reduces the pH (panel C).*

measurement. Figure 34 shows sample optical density data from a day-time dilution turbidostat.

pH-stating

In pH-stat operation, the ePBR counteracts the increase in culture medium pH due to photosynthesis by acidification with CO_2. Assuming that the culture medium does not contain a high concentration of buffering chemicals (such as phosphate or Tris), the rate of CO_2 injection equals the rate of net photosynthesis for the culture (see Figure 35 and Figure 36).

In practice, however, there are a number of caveats and limitations to the operation of a pH-stat. The first caveat is that the buffering capacity of the culture medium needs to be relatively low, otherwise the depletion of Ci from the medium may not cause a sufficient change in the pH to reliably control the delivery of CO_2. The second caveat, which has proven to be critical to the success or failure of a pH-stat, is that some of the macronutrients consumed by the algae will also affect the pH of the medium. The nitrogen source in the medium is particularly influential in this regard. In the case of nitrate, the consumption of this weak acid raises the pH, which the pH-stat system will misinterpret as CO_2 consumption, resulting in an over-delivery of CO_2. Ammonia, on the other hand, is even more disruptive to a pH-stating system, as the consumption of this weak base lowers the pH. At a certain point, a culture may consume enough ammonia that the pH will never hit the pH-stat target, even when the medium is completely depleted of Ci. To avoid these problems, one can use urea as the sole nitrogen source for their cultures

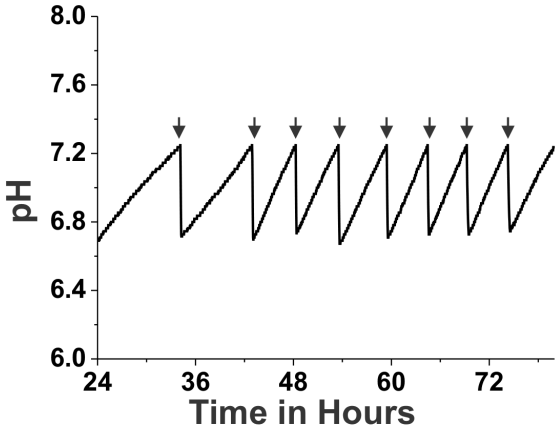

Figure 36: pH over time in an ePBR pH-stat culture of* Chlorella sorokiniana *under constant illumination. *Arrows indicate the initiation of sparging with 5% CO_2-enriched air. This particular pH-stat was programmed to keep the pH between 7.2 and 6.8. This figure is a reproduction of Figure 4B from Lucker, B. F., Hall, C. C., Zegarac, R., & Kramer, D. M. (2014), Algal Research, 6, Part B, 242–249. Permission to use this figure in this work was kindly granted by the present copyright holder (RightsLink license #4060000845495).*

(Soletto *et al*. 2005), although many algae appear to be far less efficient at assimilating nitrogen from urea than from ammonia or nitrate (Healey 1977).

REPLAYING NATURAL ENVIRONMENTS

Much of the design of the ePBR centered on approximating the dynamic environment of an outdoor algae production pond, without yet knowing how important these dynamic environmental fluctuations were to the photoautotrophic growth of the algae. This question simply could not be answered without a tool like the ePBR, and it was one of the first that we addressed after the completion of the ePBRs.

Altus OK, July 2005, and the growth of C. reinhardtii

To test the capabilities of the ePBR, and to determine the importance of natural light and temperature fluctuations on the growth of *Chlamydomonas reinhardtii*, we created a simulation of the environment of a hypothetical algae pond located in Altus, Oklahoma, throughout the month of July in the year 2005. The choice of Altus was completely arbitrary, as was the month and year, though we chose a city in the state of Oklahoma because of the excellent quality of Oklahoma's weather data archives available from the Mesonet website (Mesonet; McPherson *et al.* 2007). For accurate simulation of the water temperature, we passed the relevant weather data to Drs. Quentin Bèchet and Benoit Guieysse of Massey University and they kindly applied their pond simulation model (Béchet *et al.* 2011) to generate the expected water temperature of our hypothetical pond. The combined light and temperature simulation data was then used to program the ePBRs to replay the weather for our hypothetical algae

production pond (Figure 37).

We also created a static environment for growth rate comparison. This static environment featured a constant temperature equal to the integrated average temperature for the weather simulation. The day-night cycles were set to have the same average day-length as the weather simulation with a constant light intensity that provided the same integrated flux of photosynthetically active radiation (PAR) as the weather simulation over the course of the whole simulation. All other parameters (such as gas sparging) were identical between the two environmental programs.

Batch cultures of *Chlamydomonas reinhardtii* demonstrated remarkably similar growth rates between the weather simulation and its static counterpart. The first 5 days of the growth curves were nearly identical despite severe light fluctuations on days 1 and 4 of the weather simulation (partly-cloudy days). After 5 days, however, the weather fluctuations appeared to slow down the growth of *C. reinhardtii* relative to its performance in the static environment, though the weather simulation cultures did eventually reach the same maximum culture density as the static environment. We did not investigate the specific mechanisms responsible for slowing down the growth of a

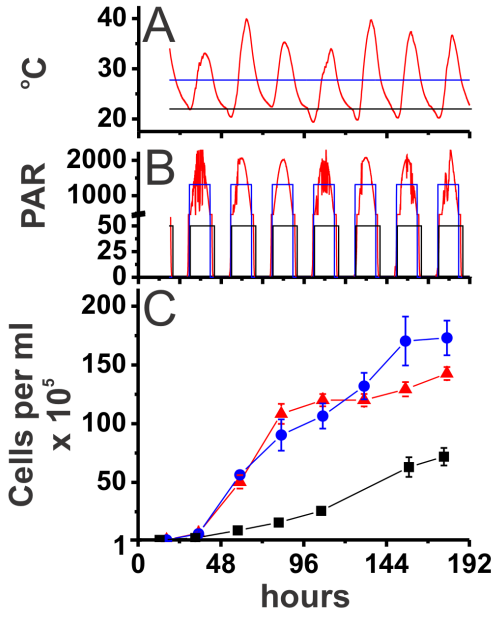

Figure 37: Batch culture growth in weather simulating ePBRs compared to static culture conditions. *Cultures of* Chlamydomonas reinhardtii *strain CC-125 were cultivated in ePBRs simulating the weather in Altus, Oklahoma in the month of July 2005 (red), ePBRs simulating a static environment (blue), and bubble flasks (black). The weather simulation featured daily temperature fluctuations between 10°C and 20°C (panel A) and light fluctuations that could halve or double the light intensity in less than 5 minutes (panel B). The culture growth was measured by the cell densities of the cultures, measured once daily (panel C). This figure is a reproduction of Figure 6 from Lucker, B. F., Hall, C. C., Zegarac, R., & Kramer, D. M. (2014), Algal Research, 6, Part B, 242–249. Permission to use this figure in this work was kindly granted by the present copyright holder (RightsLink license #4060000845495).*

dense batch culture of *C. reinhardtii* during weather fluctuations, but this experiment demonstrated a couple of points that informed our future experiments.

First, the Altus, Oklahoma weather simulation showed that the common *C. reinhardtii* lab strain CC-125 of is more robust than it is often given credit for, at least when it is grown in the ePBR. When cultured in a bubble flask under fluorescence lamps, *C. reinhardtii* is known to be sensitive to bright light (as demonstrated in Fischer *et al.* 2006). This has given *C. reinhardtii* a reputation for being a low-light adapted alga, which would be consistent with the ecological context of *C. reinhardtii* being a soil algae (reviewed in Fernández *et al.* 2009). The robust high-light tolerance of ePBR cultivated *C. reinhardtii* may be the product of two major differences between ePBR and flask culturing platforms. The first is that the geometry of the ePBR causes a significant light gradient, so the individual *C. reinhardtii* cells in the ePBR experience the full illumination only briefly before plunging back down as the culture is mixed. The second major difference is that ePBR experiments are multi-day experiments and the *C. reinhardtii* culture has time to acclimate to the ePBR environment. The result is that *C. reinhardtii* ePBR cultures are acclimated to a high-light environment and are apparently quite tolerant of light fluctuations in this state.

The second take-away from the Altus weather simulation experiments is the significant limitations of using batch growth experiments to study growth in a dynamic environment. In the above experiment, it is impossible to say which days in the weather simulation were most challenging to the *C. reinhardtii* culture as each day started with a different culture density. It is also unclear whether nutrient limitation became a factor at any point during the growth curve. In short, using batch cultures for dynamic environmental studies introduces too many uncontrolled variables on top of an already complex experiment.

USING ARTIFICIAL ENVIRONMENTS TO STUDY PARTICULAR PHENOTYPES

Another way of using the ePBR platform is to create an artificial environment to study the function of a particular phenotype. In this case, the created environment is designed to exaggerate a particular challenge that an alga might face, causing a process that would otherwise have very subtle effects to now be readily apparent. One example of this approach is a study conducted by Dr. Marco Agostoni and co-authors to examine the fitness cost of modifying the phycobilisomes for improved growth in the cyanobacterium *Fremyella diplosiphon* (Agostoni *et al.* 2016). Interestingly, they found that the phycobilisome-less *F. diplosiphon* mutant strain FdCh1 was able to compete with the wild-type in ePBRs with a rapidly fluctuating light intensity (light toggled on/off every minute), where-as a light regime that did not have such fluctuations resulted in the wild-type strain quickly out-competing the mutant

strain (Agostoni *et al.* 2016).

FUTURE DEVELOPMENT

The ePBR is already a successful photobioreactor platform that is being used around the world my many university and corporate laboratories. However, there is one feature from the earliest drawing board that has not yet been implemented: integrated fluorometry and spectrophotometry measurements. With such measurements, we could have real-time analysis of the level of photosynthetic stress experienced by the culture during environmental fluctuations.

CHAPTER 4: HYPEROXIA SENSITIVITY IN CHLAMYDOMONAS REINHARDTII CORRELATED WITH WATER-WATER CYCLE ACTIVITY

Christopher C. Hall[12], Ben F. Lucker[13], and David M. Kramer[13]

ABSTRACT

The inhibition of photosynthesis by hyperoxia poses a significant challenge to the photosynthetic productivity of algae in photobioreactors and production ponds. While oxidative photodamage, photorespiration, and the water-water cycle have all been suggested as possible explanations for hyperoxia inhibition of photosynthesis, no previous work has attempted to identify which of these mechanisms differentiates hyperoxia tolerant algae from hyperoxia sensitive algae. To address this, we identified two *C. reinhardtii* strains with differential hyperoxia sensitivity. Strain CC-1009 had a faster growth rate than strain CC-2343 in CO_2-enriched hyperoxia photobioreactors. To identify the mechanism of this hyperoxia growth inhibition, we compared their photosynthetic efficiencies and glycolate production rates under multiple oxygen environments. The strains were found to differ primarily in their rates of O_2 consumption during photosynthesis, with CC-2343 strain exhibiting substantially more oxygen consumption than CC-1009. Glycolate production rates could not account for the observed amounts of O_2 consumption, indicating that the water-water cycle is the primary limitation to hyperoxia photosynthesis. In low-CO_2 photobioreactors, strain CC-2343 outperformed strain CC-1009, suggesting an evolutionary or mechanistic trade-off between adaptation to hyperoxia versus low-CO_2 environments.

INTRODUCTION

Earth's atmosphere is approximately 21% oxygen with very little variation between different locales (L. Machta 1970). This contrasts with aquatic systems, where the slower rate of gas diffusion, together with biotic production and consumption of O_2, leads to steep gradients in oxygen tension and the formation of distinct hypoxic and hyperoxic zones (such as in the cases reported by Truchot & Duhamel-Jouve 1980 and Irwin & Davenport 2002). Here, we focus on the impact of the very high oxygen tensions that often accompany oxygenic photosynthesis in aquatic environments and poses a substantial limitation for algal biofuel/bioproduct production.

In a natural setting, oxygen accumulates to hyperoxia when the density of algae and availability of dissolved inorganic carbon results in a photosynthetic rate that exceeds the rate of gas exchange with the

1 MSU-DOE Plant Research Lab, Michigan State University, East Lansing, MI 48824-1312, US

2 Plant Biology, Michigan State University, East Lansing, MI 48824-1312, US

3 Biochemistry and Molecular Biology, Michigan State University, East Lansing, MI 48824-1312, US

atmosphere. Tide pools, for example, exhibit daily cycles of hyperoxia and hypoxia in the absence of aeration by breaking wave (Truchot & Duhamel-Jouve 1980). Artificial algae production systems, such as ponds and photobioreactors, are particularly prone to hyperoxia because the operators cultivate the algae to relatively high densities and add additional nutrients (e.g. CO_2 and nitrogen fertilizer) to maximize photoautotrophic growth (reviewed in Peng et al. 2013).

Published surveys on hyperoxia growth in algae demonstrate differences across species in tolerance to hyperoxia. For example, McMinn et al. (2005) found that certain Antarctic algal species were more sensitive to hyperoxia, with inhibitory effects of 86% O_2 ranging from 32% to 68% decreases in relative growth rates. In another study, Beudeker & Tabita (1983) characterized a mutant strain of *Chlorella sorokiniana* whose 99% O_2 hyperoxia growth rate was 50%-100% faster than its parental strain, demonstrating variability in hyperoxia sensitivity between different lineages within the same species.

Three mechanisms have been proposed to explain the inhibition of photosynthetic growth by hyperoxia in algal cultivation: photorespiration, water-water cycle, and oxidative photodamage (for example, in Kliphuis et al. 2011, Suetlemeyer et al. 1993, and McMinn et al. 2005 respectively). In the photorespiration model of hyperoxia inhibition, the ribulose-1,5-bisphosphate carboxylase/oxygenase enzyme (rubisco) incorporates O_2 in the place of CO_2, resulting in the production of 2-phosphoglycolate. Recycling (or excreting) this byproduct equates to a loss of fixed carbon from the cell (reviewed in Badger et al. 2000). Many algae species, including *Chlamydomonas reinhardtii*, possess a carbon concentrating mechanism (CCM) which is reported to effectively prevent the occurrence of photorespiration under limiting CO_2 concentrations (reviewed in (Giordano *et al.* 2005)). Raven et al. (1994) have proposed that high CO_2 environments increase the flux of photorespiration in algae due to the lack of CCM expression.

In the water-water cycle, hyperoxia is proposed to increase the flux of pathways which convert oxygen to water. Such pathways include the plastid terminal oxidase, the formation of superoxide from Photosystem I (Mehler reaction), and the flavodiiron proteins (reviewed in Peltier & Cournac 2002, Asada 1999, and Allahverdiyeva et al. 2014, respectively). All of these reduce the flux of reducing potential available to the Calvin-Benson cycle and therefore an increase in the water-water cycle could reduce the rate of carbon assimilation.

Oxidative photodamage to Photosystem II is known to depend on the formation of singlet oxygen (reviewed in Krieger-Liszkay 2005). In the absence of oxygen, the D1 subunit of Photosystem II does not appear to

suffer damage under photoinhibitory light intensities (Hundal *et al.* 1990). Extrapolating in the other direction, McMinn et al. (2005) have suggested that an elevated O_2 environment can cause enough oxidative damage to decrease the alga's efficiency of light capture.

When one or more of the aforementioned processes inhibits photosynthesis, the contribution of each process can be determined by their different effects on net O_2 production, glycolate metabolism, and chloroplast linear electron flux (LEF). Both photorespiration and the water-water cycle consume oxygen in proportion to their activity, reducing the net photosynthetic oxygen production relative to LEF. Oxidative photodamage, meanwhile, only decreases LEF without significantly impacting the ratio of net O_2 production per LEF. Additionally, decreasing the O_2 in the extracellular environment should immediately reduce the activities of photorespiration and the water-water cycle (Satagopan & Spreitzer 2008; Roberty *et al.* 2014) but oxidative photodamage would persist until repaired by the Photosystem II repair cycle (reviewed in Aro et al. 1993). When a decrease in the production of O_2 per LEF is observed, the apparent O_2 consumption can be assigned to either photorespiration or the water-water cycle based on the amount of glycolate that is produced.

While all of these processes have been demonstrated to occur in the presence of oxygen during photosynthesis, none of them have been tested under hyperoxia. Prior works do not provide a clear answer as to which of these mechanisms are the primary limitation to photoautotrophic growth in hyperoxia. Nor is it known whether the difference in hyperoxia tolerance in different algae is due to differential regulation or activity of these processes.

In this study, we address these open questions by comparing growth and photosynthetic efficiency of hyperoxia tolerant and resistant strains of *C. reinhardtii* after cultivation in normoxic and hyperoxic photobioreactors.

METHODS AND MATERIALS

Strains

The NAP10 strain of *C. reinhardtii* was kindly provided by Professor Ivan Baxter of the Donald Danforth Plant Science Center. This strain was created by crossing *C. reinhardtii* strains CC-125 and GR, selecting for growth on nitrate as nitrogen source, and then back-crossed with the CC-125 parental strain for 9 generations. All other strains of *C. reinhardtii* were ordered from the Chlamy Culture Collection (www.chlamycollection.org).

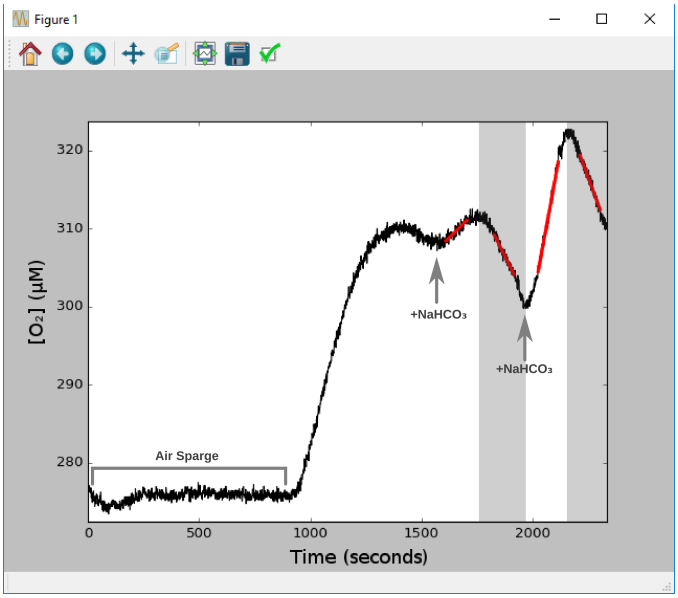

Figure 38: Example oxygen production assay experiment. *After inserting the oxygen probe into the cuvette sample of algal culture and setting the light, the sample was sparged with air for 15 minutes. After the air sparge the sample was allowed to consume the remaining available inorganic carbon by its own photosynthesis until the culture ceased to produce oxygen. Then the light was set to a saturating light intensity and sodium bicarbonate was added to the cuvette (arrows) with dark intervals in between to measure respiration (shaded boxes). The portions of the oxygen trace used to computer oxygen production are highlighted in red.*

Culturing Conditions and Productivity Measurement

Flask cultures of *C. reinhardtii* (same flask culturing conditions as described in Lucker et al. 2014) were inoculated into ePBR turbidostats filled with Sueoka's high salt (HS) medium (Sueoka 1960) and set to a target optical density threshold equivalent to 4 (+/-1) µg chlorophyll/mL with the optical density polled every 10 minutes. The day-night cycle was set to 14 hours of sinusoidal light per day with a peak noon light intensity of 2000 µmol photons photosynthetically active radiation (PAR)/m^2/s. The stir-bar was set to a constant 200 revolutions per minute and the temperature was left uncontrolled (room temperature). Gas from a premixed gas cylinder was delivered to each ePBR for 1 minute every hour at a flow rate of 0.35 L/minute through sintered glass sparge stones suspended inside the culture vessel. The gas cylinders contained either 5%CO_2:20% O_2:75%N_2 (normoxia) or 5%CO_2:95% O_2 (hyperoxia) gas mixtures. Air-sparged ePBRs received 1 minute of filtered compressed air every hour, but were otherwise identical to the normoxia and hyperoxia ePBRs.

When the turbidostat culture reached the target culture density, daily measurements of ash-free dry weight (AFDW) were taken using protocols described in (Lucker *et al.* 2014) and the photosynthetic productivity of the culture was calculated as the AFDW biomass density of the culture multiplied by the volume of culture diluted per

day and normalized to the surface area of the top of the culture.

DNA Extraction and Sequencing

We extracted genomic DNA from ePBR turbidostat cultures and inoculum mixes using a genomic DNA purification kit (QIAGEN N. V.). The DNA samples were then sent to the Michigan State University RTSF Genomics Core for Illumina sequencing and sequence analysis.

Photosynthetic Oxygen Production and Φ_{II}

The technique for measuring photosynthetic oxygen production was adapted from (Spalding 1990). Samples of ePBR turbidostat cultures were concentrated by re-suspension in fresh HS medium at a cell density of 10 µg chlorophyll/mL. Then 2.5 mL of the re-suspended culture was transferred to a 1cm square cuvette cell and inserted it into an IDEA spectrophotometer instrument (described in Hall et al. 2013) with a NeoFox Kit Probe (Ocean Optics Inc.) suspended in the cuvette with the assistance of a 3D-printed cuvette cap. The cuvette was illuminated with 490 µmol photons PAR/m^2/s light (red light emitting diode peak wavelength of 650nm) and sparged with air for 15 minutes via a hypodermic needle at a flow rate of 18.4 mL/minute to reduce the inorganic carbon concentration in the cuvette to atmospheric levels while maintaining normoxia. Then the sparge needle was removed and the algae were allowed to photosynthesize until their internal Ci stores were depleted, as indicated by the cessation of oxygen. Then light intensity was increased to a saturating light intensity of 1000 µmol photons PAR/m^2/s and a specific quantity of sodium bicarbonate was added to the cuvette. Oxygen production was then monitored for 3 minutes, then a fluorescence measurement of the quantum yield of photosystem 2 (Φ_{II}) was taken and the light shuttered for 3 minutes to measure oxygen consumption. Afterward, 5 mM sodium bicarbonate was added to saturate the algae with Ci (Moroney & Tolbert 1985) and the light-Φ_{II}-dark sequence was repeated to get the maximal oxygen production rate. Oxygen production was calculated by subtracting the dark slope from the light slope at each sodium bicarbonate concentration. A representative data set is shown in Figure 38 and the IDEA spectrophotometer and the Python data analysis scripts can be found in APPENDIX F.

Glycolate Excretion

The protocol for measuring glycolate excretion was adapted from (Moroney *et al.* 1986). Samples of ePBR turbidostat cultures were concentrated by re-suspension in fresh HS medium at a cell density of 10 µg chlorophyll/mL, then 2.5 mL was transferred to a 1cm square sealed cuvette cell and inserted it into an IDEA

spectrophotometer instrument. I then connected the cuvette to the recirculating gas system diagrammed in Figure 39. The scripted program for the IDEA spectrophotometer started with 30 minutes of darkness with a normoxia gas mixture (5% CO_2, 20% O_2, and 75% N_2). Then the actinic light turned on to an intensity of 490 µmol PAR/m^2/s (650 nm peak wavelength LED light) with fluorescence measurements every 2 minutes. 20 minutes into the actinic light interval, the gas mixture was replaced with 1% oxygen in nitrogen (N_2) to purge $^{16}O_2$ from the culture medium. Then after 5 minutes with the nitrogen mix, the glycolate dehydrogenase inhibitor amino-oxyacetate (AOA, also known as O-(Carboxymethyl)hydroxylamine) was added to a concentration of 1 mM and the gas was changed to the $^{18}O_2$ gas mix for a 20 minutes. Before or after the 20 minute $^{18}O_2$ gas treatment, I pelleted 600 µL aliquots by quick spin and stored 500 µL samples of the supernatant in a -70°C freezer. Two aliquots were used for glycolate quantification by Calkin's assay (described below) and the other two aliquots were processed for mass spectrometry. A copy of the IDEA spectrophotometer script is included in APPENDIX H.

The protocol for quantifying glycolate was based on that described by Calkins (1943). Aliquots of cell supernatants, obtained by centrifugation at approximately 10,000×G for 5 min, together with standard glycolate concentrations in sterile HS medium, were vacuum dried overnight in an ISS 100 SavantTM SpeedVacTM. The dried samples were then re-suspended with 1 mL 18% (w/v) 2,7-dihydroxynaphthalene in concentrated sulfuric acid and heated to 100°C for 20 minutes. After cooling back to room temperature, and glycolate concentrations were estimated by comparing the sample to reference absorbance measurements at 536 nm.

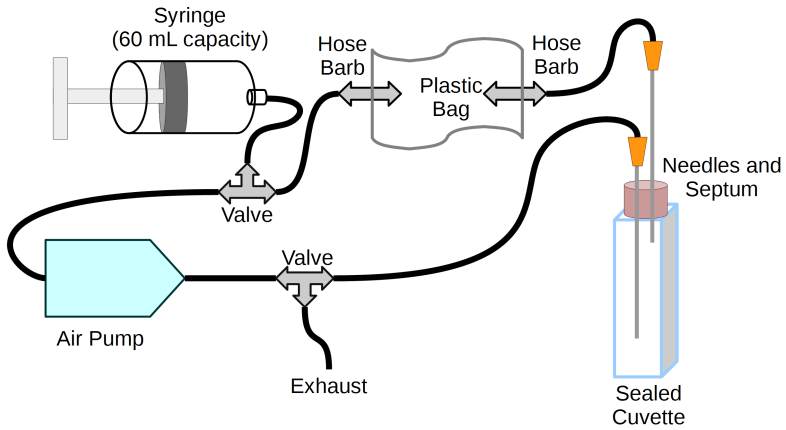

Figure 39: Diagram of apparatus used to control the gas environment of a sample for $^{18}O_2$ labeling experiments. *2.5 mL volume of algae sample would be put in the cuvette, which would then be sealed and inserted into an IDEA spectrophotometer. An electric air pump would recirculate the gas and sparge it through the hypodermic needles inserted through the septum of the cuvette cap. A plastic bag served as a gas reservoir, which could be deflated and filled by toggling the gas valves. Gases mixes were transported in 60 mL volume syringes sealed with luer-lock caps.*

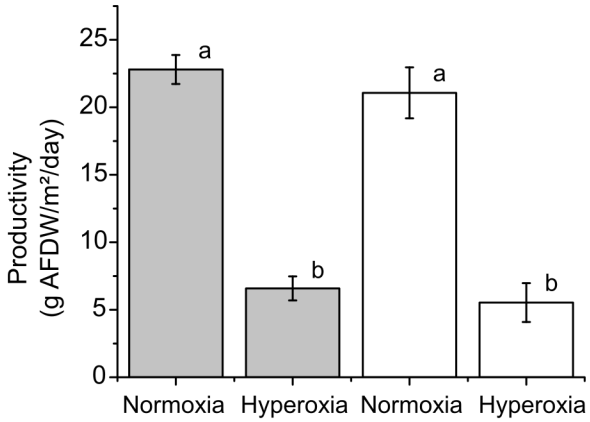

Figure 40: Daily biomass productivity of Chlamydomonas reinhardtii strain NAP10 in normoxia and hyperoxia ePBR turbidostats. *Normoxia ePBRs were sparged with a gas mix of 5% CO_2, 20% O_2, 75% N_2 for 1 minute every hour, while hyperoxia ePBRs were sparged with a gas mix of 5% CO_2, 95% O_2 for 1 minute every hour (grey bars). The turbidostats then had sodium bicarbonate added to their cultures and turbidostat feed carboys to a concentration of 10 mM (white bars), which had no apparent effect on the growth and productivity of the cultures. Error bars represent 1 standard deviation of 3 different turbidostat experiments. Letters indicate Student's T-Test for significance, where bars with the same letter have a P-value > 0.05 and bars that do not share a common letter have a P-value < 0.05.*

Mass spectrometry samples were processed using a protocol based on (Uchida *et al.* 1999) to eliminate high concentration of inorganic salts in HS. Samples were placed on ice and acidified by addition of a final concentration of 0.3 M HCl, then shaken with 15 volumes of diethyl ether. The ether phase was transferred to fresh test tubes shaken with 500 µL of 0.01 N NaOH in water, followed by evaporation of the ether by a stream of dry N_2. The samples were then stored at -70°C and separated by liquid chromatography through a BEH C18 UPLC column and analyzed by mass spectrometry on a Waters Xevo G2-XS running in negative ion electrospray ionization mode. Based on the mechanism of rubisco oxygenation (Tcherkez 2015), it was assumed that glycolate produced by rubisco oxygenation will result in ^{18}O labeling of the carboxyl group.

RESULTS

Hyperoxia Inhibits Growth of C. reinhardtii

As shown in Figure 40, growth of *C. reinhardtii* strain NAP10 in ePBR turbidostats was strongly suppressed by hyperoxia to about 30% of its normoxia rate (6.6 g AFDW/m^2/day vs 23 g AFDW/m^2/day). This is the same level of hyperoxia inhibition as Berry et al. (1976) reported for *C. reinhardtii* strain 137C in cultivated with 3% CO_2 enriched gas mixtures. Increasing the inorganic carbon concentration of the ePBR turbidostat culture medium by the addition of 10 mM sodium bicarbonate did not overcome the effects of hyperoxia. These results

suggest that hyperoxia inhibition is not the result of a competition between O_2 and CO_2, as might be expected under the photorespiration model.

	Percent of Population in Mixed Culture		Monoculture Turbidostat Productivity (g AFDW/m²/day)		
Strain	**Normoxia**	**Hyperoxia**	**Normoxia**	**Hyperoxia**	**(Tolerance)**
CC-125	3%	1%	--	--	
CC-1009	12%	5%	17.6	8.6	(49%)
CC-1373	--	--	16.3	2.8	(17%)
CC-1690	--	--	19.0	5.4	(29%)
CC-1952	4%	2%	--	--	
CC-2342	3%	3%	--	--	
CC-2343	--	--	17.4	3.2	(18%)
CC-2344	24%	2%	15.9	4.7	(29%)
CC-2931	--	--	6.2	6.4	(103%)
CC-2935	--	--	8.2	6.3	(77%)
CC-2936	17%	31%	--	--	
CC-2937	36%	58%	8.2	6.3	(77%)

Table 2: Hyperoxia tolerant and sensitive strain selection data. *In the mixed cultures, equal cell numbers of several strains were mixed together an inoculated into normoxia and hyperoxia ePBR turbisostats. After 4 weeks of turbidostat cultivation, the cell populations were tallied based on the frequency of strain-unique SNPs. A subset of the strains from the mixed culture and closely related strains were then tested in monoculture ePBR turbidostats for their normoxia and hyperoxia productivity rates. Tolerance to hyperoxia is defined as a strains hyperoxia productivity relative to its normoxia productivity. Not all strains were tested in both mixed and mono-cultures, as indicated by the double-dash in the place of a number.*

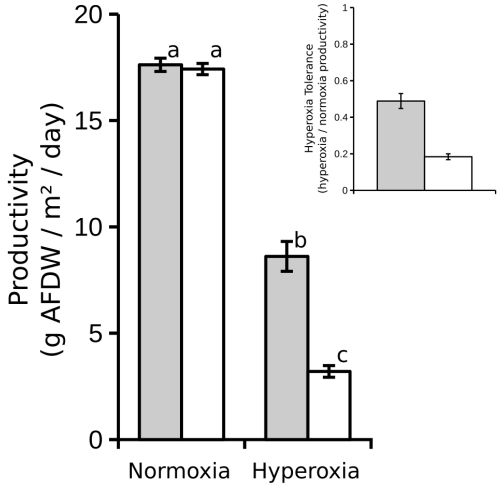

Figure 41: Monoculture photosynthetic productivity rates for the chosen hyperoxia tolerant and sensitive strains in normoxia and hyperoxia ePBR turbidostats. *The hyperoxia tolerant Chlamydomonas reinhardtii strain CC-1009 (gray bars) has nearly identical productivity to the hyperoxia sensitive strain CC-2343 (white bars) under normoxia cultivation, but loses less of its productivity rate under hyperoxia cultivation. The hyperoxia productivity growth rate of each strain relative to its normoxia growth rate was 0.49 for CC-1009 and 0.18 for CC-2343 (inset). Error bars represent 1 standard deviation of 3 different turbidostat experiments. Letters indicate Student's T-Test for significance, where bars with the same letter have a P-value > 0.05 and bars that do not share a common letter have a P-value < 0.05.*

Identification of C. reinhardtii Strains Which Differ in Sensitivity to Hyperoxia

The selection process began with a mixed culture competition wherein normoxia and hyperoxia ePBR turbidostats were inoculated with equal cell numbers of several *C. reinhardtii* strain. Over the course of four weeks, we quantified the relative abundances of each strain in the cultures by taking samples for Illumina sequencing and counting the occurrences of strain-specific single-nucleotide polymorphisms (SNPs), as summarized in Table 2. The strains which demonstrated particularly high or low competitiveness in the hyperoxia culture, along with closely related strains, were then assayed for their hyperoxia sensitivity in monoculture ePBRs. After considering each strain's hyperoxia sensitivity, mating type, and tractability, we chose CC-1009 and CC-2343 as our representative hyperoxia tolerant and sensitive strains respectively. These two strains exhibit nearly identical rates of productivity in normoxia monoculture ePBRs, but CC-1009 retains 49% of its productivity in hyperoxia while CC-2343 retains only 18% (Figure 41).

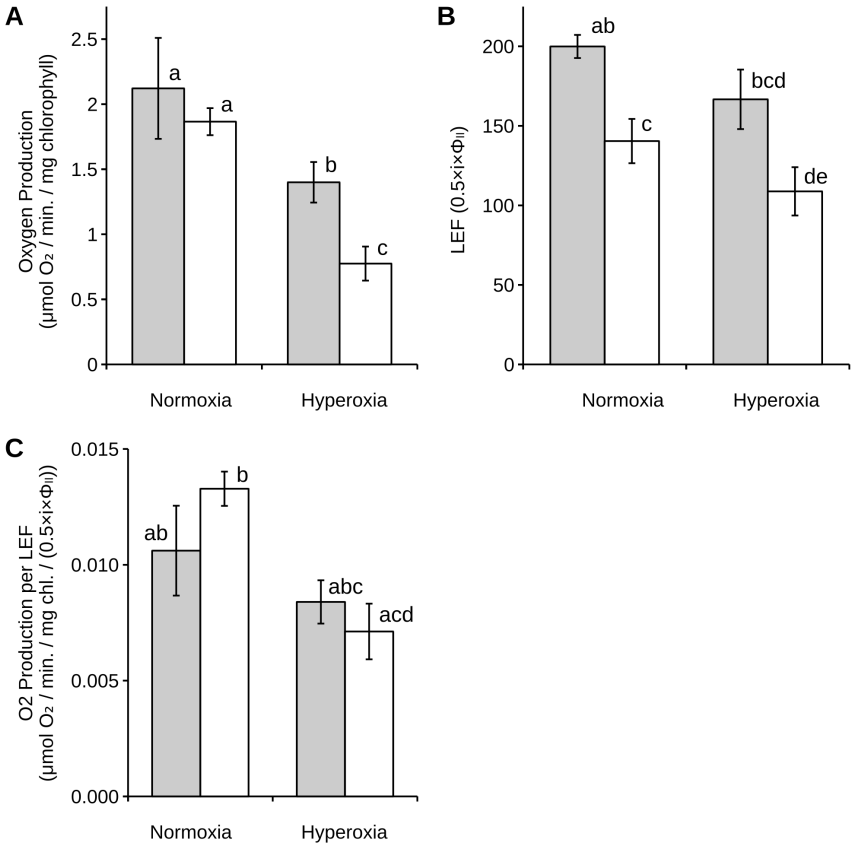

Figure 42: O_2 production rates and estimated LEF for normoxia and hyperoxia cultivated CC-1009 (gray bars) and CC-2343 (white bars). *In normoxia cultivation, the O_2 production rates are similar for the two strains, but decreases in hyperoxia cultivation (panel A). The Φ_{II} values also decrease in hyperoxia cultivation (panel B). The O_2 production per LEF shows a greater dependence on cultivation condition in strain CC-23434 than in CC-1009 (panel C). Error bars represent 1 standard deviation of 3 different turbidostat experiments. Letters indicate Student's T-Test for significance, where bars with the same letter have a P-value > 0.05 and bars that do not share a common letter have a P-value < 0.05.*

Hyperoxia Cultivation Decreases Photosynthetic Efficiency

When cultivated in normoxia ePBRs, cuvette samples of CC-1009 and CC-2343 exhibited similar rates of photosynthetic oxygen production. CC-1009 produced oxygen at a rate of 2.1 µmol O_2/min./mg chlorophyll, compared to 1.9 µmol O_2/min./mg chlorophyll for CC-2343 (Figure 42A). At the same time, CC-1009 had a higher Φ_{II} value than CC-2343 (0.38 versus 0.27) When we estimated the relative rates of LEF as $0.5 \times i \times \Phi_{II}$ (based on PSI/PSII ratios published in Nawrocki et al. 2016), we found that the two strains differed little in their O_2 production per LEF, with values of 0.011 µmol O_2/min./mg chlorophyll/LEF and 0.013 µmol O_2/min./mg chlorophyll/LEF for strains CC-1009 and CC-2343 respectively (Figure 42B, C).

With hyperoxia cultivation, the two strains showed distinct O_2 production behaviors. Both strains had reduced oxygen production rates, but the hyperoxia sensitive CC-2343 lost significantly more of its oxygen production than CC-1009, such that CC-1009 had an O_2 production rate nearly twice that of the sensitive line CC-2343 (1.4 µmol versus 0.77 µmol O_2/min./mg chlorophyll, see Figure 42A). While CC-2343 also had a lower Φ_{II} value (Figure 42B), the decrease in Φ_{II} was not sufficient to account for the loss in O_2 production, as evident in the

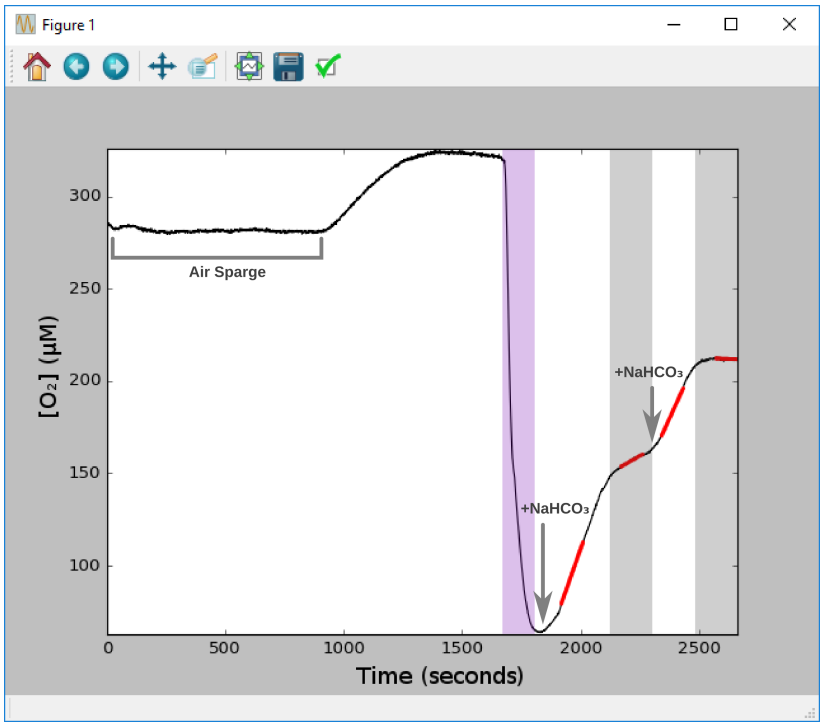

Figure 43: Example of a reduced oxygen baseline oxygen production assay. *This assay works the same as is described in Figure 38, but with the addition of a 30 second N_2 gas purge (magenta shaded box) prior to the addition of sodium bicarbonate, reducing the baseline oxygen of the assay from approximately 300 µM O_2 to approximately 150 µM O_2 at the time-point of the addition of the second addition of sodium bicarbonate.*

strain's decrease in O_2 production per LEF (Figure 42C).

The loss in O_2 production per LEF under hyperoxia cultivation suggests that a significant amount of oxygen is being consumed during photosynthesis, as might be the case if the water-water cycle and/or photorespiration are active. As an additional test, the O_2 production assay was repeated with the following modification: the cuvette was sparged for approximately 30 seconds with N_2 gas to decrease O_2 levels to below 75 µM. Then to achieve stable conditions, sodium bicarbonate was titrated to allow photosynthesis to bring the O_2 level up to 150 µM. At this point, a saturating level of sodium bicarbonate was added to induce Ci-saturated rates of photosynthesis, as shown in the example trace in Figure 43 The rapid reduction of O_2 levels should have partially inhibited O_2 consumption reactions such as photorespiration and the water-water cycle, but should not have affected the extent of photodamage, as repair of photodamage is expected to occur over much longer time scales of hours (reviewed in Yokthongwattana &

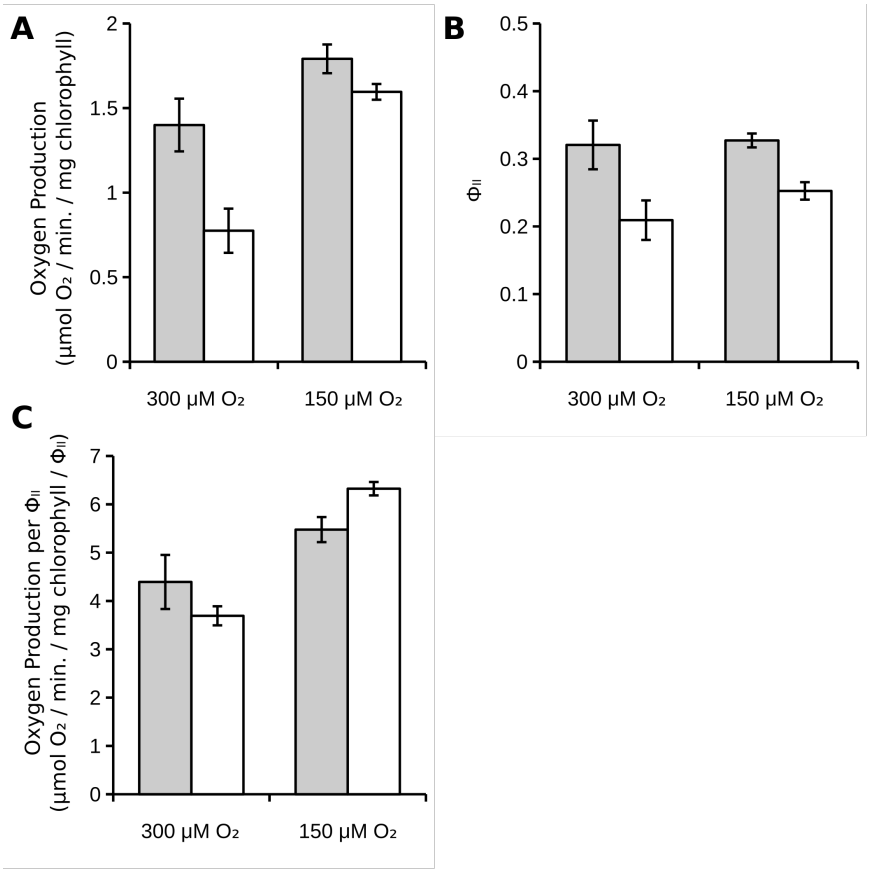

Figure 44: Maximum oxygen production rate and Φ_{II} values for hyperoxia cultivated CC-1009 (gray bars) and CC-2343 (white bars), assayed at a 150 µM O_2 baseline oxygen concentrations. *The data values for 300 µM baseline are reprinted here from Figure 42 for comparison. At a baseline O_2 concentration of 150 µM, the oxygen production rate for hyperoxia tolerant strain CC-1009 increased slightly relative to the 300 µM baseline assay, whereas the oxygen production rate for the hyperoxia sensitive strain CC-2343 increased dramatically (panel A). The Φ_{II} values, however, did not change significantly (panel B). As a result, normalizing the oxygen production rates to the Φ_{II} values for the 150 µM baseline assay puts CC-2343 ahead of CC-1009.*

Melis 2008).

After the reduction of background O_2, the oxygen production rate of CC-2343 greatly increased to the point that it was almost equal to that of the tolerant strain CC-1009 (1.8 µmol O_2/min./mg chlorophyll and 1.6 µmol O_2/min./mg chlorophyll respectively, see Figure 44A). When normalized to LEF, the oxygen productions rates were 0.011 µmol O_2/min./mg chlorophyll/LEF and 0.012 µmol O_2/min./mg chlorophyll/LEF for strains CC-1009 and CC-2343 respectively (Figure 44B, C). The rapid recovery of oxygen production under hypoxia indicated that the principle difference between strains CC-1009 and CC-2343 was due to photorespiration and/or the water-water cycle.

Under all cultivation conditions, the strains appeared to have similar carbon concentrating mechanisms (see APPENDIX G).

Glycolate Excretion as an Indicator of Rubisco Oxygenation

Photorespiration in *C. reinhardtii*, has previously been assayed by measuring glycolate excretion in the presence of AOA, a specific inhibitor of glycolate dehydrogenase (Moroney *et al.* 1986). However, no prior work has been reported to validate this method against an independent measure of photorespiration to assess whether the

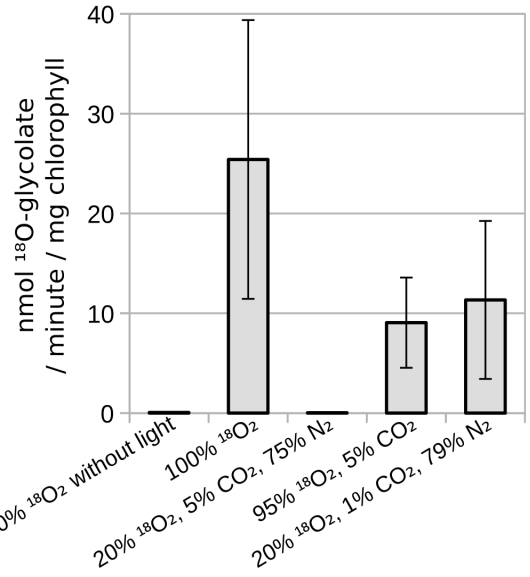

Figure 45: Results of $^{18}O_2$-labeled glycolate excretion assay. *In the absence of light, $^{18}O_2$ did not stimulate the excretion of glycolate and the highest rates of ^{18}O-glycolate excretion were observed in a gas environment consisting of just $^{18}O_2$. The normoxia gas mixture (20% $^{18}O_2$, 5% CO_2, 75% N_2) produced negligible amounts of $^{18}O_2$-glycolate excretion, while the hyperoxia gas mixture (95% $^{18}O_2$, 5% CO_2) resulted in an excretion rate of approximately 9 nmol $^{18}O_2$-glycolate/minute/mg chlorophyll. A nearly identical $^{18}O_2$-glycolate excretion rate was observed in 1% CO_2 normoxia (20% $^{18}O_2$, 1% CO_2, 79% N_2), a condition which has an equivalent O_2:CO_2 ratio as the hyperoxia gas mixture. Error bars represent 1 standard deviation of 3 different turbidostat experiments.*

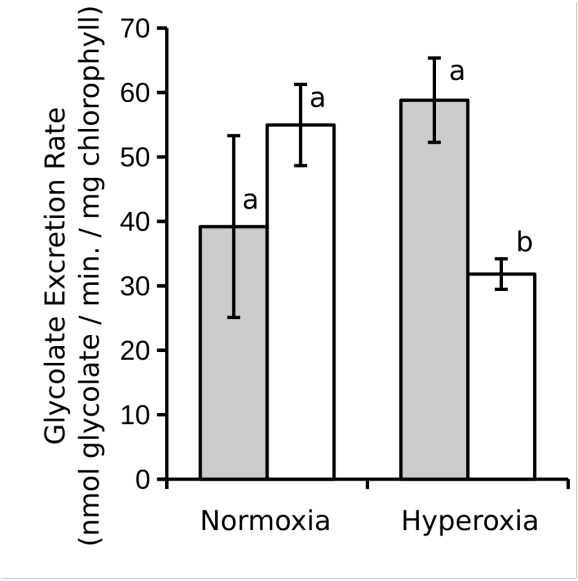

Figure 46: Susceptibility of hyperoxia tolerant strain CC-1009 and hyperoxia sensitive strain CC-2343 to hyperoxia-induced glycolate excretion when cultivated in normoxia and hyperoxia ePBR turbidostats. *In normoxia cultivation, the two strains demonstrated similar susceptibility to glycolate production, but under hyperoxia cultivation, strain CC-1009 is more susceptible to glycolate excretion than strain CC-2343. Error bars represent 1 standard deviation of 3 different turbidostat experiments. Letters indicate Student's T-Test for significance, where bars with the same letter have a P-value > 0.05 and bars that do not share a common letter have a P-value < 0.05.*

glycolate produced did indeed arise from photorespiration. We thus performed the glycolate excretion assay on *C. reinhardtii* NAP10 strain under an atmosphere containing $^{18}O_2$ and analyzed the resulting glycolate using mass spectroscopy to determine whether the produced glycolate carries the isotope label. We found that in the absence of light, negligible amounts of extracellular glycolate were detected and the fraction of ^{18}O-glycolate was equal to the natural abundance of the ^{18}O isotope, whereas illumination resulted in the excretion of ^{18}O-labeled glycolate (see Figure 45). Interestingly, hyperoxia led to ^{18}O-glycolate excretion even under 5% CO_2 or 1% CO_2, treatments that are typically considered to inhibit photorespiration. The ^{18}O-glycolate production at 5% carbon dioxide in oxygen was equal to that of 1% carbon dioxide in normoxia (gas mixtures with equivalent O_2:CO_2 ratios), consistent with the known pathway for photorespiration.

The incorporation of ^{18}O into glycolate was approximately 30%, which we assume is due to the production of $^{16}O_2$ from the oxygen evolving complex of photosystem 2 in the thylakoid membranes in the vicinity of the pyrenoid.

Photorespiration is not the Primary Consumer of Oxygen

When cultivated in normoxia ePBRs, the hyperoxia tolerant strain CC-1009 excreted somewhat less

glycolate than CC-2343, with excretion rates of 39 nmol glycolate/min./mg chlorophyll and 55 nmol glycolate/min./mg chlorophyll respectively (see Figure 46). In hyperoxia cultivation, the trend was reversed, with CC-1009 excreting 59 nmol glycolate/min./mg chlorophyll and CC-2343 excreting 32 nmol glycolate/min./mg chlorophyll. In comparison, the change in light-driven oxygen production observed after the N_2 sparge in the oxygen production assay (Figure 44) amounted to +0.39 µmol O_2/min./mg chlorophyll and +0.82 µmol O_2/min./mg chlorophyll for strains CC-1009 and CC-2343 respectively, more than ten times the observed rates of glycolate excretion.

Mehler Cycling Assay Inconclusive

Existing methods for the determination of flux through the Mehler pathway were not sensitive enough to be applied to compare Mehler cycling in CC-1009 and CC-2343 (see APPENDIX I).

CC-2343 is More Productive Than CC-1009 Under Limited Carbon Dioxide Levels

In air-sparged ePBR turbidostats, where the Ci concentration is very low, CC-1009 was less productive than CC-2343, with daily biomass productivity rates of 1.1 g AFDW/m^2/day and 2.1 g AFDW/m^2/day respectively (Figure 47A). This reversal relative to hyperoxia cultivation suggests that adaptation to hyperoxia and low-Ci conditions require different strategies.

When assayed for photosynthetic oxygen production (Figure 47B), their O_2 production rates were nearly

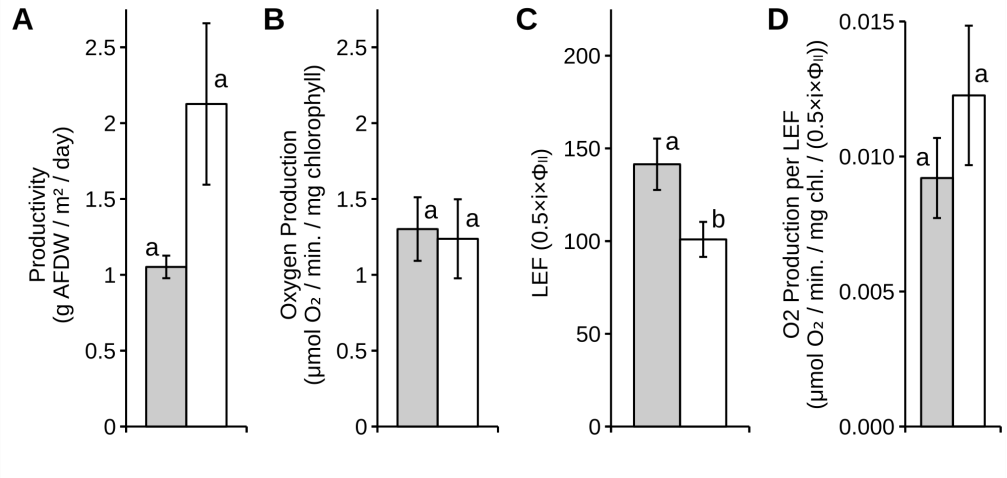

Figure 47: Performance of hyperoxia tolerant strain CC-1009 (gray bars) and hyperoxia sensitive strain CC-2343 (white bars) when cultivated in air-sparged ePBR turbidostats. *The daily turbidostat biomass productivity of strain CC-1009 was approximately half that of strain CC-2343 (panel A). The oxygen production rate as a function of added bicarbonate was the same for both strains (panel B), though CC-2343 had a lower estimated LEF (panel C) than CC-1009, resulting in a modestly higher amount of O_2 production per LEF. Error bars represent 1 standard deviation of 3 different turbidostat experiments. Letters indicate Student's T-Test for significance, where bars with the same letter have a P-value > 0.05 and bars that do not share a common letter have a P-value < 0.05.*

identical, with 1.3 µmol O_2/min./mg chlorophyll and 1.2 µmol O_2/min./mg chlorophyll for strains CC-1009 and CC-2343 respectively. CC-2343 had a lower Φ_{II} and therefore a lower estimated LEF (Figure 47C), though this difference was not enough to make for a significant difference in the two strains' O_2 production per LEF (Figure 47D).

CONCLUSIONS

The Role of the Water-Water Cycle

Under hyperoxia cultivation, strain CC-1009 was more productive than CC-2343. Both strains demonstrate a similar capacity for O_2 production when assayed under 150 µM O_2, but when assayed under 300 µM O_2 strain CC-2343 lost a significant fraction of its oxygen productivity while CC-1009 was less affected. Neither strain demonstrated a capacity for photorespiration comparable to the observed changes in oxygen production. Taken together, this means that the loss of oxygen production is due to the diversion of LEF to water-water cycle pathways (Mehler cycle, Flv-mediated oxygen reduction, etc.), and that CC-1009 diverts less of its LEF than CC-2343. With less diversion of LEF to the water-water cycle, strain CC-1009 is able to fix more carbon during hyperoxia cultivation than strain CC-2343. This difference allows strain CC-1009 to both out-perform and out-compete strain CC-2343 in carbon-replete hyperoxia cultures.

Trade-Off Between Hyperoxia Tolerance and Low-Ci Productivity

The hyperoxia sensitive strain CC-2343 was better adapted to a low-Ci environment than the hyperoxia tolerant strain CC-1009. This finding runs counter to the assumption of Kliphuis et al. (2011) and others that hyperoxia inhibition is a function of the O_2:CO_2 ratio, but it is consistent with the evolutionary context of hyperoxia photosynthesis. Hyperoxia in nature is the result of high rates of photosynthesis, which requires a high concentration of Ci. Therefore an alga that evolved to live in a low carbon environment would rarely be challenged with hyperoxia while an alga that evolved in a high carbon environment would be more likely to encounter hyperoxia. Consistent with this evolutionary model, strain CC-1009 is better adapted to a high carbon dioxide and oxygen environment while strain CC-2343 is better adapted to a low carbon dioxide and oxygen environment.

The water-water cycle may pose a direct trade-off between hyperoxia and low-Ci performance. In a normoxic environment, there would not typically enough diversion of LEF to water formation to significantly inhibit growth, and if Ci is limiting then the water-water cycle is reported to protect the light reactions from ROS-induced photodamage (as described in Allahverdiyeva et al. 2014). However in hyperoxia, the increased oxygen

concentration increases the flux of electrons into the electron acceptors, even to the point where it is in competition with carbon assimilation, especially at high carbon dioxide concentrations where the rate of carbon assimilation (rather than carbon acquisition) is the principle factor limiting the growth rate.

UNANSWERED QUESTIONS AND FUTURE DIRECTIONS

This study examined the mechanisms of hyperoxia tolerance and sensitivity by focusing on two strains of *C. reinhardtii*, CC-1009 and CC-2343, which exhibit differential sensitivity to hyperoxia cultivation. However, it is not yet known whether the mechanism of hyperoxia tolerance and sensitivity in these two strains is the same for all strains of *C. reinhardtii* or for other species of algae. More strains and species need to be tested.

This study did not identify which genes are responsible for conferring hyperoxia tolerance on strain CC-1009. Having a genetic understanding of hyperoxia tolerance would be immensely useful to anyone trying to breed hyperoxia tolerance into an algal strain that is hyperoxia sensitive but otherwise possesses desirable traits for commercial production. Work is already underway to find these hyperoxia tolerance genes by a genome-wide association study on the offspring from a crossing of CC-1009 and CC-2343.

Another open question from this study is the exact partitioning of the water-water cycle pathways responsible for hyperoxia sensitivity. How much of the oxygen consumption is Mehler reaction? How much is activity by flavodiiron proteins, plastid terminal oxidases, and others? Uncovering the answers to this mystery will require the development of new techniques that are more direct than what has been used so far to measure oxygen uptake.

And finally, there are fundamental gaps in the basic knowledge of these processes that were tested in this study. None of the glycolate transporters in *C. reinhardtii* have been identified, yet glycolate must be transported out of the chloroplast and into the mitochondria and out into the extracellular environment. With respect to the Mehler reaction, it is unclear whether the extracellular hydrogen peroxide concentration bares any relation to the intracellular concentration. If hydrogen peroxide does measure the flux of Mehler cycling, then it is rather curious that Roach et al. (2015) reported H_2O_2 excretion only under high levels of Ci and not under the low-Ci conditions that the model of Mehler cycling would predict.

APPENDICES

APPENDIX A

E-TADA DESIGN

https://www.raspberrypi.org/products/raspberry-pi-3-model-b/

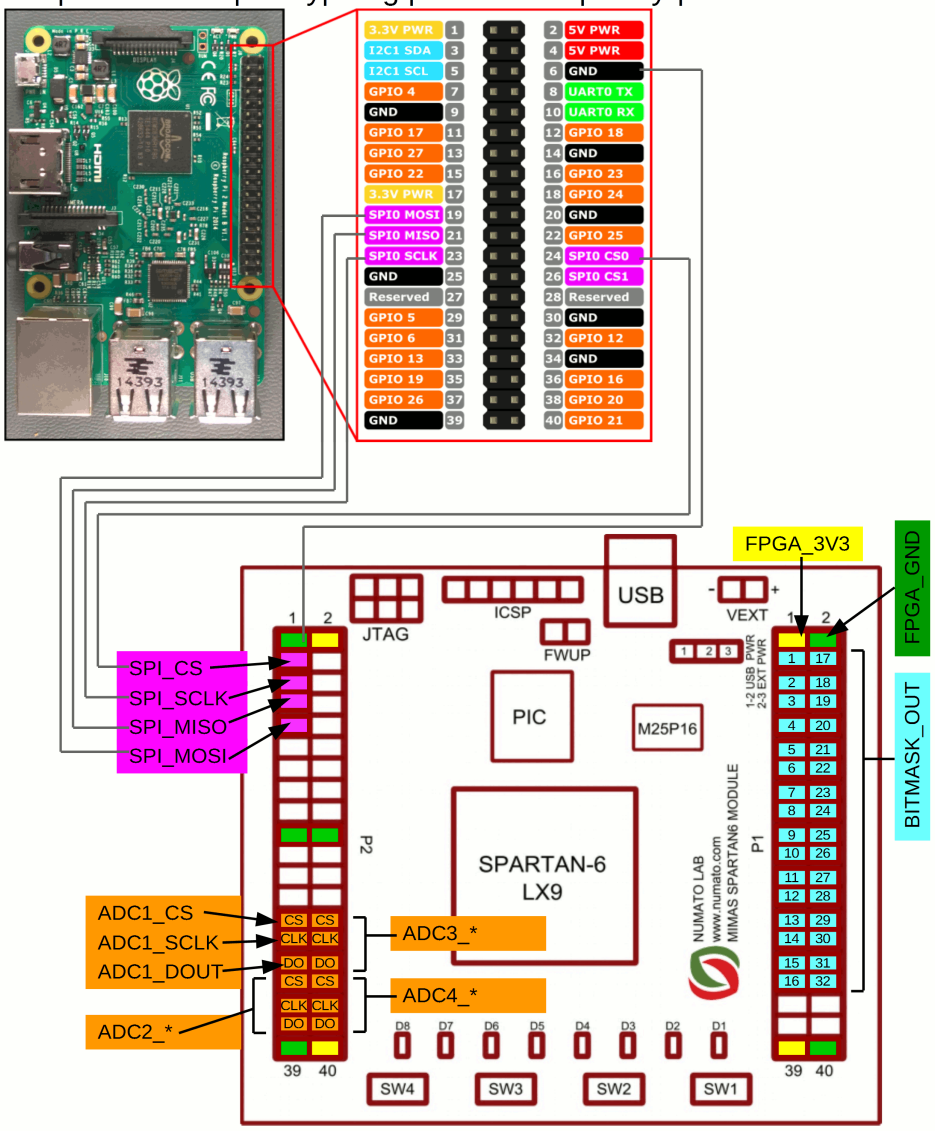

http://numato.com/mimas-spartan-6-fpga-development-board/

Figure 48: Wiring diagram of the E-TADA device. *Specific I/O pins on the Raspberry Pi microcomputer must be directly connected to corresponding pins on the Numato Mimas FPGA prototyping board.*

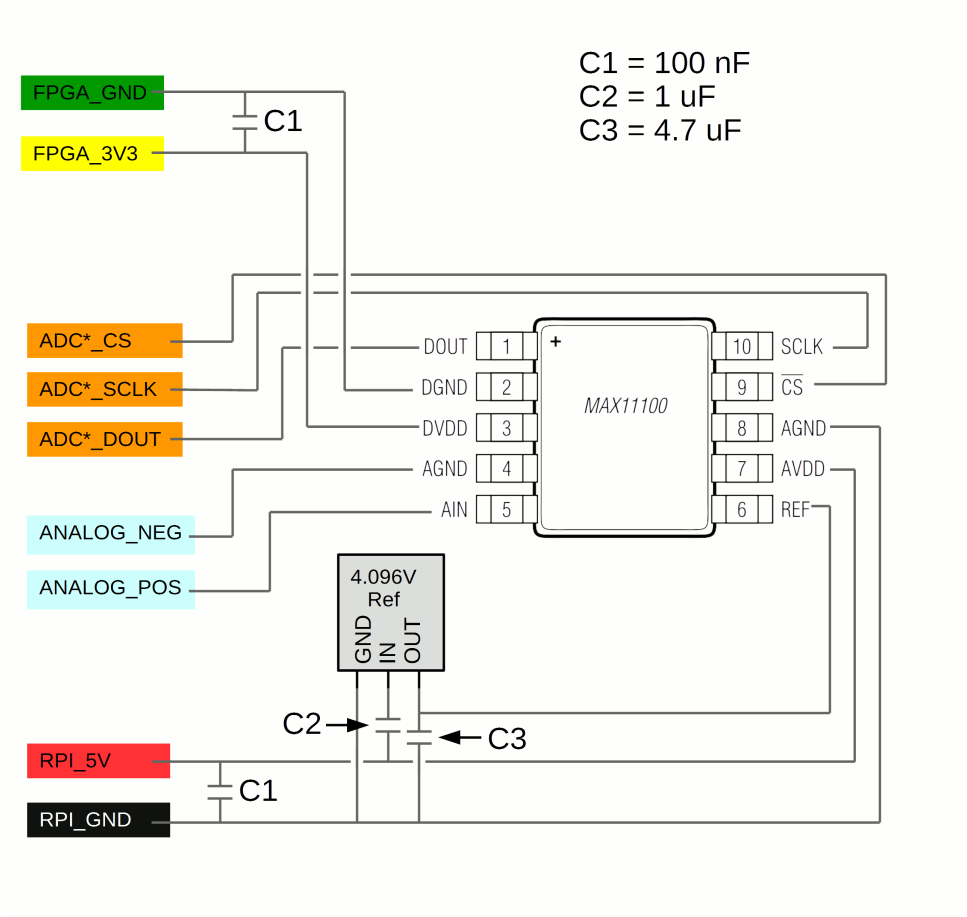

Figure 49: Wiring diagram for the analog-to-digital (ADC) microchips employed for data acquisition. *Communication between the FPGA and each MAX11100 chip relies on three digital I/O wires. Analog values between 0 and +4.096V can be read. Up to 4 ADC chips can be connected to the E-TADA and they can be independently triggered.*

APPENDIX B

IDEA SPECTROPHOTOMETER DATA ANALYSIS WITH JAVASCRIPT

```
[ IDEA spec ECS-NPQ-qP (490 uE).txt ]

set_base_file
ref_channel(1)

!lt
!sat

record_events(1)
plot_clear
record_files(1)
note_query
record_script

number_protocols(5)
gain_slop(0.7)

'basic dirk
current_protocol(1)
in_channel(0)
adc_gain(bip10volts)
measuring_pulse_duration(20u)
m_number_loops(3)
m_intensity(0,0,0)
l_measuring_interval(2m,2m,2m)
m_pulse_set(250,250,250)
m_number_measuring_lights(1)
m_measuring_light(7)
m_detector_gain(3)
m_reference_gain(4)
baseline_start(241)
baseline_end(250)

'basic fluorescence
current_protocol(2)
in_channel(0)
adc_gain(bip10volts)
measuring_pulse_duration(20u)
m_number_loops(5)
m_intensity(0,0,0,0,0)
m_pulse_set(100,100,200,100,100)
m_measuring_light(8)
l_measuring_interval(5m,5m,5m,5m,5m)
M_detector_gain(5)
m_reference_gain(0)
baseline_start(1)
baseline_end(10)

'traces
number_traces(100)

current_trace(1)
save_mode(file_append)
time_mode(sequential)
trace_note(fluorescence)
trace_protocol(2)

current_trace(2)
save_mode(file_append)
time_mode(sequential)
trace_note(505 nm)
trace_protocol(1)
```

```
current_trace(3)
save_mode(file_append)
time_mode(sequential)
trace_note(520)
trace_protocol(1)

current_trace(4)
save_mode(file_append)
time_mode(sequential)
trace_note(535)
trace_protocol(1)

'start experiments

f_shutter(0)
stir(1)
#sat(1)=255
#lt(0)=0
#lt(1)=0
intensity(@lt(0))

' dark adaptation
intensity(0)
wait(1500)
far_red(1)
wait(300)
far_red(0)

'fM
sub(sinfl)
wait(30)

#lt(1)=28
intensity(@lt(1))
wait(30)

' 10 minutes in the light
sub(measurements)

' time to change things
stir(0)
wait(600)
stir(1)

sub(measurements)

' time to change things
stir(0)
wait(600)
stir(1)

sub(measurements)

#lt(1)=0

' dark recovery
intensity(@lt(0))
sub(dark_recovery)

far_red(0)

intensity(0)
stir(0)
```

```
end

'fluorescence induction
measurements|

lb(2,10)
sub(sinfl)
wait(51)
sub(sindirk)
wait(6)
sub(sindirk)
wait(6)
sub(sindirk)
wait(6)
sub(sindirk)
wait(6)

plot_raw(3)
le(2)

return

'fluorescence recovery
dark_recovery|
sub(sinfl)

lb(2,9)
far_red(1)
wait(112)
far_red(0)
sub(sinfl)
le(2)
return

'single fluorescence trace
sinfl|

current_trace(1)
current_protocol(2)
m_intensity(@lt(1),@sat(1),0,0,0)
m_far_red(0,0,0,1,0)

stir(0)
f_shutter(1)
wait(5)
m_trace
intensity(@lt(1))
stir(1)
plot_raw(1)

return

'single 520nm dirk
sindirk|

current_trace(3)
current_protocol(1)
m_intensity(@lt(1),0,@lt(1))

stir(0)
f_shutter(0)
wait(5)
m_trace
```

```
stir(1)
return
```

```
[ IDEA spec ECS-NPQ-qP (490 uE) folder processor.js ]

/*
This script is based on 'PureJS Script for ECS-NPQ-qP.js' in HALLCC003:15 to be run in
the PureJS program found in HALLCC003:14

See also: https://github.com/cyanobacteruim/PureJS
*/

// Rhino JS engine
//importPackage(Packages.purejs.util);

// Nashorn JS Engine
var FileIO = Java.type("purejs.util.FileIO");
var File = Java.type("java.io.File");
var JOptionPane = Java.type("javax.swing.JOptionPane");
var JFileChooser = Java.type("javax.swing.JFileChooser");
var Charset = Java.type("java.nio.charset.Charset");
var BufferedWriter = Java.type("java.io.BufferedWriter");
var Files = Java.type("java.nio.file.Files");

var numPtsPerMeasurement = 600;
var FRstart = 400;
var FRstop = 500;
var numPtsPerECS = 750;
var measurementInterval = 2;
var artefactOffset = 0;
var PARintensity = 490; // in uE

var consecutiveECSaveraging = 4;

var StatsHelper = {

 sum: function (numberArray){
  var d = 0;
  for(var i = 0; i < numberArray.length; i++){
   d += numberArray[i];
  }
  return d;
 },

 mean: function (numberArray){
  var sum = 0;
  for(var i = 0; i < numberArray.length; i++){
   sum += numberArray[i];
  }
  return sum / numberArray.length;
 },

 sumOfSquares: function (numberArray){
  var squared = new Array();
  for(var i = 0; i < numberArray.length; i++){
   squared[i] = numberArray[i] * numberArray[i];
  }
  return this.sum(squared);
 },

 variance: function (numberArray){
  var ave = this.mean(numberArray);
  var deltas = new Array();
  for(var i = 0; i < numberArray.length; i++){
   deltas[i] = numberArray[i] - ave;
  }
```

```
 return this.sumOfSquares(deltas) / (numberArray.length - 1);
},

standardDeviation: function (numberArray){
 var v = this.variance(numberArray);
 return Math.sqrt(v);
},

Rsquared: function (xValues, yValues, functionOfX){
 if(xValues.length != yValues.length){
  throw "the number of independent and dependant variable values are not equal";
 }
 var sosq =this.sumOfSquares(yValues);
 var residualSquared = new Array();
 for(var i = 0; i < xValues.length; i++){
  var delta = yValues[i] - functionOfX(xValues[i]);
  residualSquared[i] = (delta * delta);
 }
 var sumOfSquaredResiduals = this.sum(residualSquared);
 return 1 - (sumOfSquaredResiduals / sosq);
},

correlationCoefficient: function (xValues, yValues) {
 // Pearson product-moment correlation coefficient, as described on wikipedia
 if(xValues.length != yValues.length){
  throw "Number of X and Y values must be the same";
 }
 var n = xValues.length;
 var products = new Array();
 for(var i = 0; i < n; i++){
  products[i] = (xValues[i] * yValues[i]);
 }
 var xAve = this.mean(xValues);
 var yAve = this.mean(yValues);
 var xDev = this.standardDeviation(xValues);
 var yDev = this.standardDeviation(yValues);
 var sumOfProducts = this.sum(products);
 return (sumOfProducts - (n * xAve * yAve))/((n - 1) * xDev * yDev);
},
}

function writeToFile(content,filepath){
 var charset = Charset.forName("UTF-8");
 var writer = null;
 try {
  writer = Files.newBufferedWriter((new File(filepath)).toPath(), charset);
  writer.write(content.toString());
  writer.flush();
 } catch (x) {
  println("IOException: "+ x);
 } finally {
  if (writer != null) writer.close();
 }
}

function setCharAt(str,index,chr) {
 if(index > str.length-1) return str;
 return str.substr(0,index) + chr + str.substr(index+1);
}

function averageTogetherFiles(fileArray){
 println("Averaging files "+fileArray);
 var fileOut = fileArray[0];
```

```
 for(var h = 1; h < fileArray.length; h++){
  for(var s = 0; s < fileOut.length; s++){
   if(fileOut.charAt(s) != fileArray[h].charAt(s)){
    fileOut = setCharAt(fileOut,s,"+");
   }
  }
 }

 var tables = new Array();
 for(var i = 0; i < fileArray.length; i++){
  tables[i] = FileIO.readFileAsTable(fileArray[i]);
 }

 var averages = new Array();
 var deviations = new Array();

 var columnCount = tables[0].getSize(0);
 var rowCount = tables[0].getSize();
 for(var row = 0; row < rowCount; row++){
  averages[row] = new Array();
  deviations[row] = new Array();
 }

 // row 0 is header
 var header = new Array();
 for(var col = 0; col < columnCount; col++){
  header[col] = tables[0].get(col,0);
  averages[0][col] = header[col];
  deviations[0][col] = "1 std. dev.";
  for(var row = 1; row < rowCount; row++){
   if(col >= tables[0].getSize(row)) {continue;}
   var values = new Array();
   try{
    for(var k = 0; k < tables.length; k++){
     values[k] = tables[k].getAsNumber(col,row);
    }
    averages[row][col] = StatsHelper.mean(values);
    deviations[row][col] = StatsHelper.standardDeviation(values);
   } catch(e){
    averages[row][col] = "--";
    deviations[row][col] = "--";
   }
  }
 }

 var output = "";
 for(var row = 0; row < rowCount; row++){
  var line = "";
  for(var col = 0; col < columnCount; col++){
   if(col != 0){
    line = line + "\t";
   }
   line = line + averages[row][col] + "\t" + deviations[row][col];
  }
  line += "\n";
  output += line;
 }
 writeToFile(output,fileOut);
 println("Averaged files "+fileArray+" and saved to "+fileOut);
}

function getBlank(){
 println("Open blank measurement");
```

```
 var blankData = FileIO.readFileAsTable(FileIO.askForFile("Get data file"));
 if(blankData == null) return 0;
 var sum = 0;
 for(var i = 0; i < blankData.getSize(); i++){
  sum += blankData.getAsNumber(1,i);
 }
 var ave = sum / blankData.getSize();
 artefactOffset  = ave;
 println("Blank offset = " + ave);
 return ave;
}

function getFs(table){
  var sum = 0;
  var count = 0;
  for(var i = 1; i < 32; i++){
 sum += table.getAsNumber(1,i);
 count++;
  }
  return (sum/count) - artefactOffset;
}
function getFm(table){
  var sum = 0;
  var count = 0;
  for(var i = 120; i <= 130; i++){
 sum += table.getAsNumber(1,i);
 count++;
  }
  return (sum/count) - artefactOffset;
}
function getF0p(table){
  var points = new Array(); // handle dark PQ reduction by taking lowest point,
// EXCLUDING the far-red pulse
  var count = 0;
  for(var i = 201; i < numPtsPerMeasurement; i++){
  if(i >= FRstart && i <= FRstop){ // exclude FR points (instrument artifact)
 continue;
  }
 points[count] = table.getAsNumber(1,i);
 count++;
  }
  var min = Math.min.apply(null,points); // array min operation
  return (min) - artefactOffset;
}

function calculateFluorescentParameters(masterTable){
 var slices  = masterTable.slice(numPtsPerMeasurement);
 F0=getFs(slices.get(0));
 println("F0="+F0);
 Fm=getFm(slices.get(0));
 println("Fm="+Fm);
 Fv=Fm-F0;
 println("Fv="+Fv);
 println("time (min.)\tFs'\tFm'\tFo'\tPhi2\tNPQ\tqP\tqL");
 for(i = 0; i < slices.size(); i++){
  Fs=getFs(slices.get(i));
  Fmp=getFm(slices.get(i));
  Fop = getF0p(slices.get(i));
  Phi2 = (Fmp-Fs)/Fmp;
  NPQ = (Fm-Fmp)/Fm;
  qP = (Fmp - Fs) / (Fmp - Fop);
  qL = qP * (Fop / Fs);
  println((measurementInterval*i)
```

```
+"\t"+Fs+"\t"+Fmp+"\t"+Fop+"\t"+Phi2+"\t"+NPQ+"\t"+qP+"\t"+qL);
 }
}

var fittingFormula = {
 C: new Array(0,1,1), // coefficients Y0, A, and tau
 f: function(x) {return this.C[0] + this.C[1] * Math.exp(-1 * x / this.C[2]);},
 toString: function(){return this.C[0]+" + "+this.C[1]+" * Math.exp(-1 * x /
"+this.C[2]+")"}
};

function err(x,y,formula){
 var sum = 0;
 for(var n = 0; n < x.length && n < y.length; n++){
  var t = x[n];
  var d = y[n];
  var sim = formula.f(t);
  sum += Math.abs(sim - d);
 }
 return sum;
}
function Rsqr(x,y,formula){
 var average = 0;
 var iii = 0;
 for(var n = 0; n < x.length && n < y.length; n++){
  average += y[n];
  iii++;
 }
 average = average / iii;
 var sumResidual = 0;
 var sumTotal = 0;
 for(var n = 0; n < x.length && n < y.length; n++){
  var t = x[n];
  var d = y[n];
  var sim = formula.f(t);
  sumResidual += (d - sim)*(d - sim);
  sumTotal += (d - average)*(d - average);
 // println(x[n]+"\t"+y[n]+"\t"+sim);
 }
 return 1 - (sumResidual / sumTotal);
}
function printFittingResult(x,y,formula){
 println("t\tY\tf(t)");
 for(var i = 0; i < x.length; i++){
  println(x[i]+"\t"+y[i]+"\t"+formula.f(x[i]));
 }
// println("error="+err(x,y,formula));
// println("formula: "+formula.toString());
}
/**
formula = {
 C: new Array(0,1,1), // coefficients Y0, A, and tau
 f: function(x) {return this.C[0] + this.C[1] * Math.exp(-1 * x / this.C[2]);},
 toString: function(){return this.C[0]+" + "+this.C[1]+" * Math.exp(-1 * x /
"+this.C[2]+")"}
};
*/
function primeFormula(x,y){
 var fitter = {
  C: new Array(0,1,1), // coefficients Y0, A, and tau
  f: function(x) {return this.C[0] + this.C[1] * Math.exp(-1 * x / this.C[2]);},
  toString: function(){return this.C[0]+" + "+this.C[1]+" * Math.exp(-1 * x /
"+this.C[2]+")"}
```

```
 };
 var endAve = 0;
 var aveSize = 0;
 for(var m = y.length - 1; m >= y.length / 2; m--){
  endAve += y[m];
  aveSize++;
 }
 endAve = endAve / aveSize;
 fitter.C[0] = endAve; // set y0 to asymptote
 fitter.C[1] = y[0] - endAve; // set A to delta
 var halfVal = Math.abs((endAve - y[0]) / 2);
 for(var i = 0; i < x.length && i < y.length; i++){
  if(Math.abs(y[i] - y[0]) > halfVal){
   fitter.C[2] = (x[i]-x[0]) / Math.log(2); // set tau based on apparent half-life
   break;
  }
 }
 return fitter;
}

/**
formula = {
 C: new Array(0,1,1), // coefficients Y0, A, and tau
 f: function(x) {return this.C[0] + this.C[1] * Math.exp(-1 * x / this.C[2]);},
 toString: function(){return this.C[0]+" + "+this.C[1]+" * Math.exp(-1 * x /
"+this.C[2]+")"}
};

tweaks the coefficients of the formula object to improve the fit.
returns number of iterations computed
 * */
function improveFit(x,y,formula,delta, maxIterations){
 // adjust the variables by the delta amount in decrease the Chi-squared value
 var lastChi;
 var iterations = 0;
 do{
  lastChi = err(x,y,formula);
  for(var i = 0; i < formula.C.length; i++){
   var oldC = formula.C[i];
   var upC = formula.C[i]+delta;
   var downC = formula.C[i]-delta;
   var currentChi = err(x,y,formula);
   formula.C[i] = upC;
   var chiPlus = err(x,y,formula);
   formula.C[i] = downC;
   var chiMinus = err(x,y,formula);
   if(chiPlus < currentChi && chiPlus < chiMinus){
    // increase the variable
    formula.C[i] = upC;
   } else if(chiMinus < currentChi){
    // decrease the variable
    formula.C[i] = downC;
   } else {
    // no change
    formula.C[i] = oldC;
   }
  }
  iterations++;
 } while (lastChi > err(x,y,formula) && iterations < maxIterations);
 return iterations;
}

function getECSformula(dataTableSlice,recalcAbsorption){
```

```
 var table;
 if(dataTableSlice instanceof Array){
  // already a 2D array
  table = dataTableSlice;
 } else {
  // make a 2D array
  table = new Array();
  for(var c = 0; c < 4; c++){
   table.push(new Array());
   for(var r = 0; r < dataTableSlice.getSize(); r++){
    table[c].push(sliceArray[t].getAsNumber(c,r));
   }
  }
 }
 var dirkStart = 250;
 var xVals = new Array();
 var yVals = new Array();
 if(recalcAbsorption == true){
  var baseline = 0;
  var divisor = 0;
  for(var k = 65; k < 215; k++){
   baseline += table[1][k];
   divisor++;
  }
  baseline = baseline / divisor;
  for(var k = 0; k < table[0].length; k++){
   xVals[k] = table[0][k];
   yVals[k] = -1 * Math.log(table[1][k] / baseline);
  }
 } else {
  for(var k = 0; k < table[0].length; k++){
   xVals[k] = table[0][k];
   yVals[k] = table[3][k];
  }
 }
 var numPts;// = 25; // set to lowest point
 var indexOfLowestPoint = dirkStart;
 var lowestVal = yVals[indexOfLowestPoint];
 for(var k = dirkStart; k < 400; k++){
  if(yVals[k] < lowestVal){
   lowestVal = yVals[k];
   indexOfLowestPoint = k;
  }
 }
 numPts = indexOfLowestPoint - dirkStart + 1;
 var t0 = xVals[dirkStart];
 var y0 = yVals[dirkStart];
 var t = new Array();
 var data = new Array();
 for(var i = 0; i < numPts; i++){
  t[i] = xVals[dirkStart + i] - t0;
  data[i] = yVals[dirkStart + i] - y0;
 }
 var fittingFormula = primeFormula(t,data);
// println("formula: "+fittingFormula.toString());
 var iterations = 0;
 for(var l = 0; l < 10; l++){
  iterations += improveFit(t,data,fittingFormula,0.1,1000);
  iterations += improveFit(t,data,fittingFormula,0.01,100);
  iterations += improveFit(t,data,fittingFormula,0.001,100);
  iterations += improveFit(t,data,fittingFormula,0.0001,100);
  iterations += improveFit(t,data,fittingFormula,0.00001,100);
  iterations += improveFit(t,data,fittingFormula,0.000001,100);
```

```
 }
// printFittingResult(t,data,fittingFormula);
 var fitError = err(t,data,fittingFormula); // sum of variances
 fittingFormula.fitError = fitError;
 var R_squared = Rsqr(t,data,fittingFormula);
 fittingFormula.R_squared = R_squared;
 return fittingFormula;
}

/** Alternative to formula fitting. Problem with formula fitting is that
 * there's a linear artifact in the decay data and the tau value is
 * definitely changing enough to change how many point are needed for a
 * good fit */
function getECShalflife(dataTableSlice){
 var decayArray = new Array();
 var count = 0 ;
 var t0 = dataTableSlice.getAsNumber(0,250);
 var y0 = dataTableSlice.getAsNumber(3,250);
 for(var i = 250; i < 350; i++){
  decayArray[count] = dataTableSlice.getAsNumber(3,i);
  count++;
 }
 var min = Math.min.apply(null,decayArray); // array min operation
 var halfy = (y0+min)/2;
 var thalf;
 for(var i = 250; i < 350; i++){
  if(dataTableSlice.getAsNumber(3,i) < halfy){
   thalf = dataTableSlice.getAsNumber(0,i)
   break;
  }
 }
 return (thalf - t0);
}

function getECSInitialSlope(dataTableSlice){
 var i = 0;
 var s1 = (dataTableSlice.getAsNumber(3,251+i) - dataTableSlice.getAsNumber(3,250)) /
(dataTableSlice.getAsNumber(0,251+i) - dataTableSlice.getAsNumber(0,250));
 i = 1;
 var s2 = (dataTableSlice.getAsNumber(3,251+i) - dataTableSlice.getAsNumber(3,250)) /
(dataTableSlice.getAsNumber(0,251+i) - dataTableSlice.getAsNumber(0,250));
 i = 2;
 var s3 = (dataTableSlice.getAsNumber(3,251+i) - dataTableSlice.getAsNumber(3,250)) /
(dataTableSlice.getAsNumber(0,251+i) - dataTableSlice.getAsNumber(0,250));
 return (s1+s2+s3)/3;
}

/**
Averages multiple slices together into a 2D array
@param sliceArray an array of slice objects
@param tableWidth Number of columns in the table
@return an array of arrays, where the first dimension is the
column number and the second dimension is the row number
*/
function averageTogether(sliceArray, tableWidth){
 var table = new Array();
 var numRows = sliceArray[0].getSize();
 for(var t = 0; t < sliceArray.length; t++){
  if(sliceArray[t].getSize() < numRows){
   numRows = sliceArray[t].getSize();
  }
 }
 for(var c = 0; c < tableWidth; c++){
```

```
  table.push(new Array());
  for(var r = 0; r < numRows; r++){
   var myval = 0;
   for(var t = 0; t < sliceArray.length; t++){
    myval += sliceArray[t].getAsNumber(c,r);
   }
   myval = myval / sliceArray.length;
   table[c].push(myval);
  }
 }
 return table;
}

function calcNPQandECS(file_flr,file_ecs){
 var flrTable = FileIO.readFileAsTable(file_flr);
 var fslices  = flrTable.slice(numPtsPerMeasurement);
 F0=getFs(fslices.get(0));
 println("F0="+F0);
 Fm=getFm(fslices.get(0));
 println("Fm="+Fm);
 Fv=Fm-F0;
 println("Fv="+Fv);

 var dataTable = {};
 dataTable.time = new Array();
 dataTable.Fs = new Array();
 dataTable.Fmp = new Array();
 dataTable.Fop = new Array();
 dataTable.Phi2 = new Array();
 dataTable.NPQ = new Array();
 dataTable.qP = new Array();
 dataTable.qL = new Array();
 dataTable.time2 = new Array();
 dataTable.tau = new Array();
 dataTable.y0 = new Array();
 dataTable.A = new Array();
 dataTable.gH = new Array();
 dataTable.vH = new Array();
 dataTable.pmf = new Array();
 dataTable.LEF = new Array();
 dataTable.CEF = new Array();
 dataTable.fitError = new Array();
 dataTable.fitFormula = new Array();
 dataTable.R_squared = new Array();
 for(i = 0; i < fslices.size(); i++){
  Fs=getFs(fslices.get(i));
  Fmp=getFm(fslices.get(i));
  Fop = getF0p(fslices.get(i));
  Phi2 = (Fmp-Fs)/Fmp;
  NPQ = (Fm-Fmp)/Fm;
  qP = (Fmp - Fs) / (Fmp - Fop);
  qL = qP * (Fop / Fs);
  //println((measurementInterval*i)
+"\t"+Fs+"\t"+Fmp+"\t"+Fop+"\t"+Phi2+"\t"+NPQ+"\t"+qP+"\t"+qL);
  dataTable.time[i] = (measurementInterval*i);
  dataTable.Fs[i] = Fs;
  dataTable.Fmp[i] = Fmp;
  dataTable.Fop[i] = Fop;
  dataTable.Phi2[i] = Phi2;
  dataTable.NPQ[i] = NPQ;
  dataTable.qP[i] = qP;
  dataTable.qL[i] = qL;
 }
```

```
 var ecsTable = FileIO.readFileAsTable(file_ecs);
 var eslices  = ecsTable.slice(numPtsPerECS);

 // curve fit method
 var serializedECSdata = "";
 var formulaList = new Array();
 var numECS = 0;
 var i = 0;
 while(i < eslices.size()){
  var sliceArray = new Array();
  for(var q = 0; q < consecutiveECSaveraging && i < eslices.size(); q++){
  // if((i+q) < eslices.size()) {sliceArray.push(eslices.get(i+q));}
// old solution (rolling average)
   sliceArray.push(eslices.get(i)); // cluster averaging
   i++;
  }
  var table2D = averageTogether(sliceArray,4);
  // write averaged ECS data to file
  serializedECSdata += table2DtoString(table2D);
  var expfit = getECSformula(table2D,true);
  formulaList[numECS] = expfit;
  numECS++;
 }
 try{
  writeToFile(serializedECSdata,file_ecs+"_averaged.dat");
 }catch(ex){
  println("Failed to write processed data to file: "+ex);
 }
 // gather output
 //println("time (min.)\ttau\ty0\tA\ttotal error\tfit formula");
 for(i = 0; i < formulaList.length; i++){
  dataTable.time2[i] = (measurementInterval*i+3);
  dataTable.tau[i] = formulaList[i].C[2];
  dataTable.y0[i] = formulaList[i].C[0];
  dataTable.A[i] = formulaList[i].C[1];
  dataTable.gH[i] = 1.0 / dataTable.tau[i];
  dataTable.vH[i] = (dataTable.A[i] - dataTable.y0[i]) / dataTable.tau[i];
  dataTable.pmf[i] = dataTable.A[i] - dataTable.y0[i];
  dataTable.LEF[i] = PARintensity * dataTable.Phi2[i+1];
  dataTable.CEF[i] = dataTable.vH[i] / dataTable.LEF[i];
  dataTable.fitError[i] = formulaList[i].fitError;
  dataTable.fitFormula[i] = formulaList[i].toString();
  dataTable.R_squared[i] = formulaList[i].R_squared.toString();
 }
 return createMegaTable(dataTable);
}
/**
@param table2d an array of arrays (should be square), where the
first dimension is the column and the second dimension is the row
*/
function table2DtoString(table2d){
 var strContent = "";
 for(var r = 0; r < table2d[0].length; r++){
  var first = true;
  for(var c = 0; c < table2d.length; c++){
   if(first == false){
    strContent += "\t";
   }
   strContent += table2d[c][r];
   first = false;
  }
  strContent += "\n";
```

```
 }
 return strContent;
}

function createMegaTable(obj){
 var toStringContent = "";
 var squareTable = new Array();
 for(var varName in obj){
  squareTable.push(new Array());
 }
 var width = squareTable.length;
 var ii = 0;
 for(var varName in obj){
  for(var item in obj[varName]){
   squareTable[ii].push(obj[varName][item]);
  }
  ii++;
 }
 var numRows = 0;
 for(var c = 0; c < width; c++){
  if(squareTable[c].length > numRows){
   numRows = squareTable[c].length;
  }
 }

 var first = true;
 var header = "";
 for(var varName in obj){
  if(first == false){
   header = header + "\t";
  }
  header = header + varName;
  first = false;
 }
 toStringContent += header + "\n";

 for(var r = 0; r < numRows; r++){
  first = true;
  var rowText= "";
  for(var c = 0; c < width; c++){
   if(first == false){
    rowText = rowText + "\t";
   }

   if(squareTable[c][r] === undefined) {
    // add nothing (empty cell)
   } else {
    rowText = rowText + squareTable[c][r];
   }
   first = false;
  }
  toStringContent += rowText + "\n";
 }
 return toStringContent;
}

var processedFiles = new Array();
function processMeasurement(){
 if(artefactOffset == 0)getBlank();
 var dataFile = FileIO.askForFile("Get data file");
 if(dataFile == null) return false;
 var fileString = dataFile.toString();
 var dotIndex = fileString.lastIndexOf(".");
```

```
 var fileRoot = fileString.substring(0,dotIndex-4);
 var flrFile = fileRoot+"0001.dat";
 var ecsFile =  fileRoot+"0003.dat";
 println("Processing "+fileRoot);
 var output = calcNPQandECS(flrFile,ecsFile);
 println(output);
 var outFile = fileRoot+"processed.dat";
 println("writing processed data to '"+outFile+"'");
 writeToFile(output,outFile);
 processedFiles.push(outFile);
 return true;
}

function processFolder(folderPath){
 var dir = new File(folderPath.toString());
 println("Processing folder "+dir+"...");
 var fileList = dir.listFiles();
 var flrFiles = new Array();
 var ecsFiles = new Array();
 for(var k = 0; k < fileList.length; k++){
  var f = fileList[k];
  if(f.toString().endsWith("0001.dat")){
   flrFiles.push(f);
  }
  if(f.toString().endsWith("0003.dat")){
   ecsFiles.push(f);
  }
 }
 var numFiles = flrFiles.length;
 if(numFiles > ecsFiles.length){
  numFiles = ecsFiles.length;
 }
 var processedFiles = new Array();
 for(var k = 0; k < numFiles; k++){
  var flrFile = flrFiles[k].toString();
  var ecsFile = ecsFiles[k].toString();
  var fileRoot = flrFile.toString()
        .substring(0,flrFile.toString().lastIndexOf(".") -4);
  println("Processing "+fileRoot+"...");
  var output = calcNPQandECS(flrFile,ecsFile);
  var outFile = fileRoot+"processed.dat";
  println("writing processed data to '"+outFile+"' ...");
  writeToFile(output,outFile);
  processedFiles.push(outFile);
 }
 if(processedFiles.length > 1){
  println("Averaging data...");
  averageTogetherFiles(processedFiles);
 }
 println("Done");
}

function processSubFolders(superFolderPath){
 var sdir = new File(superFolderPath.toString());
 var sfileList = sdir.listFiles();
 for(var q = 0; q < sfileList.length; q++){
  if(sfileList[q].isDirectory() == true){
   processFolder(sfileList[q]);
  }
 }
}

function askForFolder(title){
```

```
 if(typeof variable !== 'undefined'){
  // already exists
 } else {
  fileChooser = new JFileChooser();
 }
 fileChooser.setDialogTitle(title);
 fileChooser.setFileSelectionMode(JFileChooser.DIRECTORIES_ONLY);

 var action = fileChooser.showOpenDialog(null);
 if(action != JFileChooser.CANCEL_OPTION && fileChooser.getSelectedFile() != null){
  return fileChooser.getSelectedFile().getPath();
 } else {
  return null;
 }
}

//artefactOffset = 0;
artefactOffset = 0.15052285341952223;
PARintensity = 490;

if(artefactOffset == 0)getBlank();
var dataFile = askForFolder("Get data folder");

processSubFolders(dataFile);
```

APPENDIX C

COPY OF THE ENVIRONMENTAL PHOTOBIOREACTOR (EPBR)

Algal Research 6 (2014) 242–249

Contents lists available at ScienceDirect

Algal Research

journal homepage: www.elsevier.com/locate/algal

The environmental photobioreactor (ePBR): An algal culturing platform for simulating dynamic natural environments

Ben F. Lucker [b,1], Christopher C. Hall [b,1], Robert Zegarac [b], David M. Kramer [a,b,*]

[a] Department of Biochemistry and Molecular Biology, S222 Plant Biology Building, Michigan State University, East Lansing, MI 48824-1312, USA
[b] DOE—Plant Research Laboratory, S222 Plant Biology Building, Michigan State University, East Lansing, MI 48824-1312, USA

ARTICLE INFO

Article history:
Received 13 October 2013
Received in revised form 27 November 2013
Accepted 20 December 2013
Available online 31 January 2014

Keywords:
Algae biomass
Photobioreactor
Algae pond depth
Environmental simulation

ABSTRACT

Algae in natural or production setting experience fluctuating environmental conditions including changes in light, temperature, CO_2 and nutrient availability, oxygen and mixing. In response, algae respond to environmental changes dynamically, adjusting light energy capture strategies, physiological processes and cell cycle control. It is thus the combination of environmental conditions and biological responses that determines the performance of the algae. In contrast, much algal research is performed under artificially static laboratory environments, where different constraints determine performance. Consequently, algal strains selected for mass production in the laboratory may fail to perform well or outcompete local algal strains under outdoor production conditions. To address these issues, we have developed a novel environmental photobioreactor (ePBR), designed to mimic lighting from natural pond environments while controlling key environmental parameters including temperature, pH and CO_2 levels, mixing, and culture density. Natural lighting is simulated by illuminating from the top of a columnar culture vessel with a single high power white LED. This combination of lighting and geometry provides light intensities up to full sunlight at the culture surface, with light attenuation through the culture column similar to that observed in raceways or high rate algal ponds. Environmental parameters can be imposed in complex sequences with high time resolution via a user-programmable scripting language. Multiple ePBR units can be networked to perform parallel experiments, enabling semi-high throughput operations. In this report, we demonstrate the utility of this system by showing that fluctuating environmental conditions in ePBR significantly impact algal growth.

1. Introduction

The industrial use of microalgae for production of biofuels, high value products, and bioremediation (reviewed extensively in [1–3]), requires algal strains that can sustain efficient and robust photosynthesis while coping with large fluctuations in light intensity and quality, temperature, dissolved oxygen and CO_2 concentrations, pH, evaporation, dilution rates, and competition from adventitious algal species [4–6]. Because of the cost and difficulty of algal research in actual outdoor production settings, algal biomass research has relied heavily on computer models of algal growth. These models are generally based on algal growth data that is acquired from laboratory experiments, or performance in photobioreactors not designed to simulate environmental conditions, or limited outdoor data sets (discussed in Bernard [7]).

In contrast to the fluctuating conditions algae experience in outdoor environments, much of algal research has been conducted under artificially static or unrepresentative environmental conditions [8], e.g. in shaken or sparged Erlenmeyer flasks or custom photobioreactors (PBRs) [5,9–11]. These simplified laboratory conditions are useful for controlling 'reductionist' experiments, but do not capture environmental factors such as light and temperature that can synergistically impact algal growth and productivity. These effects differ between algal species [12,13]. Therefore experiments under these artificially controlled or static conditions likely miss important phenomena that are critical for understanding algal responses under real world conditions, possibly leading to selection of strains that perform well under conditions which are unrepresentative of outdoor ponds [14]. For example, the geometry of some PBRs (e.g. flat panel PBRs) minimize light gradients and maximize mixing, thus helping maximize light use efficiency and gas exchange rates. While such reactors are useful for determining maximal quantum efficiency of a strain, they do not simulate lighting, mixing, and temperature fluctuations required for determining productivity in an outdoor production pond.

To reproducibly assess the impacts of these variables on algal productivity, we have developed the environmental photobioreactor (ePBR), designed to replicate the environmental conditions in algal production ponds and natural systems that impact algal physiology, energy capture, and life cycle. The ePBR is sufficiently small and inexpensive for relatively

* Corresponding author at: Department of Biochemistry and Molecular Biology, S222 Plant Biology Building, Michigan State University, East Lansing, MI 48824-1312, USA. Tel.: +1 517 432 0072.
E-mail address: Kramerd8@msu.edu (D.M. Kramer).
[1] These authors had equal contribution to this work.

2211-9264/$ – see front matter © 2014 Elsevier B.V. All rights reserved.
http://dx.doi.org/10.1016/j.algal.2013.12.007

Figure 50: The environmental photobioreactor (ePBR): An algal culturing platform for simulating dynamic natural environments. *Published in 2014 in the journal Algal Research volume 6, Part B, pp. 242-249*

Figure 50 (cont'd)

high throughput analysis of multiple algae strains under a matrix of conditions yet provide a growth environment that is sufficiently representative of production conditions.

2. Methods

2.1. Strains, media, and basic culture conditions

Chlorella sorokiniana (UTEX 1230, from the UTEX Culture Consortium) was cultured in modified basal media (2NBH, [15]), consisting of Bristol Medium [16] with Hutner's trace elements [17] and doubled sodium nitrate concentration. *Chlamydomonas reinhardtii* strain cc125 (Chlamy Culture Collection, Duke University) was cultured in High Salt (HS) minimal media [18]. Prior to inoculation into the ePBR reactors, all strains were cultured to log phase growth in 125 mL Erlenmeyer flasks bubbled with ambient air at approximately volume of gas to volume of liquid ratios, under 120 μmol photon m^{-2} s^{-1} photosynthetically active radiation (PAR) provided by (Phillips F32T8/TL741 plus cool white) fluorescent lights with a 14:10 light:dark cycle.

2.2. Culturing conditions for environmental effects on C. reinhardtii

Flask-grown *C. reinhardtii* cultures used for comparison with cultures grown in ePBRs during weather simulations were grown in HS in Erlenmeyer flasks as described above in Section 2.1 but at 50 μmol photon m^{-2} s^{-1} PAR. The dataset for ePBR weather simulation was collected from the Mesonet weather archives for Altus, Oklahoma [19] from the month of July, 2005. The dataset included solar energy, air and soil temperature, wind speed, and humidity at 5 min measurement intervals. The solar energy measurements were converted from W m^{-2} to μmol photons m^{-2} s^{-1} using the average photon energy for PAR (2.17 μmol photons s^{-1} PAR per W solar radiation). The weather data was applied to a shallow pond water temperature model (kindly provided by Quentin Bèchet and Benoit Guieysse of Massey University) and described in [20], which provided temperature values representing a theoretical 15 cm deep raceway pond. The ePBRs were programmed by script files to follow the environmental and simulation data with linear interpolation to update environment parameters every minute. Log phase cells were used to inoculate the ePBR at a final concentration of 1×10^5 cells per mL in HS media and cultures were sparged with air enriched to 5% CO_2 at 0.37 L min^{-1} for 2 min every hour. Gas was dispersed through a 5 mm outer diameter glass dispersion stone (Ace glass, 9435-09) suspended through the ePBR cap. Stirring was set at a constant rate of 200 RPM using a 28.6 mm by 8 mm Teflon coated stir bar.

2.3. Conditions for ePBR column depth and biomass density matrix

C. sorokiniana ePBR cultures were inoculated from a log phase flask culture at a final concentration of 1×10^6 cells per mL and grown under a 14:10 light dark cycle with a sinusoidal approximation of daily light intensity with a peak of 2000 μmol photons m^{-2} s^{-1} PAR at midday. The ePBRs were injected with air enriched with 5% CO_2 for 2 min per hour at a flow rate of 0.37 L/min. Temperature and stirring were constant at a constant 28 °C and 200 RPM, respectively.

2.4. Cell counts and ash-free dry weight

Cell counts were taken using a cell counter (Z2 Coulter Counter, Beckman-Coulter). For experiments with daily cell count measurements, counts were taken at approximately the same time of the day (±1 h). For ash-free dry weight (AFDW) measurements, cells were harvested onto Whatman GF/F glass filters. The algal biomass and filter was dried at 104 °C overnight and weighed prior to and after incineration in a muffler oven at 550 °C for an hour. AFDW was calculated as dry biomass and filter minus the incinerated filter and ash.

2.5. Culture vessel

The culture vessel was designed to allow simulation of pond depths from 5 to 25 cm, with a total height of 27 cm in height and is molded from a transparent, autoclavable polycarbonate (Fig. 1A). The sides are slightly tapered at 4° to allow rapid assembly and firm (but reversible) seating within the temperature control jacket. The vessel can be machined to add or modify ports for gas, media exchange, or sample extraction. The vessel is sealed with a cap constructed of opaque, autoclavable polycarbonate with a glass illumination port and smaller apertures for pH, temperature and oxygen probes.

2.6. Lighting design

Illumination in the ePBR is provided by a white high power LED (Seoul P7 LED, part number W724C0CSV) capable of PAR intensities at the culture surface exceeding 2500 μmol photons m^{-2} s^{-1} PAR. The light is collimated through a molded plastic optical component which provides 8° cone of illumination. The LED, optic, optical collar, and LED heat sink make up the optical assembly (Fig. 1A). The entire assembly provides culture lighting through the optical window in the vessel cap, which is removable to facilitate quick exchange of the culture vessel and if required, access inside the culture vessel by removing the optical window. Condensation build up on the interior of the optical window is prevented by heating elements integrated into the optical collar which maintains the glass temperature above that of the vessel.

2.7. Temperature control

The ePBR culture temperature is controlled by solid-state Peltier-effect thermoelectric elements integrated into each half of the temperature control jacket (TCJ). The TCJ was assembled in two identical half jackets, machined from aluminum stock, with a 2° taper on each side (4° final) and mounted on an aluminum base plate. The taper was a design element to provide increased thermal contact with the culture vessel. The half jackets do not completely surround the culture vessel forming two ~25 mm slits on opposite sides of the TCJ to allow visual inspection of the culture, tubing connections, and spectroscopic measurements. The TCJ enables real time control of culture temperatures from ~15 °C below ambient room temperature to ~45 °C.

2.8. Optical density measurements

The culture density was measured using a pulsed infrared light-emitting diode (940 nm LED) and an infrared-sensitive photodiode, filtered to block visible light and mounted to the TCJ at 20 mm from the bottom of the vessel above the stir bar. The optical path-length was 50 mm. The current from the photodiode is electronically filtered to specifically amplify the LED pulse frequency while eliminating interference from stray light. Measurements were typically collected at 30 s intervals and 10 min rolling averages were calculated to minimize interference from stirring or gas bubbles. Optical density (OD) is estimated by calculating the negative logarithm of fractional transmission. To increase dynamic range of density estimations, paired measurements were taken at two LED intensity settings (low and high); the most sensitive, non-saturating, of these two measurements was selected by the control software. Corrected OD values were generated by normalizing both high and low intensity measurements to the baseline (or I_0) measurements that were obtained immediately after inoculation.

2.9. Software

The control software for the ePBRs with graphical user interface was written in the Java programming language. This software communicates with the ePBRs via standard off-the-shelf Ethernet

Figure 50 (cont'd)

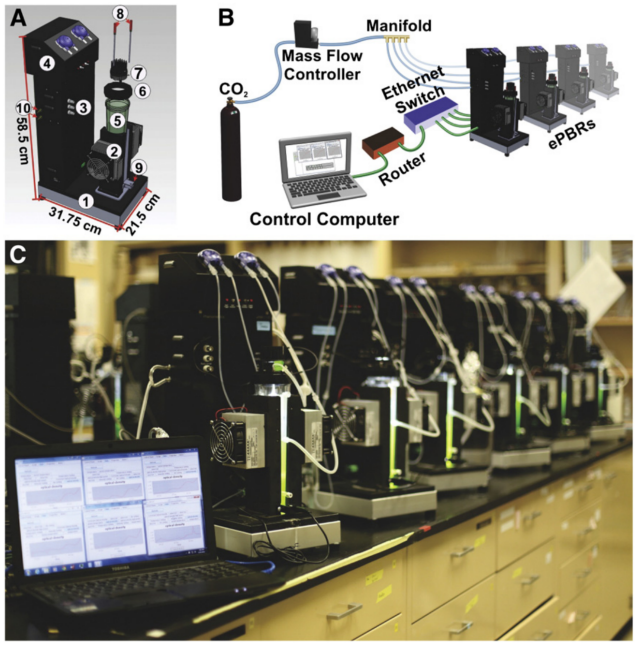

Fig. 1. The ePBR matrix as a modular photobioreactor system. A) Exploded schematic of an ePBR with: 1, base; 2, insulated aluminum temperature control jacket with Peltier thermoelectric temperature control elements; 3, housing for electronics, probe jacks solenoid valves for gas control, and ethernet jack; 4, Turbidostat pump unit; 5, autoclavable culture vessel; 6, autoclavable cap with glass window and holes for inserted probes; 7, optical assembly with high-power white LED with collimating optics; 8, temperature and pH probes thread through the cap; 9, mounted optical density probe; 10, hose barbs for gas inlet. B) Multiple ePBR modules can be networked together and operated in parallel using a central computer and use a gas timeshare system. C) A picture of an operational ePBR matrix.

networking equipment. An internal scripting language allowed programming of arbitrary or sinusoidal changes in temperature and light intensity, stirring, sparging and data collection from built in or accessory sensors.

2.10. pH and temperature probes

Probes for measuring temperature and pH were custom products for the ePBR manufactured by Microelectrodes, Inc. Bedford, New Hampshire (currently available from Phenometrics, Inc., East Lansing, MI).

2.11. Turbidostat control

For turbidostat control, ePBRs were connected to a pair of peristaltic pumps—one for injecting media and the other for removing it—controlled from the ePBR. Culture depth was determined by

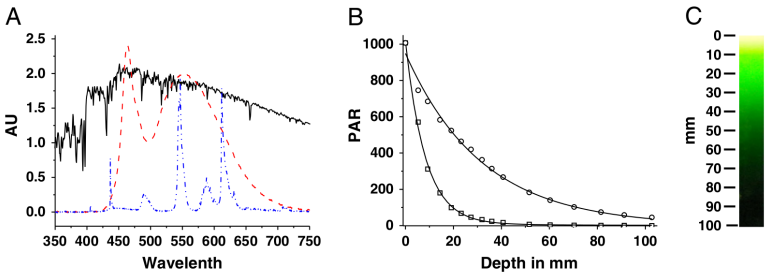

Fig. 2. Comparisons of solar, fluorescent tube and ePBR LED spectral distributions. A) Solar spectrum between 350 and 750 nm at ground level (solid black line), spectrum of the Seoul P7 LED used in the ePBR (red dashed line), and the spectrum of a Phillips F32T8/TL741 plus cool white fluorescent lights (blue dot-dashed line). B) Light intensity in μmol photons m^{-2} s^{-1} PAR as a function of depth in a *C. sorokiniana* culture at both 18 μg/mL of chlorophyll (open squares) and 3.4 μg/mL (open circles). The lines are first order decay fits to the measured PAR intensities. C) A representative cutout of a picture of an ePBR vessel with a dense *C. sorokiniana* culture at 2000 μmol photons m^{-2} s^{-1} PAR.

Figure 50 (cont'd)

placement of the removal port. Pump triggering was determined by preset optical density thresholds set in control software.

3. Results

3.1. ePBR culture lighting

The spectral output of the collimated ePBR LED, measured at the surface of a culture, was compared with that from sunlight, and fluorescent tube (Phillips F32T8/TL741 plus cool white fluorescent lights) (Fig. 2A). The LED provided a broader distribution of wavelengths in the PAR region than the fluorescent tube, but was still deficient in near UV, near infrared components and in the green region between 475 nm and 525 nm. The LED housing can accommodate supplemental LEDs to enhance output in these regions. Fig. 2B shows that the LED in combination with an 8° collimating optic resulted in light penetration through the algae culture closely mimicking the penetration of sunlight through an algal pond [21]. The light attenuation through the algae culture approximated a first order decay under both high and low chlorophyll concentrations, 18 μg/mL and 3.4 μg/mL, respectively. The LED light intensity can be controlled precisely at the full range of possible solar intensities and is discussed in further detail in Section 3.5.

3.2. Optical density measurements

Optical density (OD) measurements based on light scattering were good indicators of overall culture growth. When grown under a diurnal cycle, increasing optical density measurements were seen only during daylight hours, with small decreases in OD during dark hours (Fig. 3A), consistent with observations made by Vítová et al. [22]. An aggregate plot of changes in OD measurements versus changes in AFDW from inoculum values (15 mg L^{-1} AFDW) is shown in Fig. 3B; each data point was measured at different times in seven independent experiments. Different ePBR units were used for each experiment. For intra-experimental data points, the R values ranged from 0.877 to 0.978 and the average was 0.938 with a standard deviation of ±0.0426, while the aggregate plot of all these experiments had an R value of 0.926 with a standard deviation of ±0.16, indicating higher intra-experimental correlations than between reactors. Normalized turbidity measurements gave a linear approximation of culture biomass density as measured by AFDW. However, when data from different algal species were combined (Fig. 3B), the R value decreased to 0.85. However, intra-species correlations between OD and AFDW were much higher (data not shown). These results are not surprising considering the well-established dependence of light scattering on species [23] and indicate that calibration of OD measurements to AFDW between different species will increase accuracy.

3.3. Controlling cell density

The ePBR can control cell density in multiple ways. In turbidostat mode, algal cultures were diluted by a certain volume of culture medium (typically 5 mL) when the OD exceeded a predetermined limit. In chemostat mode, the culture was diluted at regular intervals by defined amounts, resulting in a constant dilution rate. Shown in Fig. 4A (black line), the ePBR was used in turbidostat mode under a diurnal cycle with a target OD of 0.675; when the culture OD surpassed the OD target, an aliquot of 5 mL of fresh media was added. Decreasing OD measurements as seen here were due to decreasing light scattering properties over course of the night because of changes in cell size and cellular content [22].

In chemostat mode under constant light of 400 μmol photons m^{-2} s^{-1} PAR, the dilution rate was fixed to replace 15% and 35% of the total culture volume daily. After two days, the cultures reached a steady state where the net growth rate was equal to the rate of dilution and as expected, the biomass productivity of the culture with 35% dilution rates was higher than that of the culture with 15% dilution rates, at 17.0 versus 11.9 g of AFDW m^{-2} d^{-1}, respectively. Both turbidostat and chemostat modes resulted in consistent algal growth for between 5 and 7 days.

Algal macronutrient uptake can alter culture pH through generation of H^+ or OH^- ions. A common strategy to control culture pH is through injection of CO_2 to reduce the pH to a desired set point. Over the course of four days, the culture pH was maintained between pH 6.8 and 7.2 (Fig. 4B). Because the ePBR is mechanically stirred, sparging was not required to mix the culture and the acidifying sparges could therefore be brief and infrequent (approximately 120 s every 60 min), analogous to a raceway-style pond where carbon dioxide enriched air is injected at a single point in the pond's circulation path (data not shown).

3.4. The ePBR can reproduce dynamic environmental conditions of production

To test the ability of ePBR to simulate dynamic environments experienced by algae during outdoor production, we programmed the ePBRs with archived environmental data with 5 min resolution. The weather data was from Altus, Oklahoma collected over a period of seven days in July of 2005. Water temperature was predicted from weather data using the model described in Section 2.2 [20]. Water temperature fluctuated between 20 °C and 40 °C, while associated solar energy data was from both partly-cloudy and sunny days, with a maximum light solar intensity of 2355 μmol photons m^{-2} s^{-1} PAR. Over a large range of conditions, the programmed and measured values tightly overlapped, indicating that the ePBR can accurately "playback" solar irradiance (Fig. 5A) and water temperature (Fig. 5B). The accuracy and

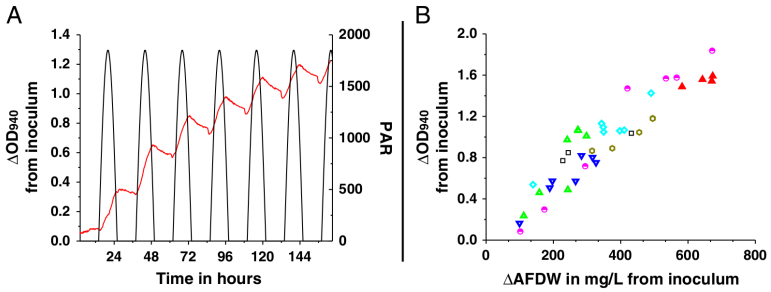

Fig. 3. Optical density (turbidity) measurements of culture growth and biomass density of *C. sorokiniana*. A) Measured optical density (red line) increases during daylight hours when cells were grown under a diurnal cycle (black line, incident light in μmol photons m^{-2} s^{-1} PAR. B) An aggregate plot of changes in optical density and versus ash free dry weight from inoculum values, each set of data points (open hexagons, open squares, open upward triangle, open diamond, half-filled circles, open downward pointed triangle, closed triangles) represents individual ePBR cultures where multiple samples were collected.

Figure 50 (cont'd)

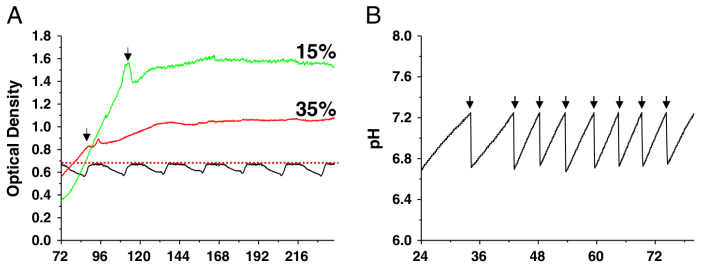

Fig. 4. The ePBR under static operations. A) Online optical density measurements combined with triggered pumps controlled culture densities, or monitor steady state chemostat growth of *C. sorokiniana*. Cultures were maintained in a light dark cycle at an upper OD threshold of 0.675. The dotted red line indicates the preset OD threshold and the solid black line show OD measurements. Cells grown under constant light and diluted continuously at 15% and 35% per day, green and red lines respectively. Arrows denote start of constant dilution. B) Culture pH was maintained between an upper and a lower threshold by programming the ePBRs to sparge 5% CO_2 in air, punctuated by arrows.

reproducibility of parameter control are readily observed in the linear dependencies of measured and programmed values shown in Fig. 5C and D.

3.5. Growth under dynamic conditions effects overall growth rate

To determine the effects of dynamic environments on algal growth, we compared the growth of *C. reinhardtii* in bubbled laboratory Erlenmeyer flasks (bubble flasks), in the ePBR under either 'dynamic' (naturally fluctuating) and 'static' (averaged) conditions. The light and temperature conditions for these experiments are illustrated in Fig. 6A and B. For dynamic conditions, the ePBR units were programmed with Altus weather data used in the experiments described in Fig. 5, which had a day:night cycle of 14:10 h. For static conditions, the averaged integrated PAR and water temperature for all data used under the dynamic conditions was applied equally in a square wave across all days (1315 μmol photons m^{-2} s^{-1}), with a day:night cycle of 12:12 h, and constant temperature of 28 °C. Bubble flasks were illuminated from above using fluorescent lighting with a 14:12 hour day/night cycle and PAR of about 50 μmol photons m^{-2} s^{-1}. Each experiment was conducted in triplicate.

During the initial 1–3 days of the experiment cultures grown under static and dynamic conditions grew equally well, doubling about 1.5 times per day (Fig. 6C). However, significant differences emerged between dynamic and static conditions during transition from logarithmic to stationary phase in days 3 to 7; the growth under dynamic conditions was significantly reduced (0.08 divisions per day versus 0.28) and varied significantly with time. The doubling time in the bubble flasks was about twice that seen in the ePBRs.

3.6. Culture depth dependence of growth rates

A key feature of the ePBR is that it can simulate the light penetration through algal cultures, as it has been observed in production settings (Fig. 2B; [21]). To test the effects of light penetration on algal growth we characterized the growth of *C. sorokiniana* in a matrix of column height and biomass concentrations (Fig. 7). The cultures were grown at depths of 10, 15 and 20 cm and at each depth we maintained biomass concentrations of ~25, 150, and 500 mg/L of AFDW. Growth under each condition was tested in triplicate and cultures were maintained at target densities for a minimum of three consecutive days. Daily biomass productivity values were calculated from the amount of culture biomass displaced each day with fresh culture by the turbidostat to maintain a constant culture biomass density.

At biomass concentrations of 25 and 150 mg/L^{-1}, biomass productivity was highest in the tallest (20 cm) columns at 19.7 g AFDW m^{-2} day^{-1} (72.2 metric ton ha^{-1} $year^{-1}$) and 19.1 g AFDW m^{-2} day^{-1} (69.7 metric ton ha^{-1} $year^{-1}$), respectively, followed in productivity by 15 and 10 cm cultures. In contrast the maximal and minimum productivities of ~21.4 g AFDW m^{-2} day^{-1} (78.1 metric ton ha^{-1} $year^{-1}$) and 4.31 g AFDW m^{-2} day^{-1} (15.7 metric ton ha^{-1} $year^{-1}$) were achieved by the 10 cm depth culture at 500 mg L^{-1} and 25 mg L^{-1} biomass density, respectively. There was slightly higher biomass productivity in the 20 cm

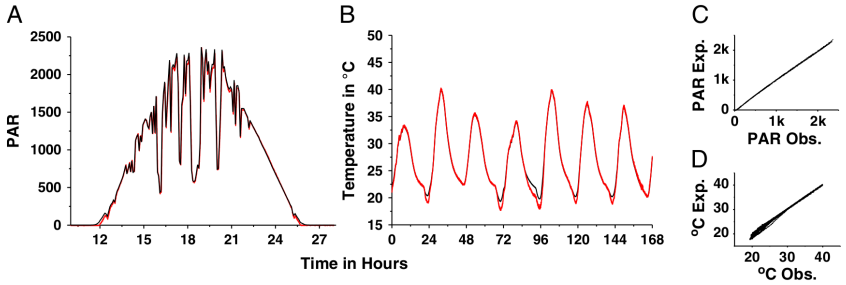

Fig. 5. Dynamic control of lighting and temperature conditions. A) Incident light intensity was programed into the ePBR using field measurements as described in Section 2.2 (black line) and light intensity output was recorded using a LiCOR PAR sensor connected to a data logger (red line). B) Water temperature predicted from modeling (Sec. **2.1**) was programed into the ePBR (black line) and observed culture temperatures were recorded over seven days while running the program (black line). C) Observed versus expected light intensity reading from the experiment in panel A, in μmol photons m^{-2} s^{-1} PAR. D) Scatter plot of the measured water temperature versus water temperature profile programed into the ePBR from the experiment in panel B.

Figure 50 (cont'd)

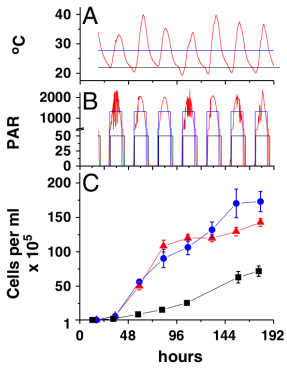

Fig. 6. Effects of dynamic temperature and light regimes affect *C. reinhardtii* growth rates. A) The dynamic temperature regime acquired from the predictive water temperature model described in Section 2.2 (red line), the averaged temperature used for static conditions (blue line) in the ePBR cultures and room temperature of the bubble flasks (black). B) light intensities in μmol photons m^{-2} s^{-1} of PAR for the dynamic conditions (red line), static conditions (blue line), and the light regime of the flask cultures which was 50 μmol photons m^{-2} s^{-1} PAR (black line), note the split y axis to allow representation of flask culture conditions. C) Cell density of cultures grown under the dynamic conditions (red line), static conditions (blue line), and bubble flasks (black line). Error bars represent standard deviation from three independent biological replicates.

than in the 15 cm column height at high biomass concentration. Interestingly, the percentage of biomass attributed to chlorophyll increased from ~1% in the low biomass cultures to 2.5% in the high biomass cultures (Fig. 6, open circles). In the low biomass cultures, there was higher incident light per unit biomass, leading to less self-shading and lower light attenuation through the column depth.

4. Discussion

4.1. Design objectives

The primary design objective of the ePBR system was to develop a research photobioreactor capable of 1) simulating an outdoor algal pond environment without hindering versatility; and 2) operating at medium high throughput (in an array of dozens of units). We met these objectives and describe the performance of the ePBR under selected conditions, illustrating its ability to control light intensities (Fig. 5A), temperatures (Fig. 5B), CO_2 and pH (Fig. 4B), cell density (Fig. 4A), measuring growth by turbidity (Fig. 3A), and network compatible enabling parallel experiments (Fig. 1B, C).

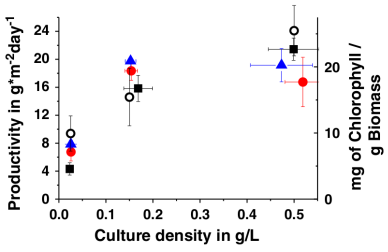

Fig. 7. Biomass productivity as a function of biomass density and culture depth. *C. sorokiniana* was cultured under 14:10 hour light dark cycle and sinusoidal light regime reaching the zenith of 2000 μmol photons m^{-2} s^{-1} PAR at midday and a constant 28 °C. Cultures depths were 10 cm (black squares), 15 cm (red circles), and 20 cm column heights (blue triangles). Each depth was maintained at ~25, 150, and 500 mg/L biomass densities under turbidostat model as described in Sec. 3.3 (right y-axis). All data points represent a minimum of three biological replicates maintained for a minimum of three consecutive days. The right y-axis shows the amount of chlorophyll in mg for every g of biomass is displayed for each biomass density (open circles).

4.2. Overall culture depth affects algal biomass production rates

Under optimized culture de7pths and biomass concentrations daily biomass yield of *C. sorokiniana* was 21.4 g AFDW m^{-2} day^{-1}, Fig. 7. Using the average biomass energy densities for *C. sorokini*ana reported in literature of 21.95 KJ g^{-1} dry weight [24,25] we estimated total light energy conversion to biomass of 7.3% (PAR), 3.43% (predicted total solar energy) assuming PAR is 47% of available solar energy. This is lower than light energy capture and conversion to biomass percentages for the same strain, 4.8% (total solar) in outdoor tubular photobioreactors by Bechet et al. [26] and 8.67% (PAR) in a helical photobioreactor Morita et al. [27]. These values are well within reported ranges of outdoor algal biomass productivity rates in outdoor ponds [4,8]. It is important to note that this production only optimized for column height, not temperatures, media composition or pH. It has been reported that this strain can reach optimum growth temperatures between 34 °C and 38 °C [28,29], significantly higher than temperatures used here.

In high rate algal ponds, culture depth affects light penetration and thus algal light use efficiency [12,30–32] and productivity [4,33,34]. Our column depth experiments (Fig. 7) show that algae decrease chlorophyll content with increased incident light availability, confirming earlier results by Bonente et al. [34]. They also show that growth rate is influenced by a combination of pond depth and biomass density, consistent with observations and models by Richie and Larkum [35], and Sukenik et al. [30], who predicted optimum pond depths of ~9 cm and 20 cm, respectively. These model predictions and our observations are in contrast to recent models put forth by Slegers et al. [36], who predicted that pond depths up to 50 cm at low biomass densities are optimal for maximizing total biomass yield. Moheimani and Borowitzka [37] reported that productivity in their open raceway ponds was indeed influenced by pond depth, but optimum depth for productivity depended on the season and weather and suggests that the light sensitivity of *Pleurochrysis carterae* was affected by seasonal temperature variation. These past results, and those reported here, highlight the need to optimize culture depth and biomass density under seasonal temperature variations prior to expensive field trials. We conclude that the ePBR can be used as an effective laboratory tool for this optimization process.

4.3. The ePBR can simulate dynamic environments

Combining the programmable lighting and temperature controls enables the ePBR to "playback" recorded weather data. Here we were able to combine archived environmental data with sophisticated pond temperature models to recreate key dynamic aspects of environments that algae may experience under production conditions. We found that growth differed substantially between simulated dynamic and static (averaged) conditions (Fig. 6), implying that dynamic changes in conditions are critical for assessing productivity and robustness of algal strains in particular environments.

The ePBR recreates spatial and temporal gradients of light that can occur in production algae environments by using a high power LED combined with a low angle collimating optic at the top of the culturing column (Fig. 1A). Light intensities in the field can vary rapidly by orders of magnitude over the seconds time scale because of cloud cover, wave lensing, and culture mixing [19,38]. These fluctuations can lead to rapid cycling between high light-driven photoinhibition of photosystem II (e.g. at the pond surface) and light-limitations (e.g. at the bottom of the column) [30,39–41]. In contrast, common fluorescent bulbs used

Figure 50 (cont'd)

for algal culturing provide continuous diffuse, low intensity (non-saturating) light with little spectral resemblance to natural light. Therefore, culture flasks illuminated via fluorescent lights likely do not provide the light gradient through the culture that algae experience in natural pond conditions.

Over the course of our experiments, flask cultures received roughly 4% of the available energy for cellular growth, however had growth rates ~50% of cultures exposed to simulated sunlight through water columns in ePBRs (Fig. 6). This difference translates into an approximately 13-fold higher ratio of growth to integrated irradiance for laboratory flasks compared to ePBR. The disparity between observed energy requirements for growth in the flasks and ePBR can be largely attributed to the intensity and distribution of light through the culture vessels. Photosynthesis is highly efficient at low light but is saturated at the irradiances increase above saturation [42]. The flask cultures received light far below saturation for *C. reinhardtii*, leading to high light use efficiency [43,44]. In contrast, the ePBR cultures received higher intensity light that is distributed with a steep gradient through the culture column (Fig. 2B, C). The upper surface of the dynamic ePBR cultures received light reaching full sunlight at midday, up to 2355 μmol photons m^{-2} s^{-1} and the static cultures received 1315 μmol photons m^{-2} s^{-1}, both of these conditions exceeds the light capacity of photosynthesis, leading to dissipation of energy by nonphotochemical processes [42–45]. The steep light gradient (Fig. 2B, C) also leads to light limitation of photosynthesis in cells near the bottom of the column. Because light saturation and penetration are strongly dependent on the antenna composition and metabolic capacity of algae [8], future efforts to improve algae would benefit greatly by estimates of field performance from more realistic culture conditions, like those provided by ePBR.

5. Conclusion

We have demonstrated the utility of the ePBR system as a tool to accelerate algal biomass research. The ePBR provides a scalable platform that mimics key environmental conditions found in natural or production settings that are important for determining the efficiency and productivity of photosynthesis. Controlling light and temperature improves reproducibility between cultures under the same conditions and the networking interface provides centralized control that facilitates running experiments and replicates in parallel. Dynamic control over culturing parameters makes it possible to examine how algae respond to changes in their environment and to replay target environments to measure strain performance in the expected field conditions.

Conflict of interest

The authors would like to disclose that the ePBR system is now a product sold by Phenometrics Inc. whom did not financially contribute to this work.

Acknowledgments

The authors thank Drs. Quentin Bèchet and Benoit Guieysse of Massey University for their assistance in modeling water temperature, and the participating members of the National Alliance for the Advancement of Biofuels and Bioproducts (NAABB) for their valuable input on the design of the ePBR. We would also like to thank Jeffery Cruz for the valuable discussions and Joel Carpenter for contributions to design efforts during initial prototyping. This work was a subcontract of the NAABB consortium and funded by U.S. Department of Energy Office of Biomass Program grant DE-EE0003046.

References

[1] O. Pulz, W. Gross, Valuable products from biotechnology of microalgae, Appl. Microbiol. Biotechnol. 65 (2004) 635–648.
[2] S.A. Scott, M.P. Davey, J.S. Dennis, I. Horst, C.J. Howe, D.J. Lea-Smith, et al., Biodiesel from algae: challenges and prospects, Curr. Opin. Biotechnol. 21 (2010) 277–286.
[3] J. Milledge, Commercial application of microalgae other than as biofuels: a brief review, Rev. Environ. Sci. Biotechnol. 10 (2011) 31–41.
[4] J.C. Weissmen, R.P. Goebel, Design and Analysis of Microalgal Open Pond Systems for the Purpose of Producing Fuels, National Technical Information Service, U.S. Department of Commerce, Springfield, VA, 1987.
[5] M. Morweiser, O. Kruse, B. Hankamer, C. Posten, Developments and perspectives of photobioreactors for biofuel production, Appl. Microbiol. Biotechnol. 87 (2010) 1291–1301.
[6] J.J. Bull, S. Collins, Algae for biofuel: will the evolution of weeds limit the enterprise? Evolution 66 (2012) 2983–2987.
[7] O. Bernard, Hurdles and challenges for modelling and control of microalgae for CO_2 mitigation and biofuel production, J. Process Control 21 (2011) 1378–1389.
[8] J. Sheehan, A look back at the U. S. Department of Energy' s Aquatic Species Program: biodiesel from algae, Renew. Energy 328 (1998) 1–328.
[9] B. Wang, C.Q. Lan, M. Horsman, Closed photobioreactors for production of microalgal biomasses, Biotechnol. Adv. 30 (2012) 904–912.
[10] F. Lehr, C. Posten, Closed photo-bioreactors as tools for biofuel production, Curr. Opin. Biotechnol. 20 (2009) 280–285.
[11] C.U. Ugwu, H. Aoyagi, H. Uchiyama, Influence of irradiance, dissolved oxygen concentration, and temperature on the growth of *Chlorella sorokiniana*, Photosynthetica 45 (2007) 309–311.
[12] J.E.F. Huisman, R.R. Jonker, C.O.R. Zonneveld, F.J. Weissing, Competition for light between phytoplankton species: experimental tests of mechanistic theory, Ecology 80 (1999) 211–222.
[13] J.F. Coles, R.C. Jones, Effect of temperature on photosynthesis-light response and growth of four phytoplankton species isolated from a tidal freshwater river, J. Phycol. 36 (2000) 7–16.
[14] M.J. Griffiths, S.T.L. Harrison, Lipid productivity as a key characteristic for choosing algal species for biodiesel production, J. Appl. Phycol. 21 (2009) 493–507.
[15] P.T. Davey, W.C. Hiscox, B.F. Lucker, J.V. O'Fallon, S. Chen, G.L. Helms, Rapid triacylglyceride detection and quantification in live micro-algal cultures via liquid state ^{1}H NMR, Algal Res. 1 (2012) 166–175.
[16] H.C. Bold, The morphology of *Chlamydomonas chlamydogama*, sp. nov. Bull. Torrey Bot. Club 76 (1949) 101.
[17] S.H. Hutner, L. Provosoli, A. Schatz, C.P. Haskins, Some approaches to the study of the role of metals in the metabolism of microorganisms, Proc. Am. Phil. Soc. 94 (1950) 152–170.
[18] N. Sueoka, Mitotic replication of deoxyribonucleic acid in *Chlamydomonas reinhardtii*, Proc. Natl. Acad. Sci. 46 (1960) 83–91.
[19] R.A. McPherson, C.A. Fiebrich, K.C. Crawford, J.R. Kilby, D.L. Grimsley, J.E. Martinez, et al., Statewide monitoring of the mesoscale environment: a technical update on the Oklahoma Mesonet, J. Atmos. Ocean. Technol. 24 (2007) 301–321.
[20] Q. Béchet, A. Shilton, J.B.K. Park, R.J. Craggs, B. Guieysse, Universal temperature model for shallow algal ponds provides improved accuracy, Environ. Sci. Technol. 45 (2011) 3702–3709.
[21] B.M.A. Kroon, H.A.M. Ketelaars, H.J. Fallowfield, L.R. Mur, Modelling microalgal productivity in a high rate algal pond based on wavelength dependent optical properties, J. Appl. Phycol. 1 (1989) 247–256.
[22] M. Vítová, K. Binová, M. Hlavová, S. Kawano, V. Zachleder, M. Cizkova, *Chlamydomonas reinhardtii*: duration of its cell cycle and phases at growth rates affected by temperature, Planta 234 (2011) 599–608.
[23] R.D. Vaillancourt, Light backscattering properties of marine phytoplankton: relationships to cell size, chemical composition and taxonomy, J. Plankton Res. 26 (2004) 191–212.
[24] A. Illman, A. Scragg, S. Shales, Increase in *Chlorella* strains calorific values when grown in low nitrogen medium, Enzyme Microb. Technol. 27 (2000) 631–635.
[25] R. Hase, H. Oikawa, C. Sasao, M. Morita, Y. Watanabe, Photosynthetic production of microalgal biomass in a raceway system under greenhouse conditions in Sendai city, J. Biosci. Bioeng. 89 (2000) 157–163.
[26] Q. Béchet, R. Muñoz, A. Shilton, B. Guieysse, Outdoor cultivation of temperature-tolerant *Chlorella sorokiniana* in a column photobioreactor under low power-input, Biotechnol. Bioeng. 110 (2013) 118–126.
[27] M. Morita, Y. Watanabe, H. Saiki, High photosynthetic productivity of green microalga *Chlorella sorokiniana*, Appl. Biochem. Biotechnol. 87 (2000) 203–218.
[28] C. Sorokin, Tabular comparative data for the low- and high-temperature strains of *Chlorella*, Nature 184 (1959) 613–614.
[29] D. Madamwar, R.B. Subramanian, L.E. de-Bashan, A. Trejo, V.A.R. Huss, J.-P. Hernandez, et al., *Chlorella sorokiniana* UTEX 2805, a heat and intense, sunlight-tolerant microalga with potential for removing ammonium from wastewater, Bioresour. Technol. 99 (2008) 4980–4989.
[30] A. Sukenik, R.S. Levy, Y. Levy, P.G. Falkowski, Z. Dubinsky, Optimizing algal biomass production in an outdoor pond: a simulation model, J. Appl. Phycol. 3 (1991) 191–201.
[31] J.L. Mendoza, M.R. Granados, I. de Godos, F.G. Acién, E. Molina, C. Banks, et al., Fluid-dynamic characterization of real-scale raceway reactors for microalgae production, Biomass Bioenergy 54 (2013) 267–275.
[32] P.G. Falkowski, Light-shade adaptation and assimilation numbers, J. Plankton Res. 3 (1981) 203–216.
[33] J.U. Grobbelaar, Modelling phytoplankton productivity in turbid waters with small euphotic to mixing depth ratios, J. Plankton Res. 12 (1990) 923–931.
[34] G. Bonente, S. Pippa, S. Castellano, R. Bassi, M. Ballottari, Acclimation of *Chlamydomonas reinhardtii* to different growth irradiances, J. Biol. Chem. 287 (2012) 5833–5847.
[35] R.J. Ritchie, A.W.D. Larkum, Modelling photosynthesis in shallow algal production ponds, Photosynthetica 50 (2012) 481–500.

Figure 50 (cont'd)

[36] P.M. Slegers, M.B. Lösing, R.H. Wijffels, G. van Straten, A.J.B. van Boxtel, Scenario evaluation of open pond microalgae production, Algal Res 2 (4) (2013) 358–368.
[37] N.R. Moheimani, M.A. Borowitzka, Limits to productivity of the alga *Pleurochrysis carterae* (haptophyta) grown in outdoor raceway ponds, Biotechnol. Bioeng. 96 (2007) 27–36.
[38] John C. Sager, J. Craig McFarlane, Radiation, in: R.W. Langhans, T.W. Tibbitts (Eds.), Plant Growth Chamb. Handb., NC-101 Regional Committee on Controlled Environment Technology and Use, Iowa State University, 1997, pp. 1–30.
[39] J. Myers, Growth characteristics of algae in relation to the problems of mass culture, Algal Cult. from Lab. to Pilot Plant. Carnegie Inst. Wash. Publ. 600 (1953) 37–54.
[40] M.A. Borowitzka, Commercial production of microalgae: ponds, tanks, tubes and fermenters, J. Biotechnol. 70 (1999) 313–321.
[41] D.R. Ort, A. Melis, Optimizing antenna size to maximize photosynthetic efficiency, Plant Physiol. 155 (2011) 79–85.
[42] R.E. Blankenship, D.M. Tiede, J. Barber, G.W. Brudvig, G. Fleming, M. Ghirardi, et al., Comparing photosynthetic and photovoltaic efficiencies and recognizing the potential for improvement, Science 332 (2011) 805–809.
[43] C. Sorokin, R.W. Krauss, The effects of light intensity on the growth rates of green algae, Plant Physiol. 33 (1958) 109–113.
[44] S. Falk, G. Samuelsson, Recovery of photosynthesis and photosystem II fluorescence in *Chlamydomonas reinhardtii* after exposure to three levels of high light, Physiol. Plant. 85 (1992) 61–68.
[45] C. Vejrazka, M. Janssen, G. Benvenuti, M. Streefland, R.H. Wijffels, Photosynthetic efficiency and oxygen evolution of *Chlamydomonas reinhardtii* under continuous and flashing light, Appl. Microbiol. Biotechnol. 97 (2013) 1523–1532.

APPENDIX D

DERIVATION OF SINUSOIDAL DAY APPROXIMATION

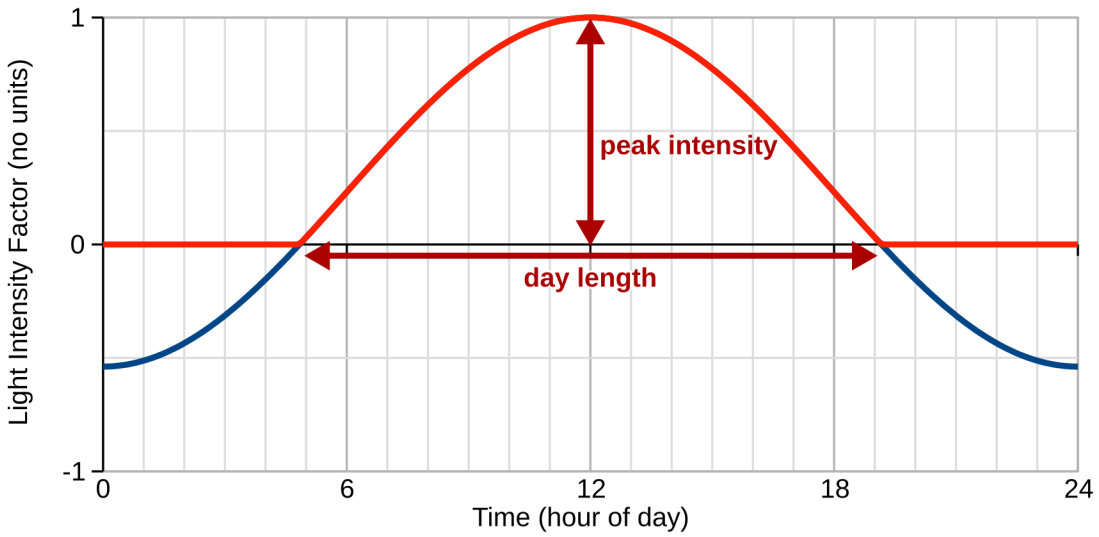

Figure 51: Derivation of sinusoidal day approximation. *The algorithm was derived by defining a sine wave that is offset such that the time between its crossing of the X-axis is equal to the specified day length, and then normalized to the peak value occurring at noon.*

The equations used to generate the sinusoidal day are as follows:

Eq. 20: $$I = I_{max} \times A \times \sin\left(hr \times \frac{\pi}{12} - \frac{\pi}{2}\right) + C$$

Eq. 21: $$A = 1 - C$$

Eq. 22: $$C = \frac{J}{J - 1}$$

Eq. 23: $$J = \sin\left(\frac{\pi}{2} - (day\,length) \times \frac{\pi}{24}\right)$$

From Simulation.java:

```
public static double sinusoidalDayFactor(Number timeInHours, Number dayLength) {
  double PIover2 = Math.PI / 2;
  double time_in_radians = (timeInHours.doubleValue() / 24.0) * 2 * Math.PI;

  time_in_radians -= PIover2;// phase shift so midnight is the lowest point
  // get day length in radians
  double day_in_radians = 2 * Math.PI * dayLength.doubleValue() / 24;
  // here's the origin of the math:
  // intensity = Imax * A * sin(2 * PI * time / 24) + C
  // A = 1 - C
  // A * sin(x) + C = 0 when at sunrise and sunset
  // thus A * sin(x + day_length) + C = 0 iff  A * sin(x) + C = 0
  // x = arcsin(-C/A)
  // due to symmetry, half way through the day is noon: sin(x + day_length/2) = 1
  // thus x + day_length/2 = PI/2
  // arcsin(-C/A) = PI/2 - day_length/2
  // -C/A = sin(PI/2 - day_length/2)
  // -C/(1 - C) = sin(PI/2 - day_length/2)
  // let J = sin(PI/2 - day_length/2)
  // -C = (1 - C) * J
  // -C = J - C * J
  // C * J - C = J
  // C * (J - 1) = J
  // C = J / (J - 1)
  double J = Math.sin(PIover2 - day_in_radians / 2);
  double C = J / (J - 1);
  double A = 1 - C;
  double factor = A * Math.sin(time_in_radians) + C;
  if (factor < 0) {
   factor = 0;
  }
  return factor;
}
```

APPENDIX E

ALGALCOMMAND SCRIPT PROGRAMMING MANUAL

AlgalCommand Script Programming Manual

Contents

Introduction

AlgalCommand allows the user operate the ePBRs in non-standard modes of operation by creating JavaScript files that specify the desired behavior of the ePBR.

WARNING: It is possible for scripts to access the filesystem of the computer. Take extra care when loading scripts not written by you or a trusted source.

Figure 52: AlgalCommand script writing guide. *This documentation is provided to users of ePBRs who wish to write their own ePBR control scripts.*

Figure 52 (cont'd)

Event-Based Scripting

Scripts for the ePBRs are event-based, with functions in the script being called in response to events, such as timing events and data received events. The reason that the scripts are not linear is that a linear script would not easily be able to make decisions based on real-time data from the ePBR and that the ePBRs may generate data independently of the script (such as from clicking "Measure Now" in the manual controls tab). The event-based structure ensures that the script will always be able to intercept data, even if the trigger for that measurement was external to the script or the ePBR has lost connection at the time of the request for data and comes back online at a later time.

Taking a measurement in a script has two components. First, the appropriate measure function is called (such as `PBR.measureOD()`). Calling the measurement functions will send a command to the ePBR to take that measurement and send back the data at some time in the near future. Usually the data comes back to AlgalCommand within a second of asking for a measurement, but network traffic could introduce a delay. When the data comes back from the ePBR, the data is passed back to the script through one of the data event functions. If the ePBR is not online, the functions to ask for measurements will not fail (so the script will continue to run), but no data will return and thus the data event functions will not be triggered until the ePBR is back online.

All code in the script will be called in response to some event. For code that is not triggered by data or user interaction, use timers to generate timing events. Use `Timer.setTimer(X, Y)` to generate time events at a periodic interval of Y seconds and then place the repeating code in the `timeEvent(X)` function. The `timeEvent(X)` function's argument will be the number of the timer that was created.

The following figure shows all the events and corresponding functions for scripts.

Figure 52 (cont'd)

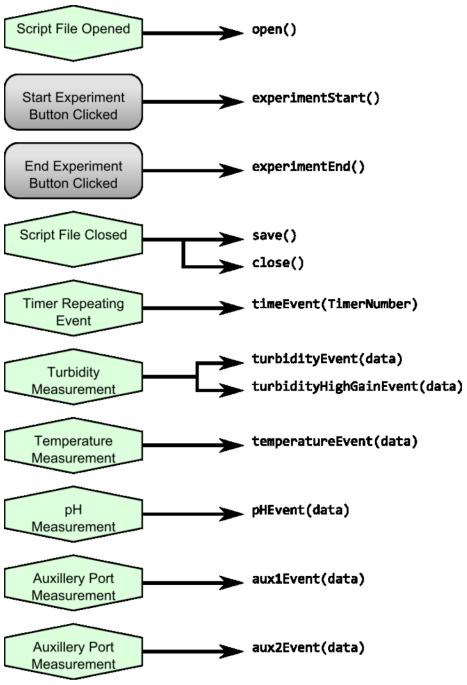

Figure 1: A list of all of the events that can be intercepted by a script and the corresponding functions that those events call.

In a typical script, periodic events are described in the `timeEvent(X)` function and their timers are created in the `open()` function. Most scripts will have environment parameter updates as one periodic event and request for measurements as another periodic event. The following figure shows how such a script works:

Figure 52 (cont'd)

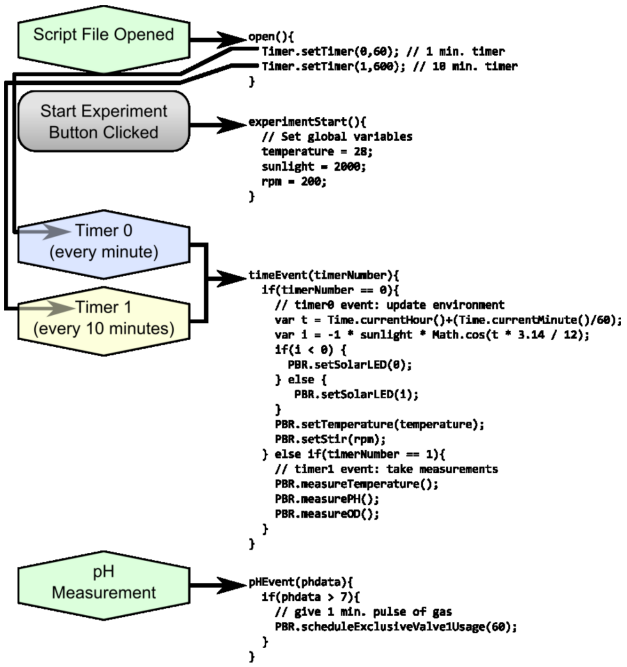

Figure 2: Structure of a typical script file. The open() function is called when the script file is loaded into AlgalCommand. This function creates two repeating timers, which cause a timing event at different intervals (1 minutes for timer 0 and 10 minutes for timer 1). Global variables in the script have their values reset when the user clicks on the "Start Experiment" button. The periodic timers call the timeEvent(…) function and pass in the numerical ID of the triggering timer. This script updates the environment on timer 0 (every minute) and takes measurements on timer 1 (every 10 minutes). When the ePBR returns pH data, the pHEvent(…) function is called, which triggers a dose of gas injection if the pH was measured to be above 7.

Figure 52 (cont'd)

Simple Scripts

The following is a simple script that you may use as a template for creating more advanced scripts. It uses 3 timers to update the light and temperature of the ePBR every minute, take measurements every 10 minutes, and give 2 minutes of sparging every hour. The functions to handle received data are blank because this script does not make decisions based on real time data (the measurements are automatically logged, so no scripting is required to save the data).

```
// global variables and default values
// (values of global variables are saved when script is
// closed and opened again, so the values should be
// reset in the experimentStart() function).
var peakIntensity = 0;
var temperature = 20;
// called when this file is loaded
function open() {
        Timer.setTimer(1, 1 * 60); // 1 min. interval
        Timer.setTimer(2,10 * 60); // 10 min. interval
        Timer.setTimer(3,60 * 60); // 1 hr interval
        PBR.setStir(200);
}
// called when the "Start Experiment" button is clicked
function experimentStart() {
        peakIntensity = 2000;
        temperature = 28;
}
// called when the "End Experiment" button is clicked
function experimentEnd() {
        peakIntensity = 0;
        PBR.stopTemperatureControl();
}
function timeEvent(timerID){
        if(timerID == 1){
                var daylength = 16;
                var intensity = peakIntensity * Simulation.sinusoidalDayFactor(daylength);
                PBR.setSolarLED(intensity);
                PBR.setTemperature(temperature);
        } else if(timerID == 2){
                PBR.measureOD();
                PBR.measureTemperature();
                PBR.measurePH();
        } else if(timerID == 3){
                PBR.scheduleExclusiveValve1Usage(120,10); // 10s purge, 2min. sparge
        }
}
// called when the script file is closed (e.g. when AlgalCommand is closed)
function save() {
        //
}
// called when the script file is closed (e.g. when AlgalCommand is closed)
function close() {
        //
}
// called when OD data is received
function turbidityEvent(opticalDensity) {
        //
}
// called when OD data is received
function turbidityHighGainEvent(opticalDensityHG){
        //
}
```

5

Figure 52 (cont'd)

```
// called when temperature data is received
function temperatureEvent(degreesC){
        //
}
// called when pH data is received
function pHEvent(pH){
        //
}
// called when aux ports are measured (this feature is not used by default)
function aux1Event(voltage){
        //
}
// called when aux ports are measured (this feature is not used by default)
function aux2Event(voltage){
        //
}
```

Script Equivalents to Manual Controls

Sinusoidal Day-Night Cycle

The `Simulation.sinusoidalDayFactor(dayLength)` function uses the same formula as the manual controls for calculating the sinusoidal approximation for a day-night cycle. The following code is an example that uses this function.

```
function timeEvent(timerID){
        if(timerID == 1){
                var daylength = 16;
                var intensity = peakIntensity * Simulation.sinusoidalDayFactor(daylength);
                PBR.setSolarLED(intensity);
        }
}
```

Temperature Fluctuations

The temperature fluctuation control in the manual controls is a very simplistic sine wave to emulate a pond getting warmer during the day and cooler at night. You may wish to phase-shift this behavior. The following code implements the same logic as the manual control with a phaseShift variable to shift the phase of the sine wave.

```
function timeEvent(timerID){
        if(timerID == 1){
                var tempAve = 20;
                var tempAmp = 5;
                var phaseShift = 0;
                var timeOfDay = Simulation.currentTimeOfDayInHours() - phaseShift;
                var temperature = tempAve - tempAmp * Math.sin(timeOfDay * Math.PI / 12);
                PBR.setTemperature(temperature);
        }
}
```

pH Control by Gas Injection

There are several ways to implement pH control by gas injection and the default control may not be suitable for your gas system. In the manual controls, pH control follows simple logic: when the pH is greater than [target + tolerance], the gas valve is turned on until the pH is below [target - tolerance].

Figure 52 (cont'd)

This logic ignores the state of other ePBRs, so it does not prevent multiple ePBRs from sparging at the same time. This manual controls are equivalent to this script code:

```
function pHEvent(pH){
        var target = 7.5;
        var tolerance = 0.75;
        if (pH > (target + tolerance)){
                PBR.setValve1(true);
        } else if (pH < (target - tolerance)){
                PBR.setValve1(false);
        }
}
```

If you wish to administer the sparges as 1 minute doses and did not want more than one ePBR to sparge at the same time, use this code instead:

```
function pHEvent(pH){
        var target = 7.5;
        if (pH > target){
                PBR.scheduleExclusiveValve1Usage(60);
        }
}
```

Turbidostat

Running a turbidostat requires that you either blank the vessel or otherwise use some reference point. The following code illustrates a turbidostat that tries to maintain the optical density at the time that the "Start Experiment" button was last clicked. If the culture is thick, move the code from `turbidityEvent(...)` to `turbidityHighGainEvent(...)`.

```
var setThreshold = false;
var odTarget = 100;
PBR.setAux2(false);
function experimentStart() {
        setThreshold = true;
        PBR.measureOD();
}
function turbidityEvent(opticalDensity) {
        if (setThreshold == true){
                odTarget = opticalDensity;
                setThreshold = false;
        } else {
                if (opticalDensity > odTarget){
                        PBR.triggerPump(1);
                }
        }
}
```

Figure 52 (cont'd)

Function Reference

Below is a list of functions provided by AlgalCommand for scripting. The scripting engine also allows the use of standard Java objects (e.g. `java.lang.Thread`) in the script file, but this is not recommended.

PBR

PBR.flashLED()

Blinks the solar LED of the ePBR several times.

PBR.logCustomData(measurementName, dataValue, unitOfMeasurement)

Logs custom data as if it was generated by the ePBR. The data will be graphed in the ePBR control window and

PBR.measureOD()

Tells the ePBR to take a turbidity measurement.

PBR.measureODNow()

Tells the ePBR to override the rolling average and take an immediate turbidity measurement.

PBR.measurePH()

Tells the ePBR to take a pH measurement

PBR.measureTemperature()

Tells the ePBR to take a temperature measurement

PBR.measureTransmission()

Tells the PBR to take an optical density measurement and return the raw voltage.

PBR.measureTransmissionNow()

Tells the PBR to override the rolling average and take an optical density measurement and return the raw voltage.

PBR.scheduleExclusiveValve1Usage(secondsOn)

Causes the ePBR to receive a pulse of gas through valve 1 at some time in the future, where the duration of the pulse is equal to the provided number. AlgalCommand will coordinate the operation of the gas valves so that if multiple ePBRs use this function at the same time, the gas will be delivered to only 1 ePBR at a time, roughly in the order that they called this function.

PBR.scheduleExclusiveValve1Usage(secondsOn, purgeTime)

Figure 52 (cont'd)

Same as PBR.scheduleExclusiveValve1Usage(secondsOn), except that valve 2 will be opened for a pulse immediately before opening valve 1. Use this function to depressurize the gas system if pressure builds up in your gas system while all ePBRs are not using the gas.

PBR.scheduleExclusiveValve2Usage(secondsOn)

Causes the ePBR to receive a pulse of gas through valve 2 at some time in the future, where the duration of the pulse is equal to the provided number. AlgalCommand will coordinate the operation of the gas valves so that if multiple ePBRs use this function at the same time, the gas will be delivered to only 1 ePBR at a time, roughly in the order that they called this function.

PBR.setAux1(true|false)

Call PBR.setAux1(true) to turn on and PBR.setAux1(false) the power to the aux1 (light heater) port. Aux ports are **on** by default.

PBR.setAux2(true|false)

Call PBR.setAux2(true) to turn on and PBR.setAux2(false) the power to the aux2 (aux) port. Aux ports are **on** by default.

PBR.setSolarLED(intensity)

Sets the light intensity of the illumination LED

PBR.setSolarLEDVoltage(voltage)

Sets the raw voltage setting on the control circuit for the LED. *This is not the voltage output to the LED.* The LED is on a current-regulating circuit whose current is proportional to the control voltage.

PBR.setStir(rpm)

Sets the speed of the stirring motor.

PBR.setTemperature(degreesC)

Sets the temperature control target for the ePBR.

PBR.setValve1(true|false)

Call PBR.setValve1(true) to open gas valve 1 and PBR.setValve1(false) to close it.

PBR.setValve2(true|false)

Call PBR.setValve2(true) to open gas valve 2 and PBR.setValve1(false) to close it.

PBR.stopTemperatureControl()

Tells the PBR to stop regulating the temperature

Figure 52 (cont'd)

PBR.triggerPump(secondsOn)

Tells the PBR to trigger a dose of dilution media from the turbidostat pump. The trigger signal will be on for the given number of seconds (1 second is good for edge-triggered pumps).

Simulation

Simulation.currentTimeOfDayInHours()

returns the time of day in hours from 0 to 24

Simulation.sinusoidalDayFactor(dayLength)

Returns a number from 0 to 1 specifying what the light intensity should be based on the time of day and day length using a sinusoidal approximation (same calculation as the sinusoidal day setting in the control window). Multiply this number by the peak light intensity to replicate the behavior of the manual controls.

Simulation.sinusoidalDayFactor(timeInHours, dayLength)

Same as sinusoidalDayFactor(dayLength), but uses the provided number as the time of day instead of the system clock.

Timer

Timer.setTimer(idNumber, interval)

Sets up a timer to trigger the timeEvent(id) function at a specified interval. The interval is specified in seconds.

Timer.removeTimer(idNumber)

Deletes a timer that was previously created with Timer.setTimer(idNumber, interval).

Timer.removeAllTimers()

Deletes all timers.

Time

Time.currentDayOfMonth()

Returns the current day of the month

Time.currentDayOfYear()

Returns the current day of the year

Time.currentHour()

Returns the current hour in the day

Figure 52 (cont'd)

Time.currentMinute()

Returns the current minute

Time.currentMonth()

Returns the current month of the year

Time.currentSecond()

Returns the current second

Time.currentTimeInDays()

Returns the raw system time (time since 1970), converted to days

Time.currentTimeInHours()

Returns the raw system time (time since 1970), converted to hours

Time.currentTimeInMinutes()

Returns the raw system time (time since 1970), converted to minutes

Time.currentTimeInYears()

Returns the raw system time (time since 1970), converted to years

Time.currentYear()

Returns the current year

Time.getTimeStamp()

Returns a text representation of the current time

Math

See http://www.w3schools.com/jsref/jsref_obj_math.asp

GUI

GUI.getInput(name, initialValue)

Launches a pop-up asking for an input value and returns either the new value (if the user clicked OK) or the initial value (if the user clicked cancel). For example:

```
useSpecial = GUI.getInput("Use special function?", false);

setting = GUI.getInput("What value to set?", 1500);
```

11

Figure 52 (cont'd)

Only supports Strings, Numbers, and booleans.

ScheduleReader

The ScheduleReader class is provided for parsing tab-delimited files describing the environmental settings of the ePBR over time. The first line of the schedule text file contains the headers for the columns (required). One of the columns must be TIME, which is formatted as hour:minute:second. The hour portion is hours from start of experiment, not time of day. The schedule does not automatically repeat itself. Typical usage in script:

```
function open() {
	Timer.setTimer(1, 60);
}
function experimentStart() {
	startTime = ScheduleReader.currentTime();
	scheduleFile = ""+ScheduleReader.askForFile("Choose schedule file");
}
function timeEvent(timerID){
	if(timerID == 1){
		if(scheduleFile != null && startTime != null){
			if(schedule == null){
				schedule = new ScheduleReader(scheduleFile);
			}
schedule.setPBR(PBR,ScheduleReader.timeSince(startTime));
// use "schedule.setPBR(PBR, ScheduleReader.timeOfDayInMilliseconds());"
// for repeating 24hr schedule

		}
	}
}
```

Typical contents of schedule file:

TIME	LINT	TEMP	STIR
0:00:00	0	23.4	0
4:00:00	0	22.4	0
8:00:00	414.3	25.3	200
12:00:00	1696	27.3	200
16:00:00	1017	27.4	200
20:00:00	0	25.7	0
24:00:00	0	24.4	0
28:00:00	0	22.6	0
32:00:00	603.2	25.2	200
36:00:00	1572	27.2	200
40:00:00	941.4	26.8	200
44:00:00	0	25.4	0
48:00:00	0	24.8	0

Figure 52 (cont'd)

To make the schedule repeat every 24 hours, replace `schedule.setPBR(PBR,ScheduleReader.timeSince(startTime));` with `schedule.setPBR(PBR, ScheduleReader.timeOfDayInMilliseconds());`

ScheduleReader.askForFile()

Shows a pop-up asking the user to select a file.

ScheduleReader.currentTime()

Returns the current time, expressed in computer standard millisecond time (milliseconds since midnight on Jan. 1st, 1970).

_____.setPBR(PBR, mstime)

Sets the environmental properties of the given PBR using interpolated values from the loaded schedule file. The variable mstime refers to the time since the start of the experiment, in milliseconds. This function can only be called on a variable that was assigned the value of a new ScheduleReader instance:

```
schedule = new ScheduleReader(scheduleFile);
…
schedule.setPBR(PBR,ScheduleReader.timeSince(startTime));
```

ScheduleReader.timeOfDayInMilliseconds()

Returns the number of milliseconds since midnight.

ScheduleReader.timeSince(initialTime)

Returns the amount of time since the given time point, in milliseconds.

APPENDIX F

OXYGEN PRODUCTION ASSAY SCRIPT FILES

```
[ O2 vs bicarb script IDEAspec.txt ]

' Script to measure o2 evolution for CCM determination
set_base_file
ref_channel(1)

!lt
!sat



record_events(1)
plot_clear
record_files(1)
note_query
record_script


number_protocols(5)
gain_slop(0.7)

'basic dirk
current_protocol(1)
in_channel(0)
adc_gain(bip10volts)
measuring_pulse_duration(20u)
m_number_loops(3)
m_intensity(0,0,0)
l_measuring_interval(2m,2m,2m)
m_pulse_set(250,250,250)
m_number_measuring_lights(1)
m_measuring_light(7)
m_detector_gain(3)
m_reference_gain(4)
baseline_start(241)
baseline_end(250)

'basic fluorescence
current_protocol(2)
in_channel(0)
adc_gain(bip10volts)
measuring_pulse_duration(20u)
m_number_loops(5)
m_intensity(0,0,0,0,0)
m_pulse_set(100,100,200,100,100)
m_measuring_light(8)
l_measuring_interval(5m,5m,5m,5m,5m)
M_detector_gain(5)
m_reference_gain(0)
baseline_start(1)
baseline_end(10)



'traces
number_traces(100)

current_trace(1)
save_mode(file_append)
time_mode(sequential)
trace_note(fluorescence)
trace_protocol(2)
```

```
current_trace(2)
save_mode(file_append)
time_mode(sequential)
trace_note(505 nm)
trace_protocol(1)

current_trace(3)
save_mode(file_append)
time_mode(sequential)
trace_note(520)
trace_protocol(1)

current_trace(4)
save_mode(file_append)
time_mode(sequential)
trace_note(535)
trace_protocol(1)

'start experiments

f_shutter(0)
stir(1)
#sat(1)=255
#lt(0)=0
' cal curve - 13 = 112 uE & 16 = 188 uE & 28 = 490 uE
' 1040 uE <- 50
' 490 uE -> 28
' 238 uE -> 18
' 112 uE -> 13
#lt(1)=50

' start at standard intensity to speed-up Ci depletion
intensity(28)



' 15 min. air sparge
wait(900)
' wait for O2 production to stop
' then add uM bicarb and skip
wait(3600)
stir(1)


intensity(@lt(1))
wait(180)
sub(sinfl)
stir(1)

intensity(@lt(0))
wait(180)

intensity(@lt(1))
' add 5 mM bicarb then skip
' that is 25 uL of 0.5M bicarb solution
wait(900)

' max O2 production and consumption
intensity(@lt(1))
wait(180)
sub(sinfl)
stir(1)
```

```
intensity(@lt(0))
wait(210)



far_red(0)

intensity(0)
stir(0)
end



'fluorescence induction
measurements|

lb(2,10)
sub(sinfl)
wait(51)
sub(sindirk)
wait(6)
sub(sindirk)
wait(6)
sub(sindirk)
wait(6)
sub(sindirk)
wait(6)

plot_raw(3)
le(2)

return

'fluorescence recovery
dark_recovery|
sub(sinfl)

lb(2,9)
far_red(1)
wait(112)
far_red(0)
sub(sinfl)
le(2)
return



'single fluorescence trace
sinfl|

current_trace(1)
current_protocol(2)
m_intensity(@lt(1),@sat(1),0,0,0)
m_far_red(0,0,0,1,0)

stir(0)
f_shutter(1)
wait(5)
m_trace
intensity(@lt(1))
stir(1)
plot_raw(1)
```

```
return



'single 520nm dirk
sindirk|

current_trace(3)
current_protocol(1)
m_intensity(@lt(1),0,@lt(1))

stir(0)
f_shutter(0)
wait(5)
m_trace
stir(1)

return
```

[SlopeFinder2.py]

```
'''
Created on Jun 20, 2016

@author: CCHall
'''

import pandas as panda
from scipy import stats
import numpy
import tkinter as tk
from tkinter import filedialog
import collections
import sys
from matplotlib import pyplot
import time


class OutputSplitter(object):
 def __init__(self, *files):
  self.files = files
 def write(self, obj):
  for f in self.files:
   f.write(obj)
   f.flush()
 def flush(self) :
  for f in self.files:
   f.flush()


def main():
 setup()
 print("\n\n\nStarting Slope-Finder 2:", time.strftime("%c"))
 dataFiles = askForDataFiles()
 for dataFile in dataFiles:
  print("\nProcessing file: ",dataFile)
  data = readData(dataFile)
  label = str(dataFile)
  plotData(data, label[label.rfind('/')+1:] )
 close()

def setup():
 # Make print statements go to log file and console simultaeously
 global logfile
 global stdout
 stdout = sys.stdout
 logfile = open('SlopeFinder2.log', 'a')
 sys.stdout = OutputSplitter(sys.stdout, logfile)
 # GUI initialization
 root = tk.Tk()
 root.withdraw()

def close():
 sys.stdout = sys.stdout # needed so that closing messages don't thorw errors
 logfile.close()

def askForDataFiles():
 files = filedialog.askopenfilenames()
 return files

def readData(file):
 return panda.read_csv(file)
```

```
currentPlotDataSet = None
currentPlot = None

def calcSlopeOnclick(event):
 global currentPlotDataSet
 global currentPlot
#  print('button=%d, x=%d, y=%d, xdata=%f, ydata=%f' %
#     (event.button, event.x, event.y, event.xdata, event.ydata))
#  print(currentPlotDataSet is not None)
#  print(currentPlot is not None)
 if(currentPlotDataSet is not None):
  fitMargin = 45
  minx = max(0,event.xdata - fitMargin)
  maxx = event.xdata + fitMargin
  index = 0
  while currentPlotDataSet[0][index] < minx:
   index += 1
  start = index
  end = min(len(currentPlotDataSet[0]),(index+(2*fitMargin)))
  newX = currentPlotDataSet[0][start:end]
  newY = currentPlotDataSet[1][start:end]

  slope, intercept, r, prob, sterrest = stats.linregress(newX,newY)
  print('%f\t' %
    (slope), end="")
  if(currentPlot is not None):
   fitY = []
   for nx in newX:
    fitY.append(slope * nx + intercept)
   currentPlot.plot(newX,fitY, linestyle='-', color='red')
   pyplot.draw()

def plotData(data, label):
 global currentPlotDataSet
 global currentPlot
 timeColumnIndex = "Time"
 dataColumnIndex = " Oxygen"
 firstRowIndex = 0
 count = 0
 x=[]
 y=[]
 for row in range(1,len(data[timeColumnIndex])):
  time = row - firstRowIndex # each row data point is 1 second apart
  value = float(data[dataColumnIndex][row]) # python float is 64 bit, usually
  x.append(time)
  y.append(value)
  count = count + 1

 currentPlotDataSet = (x,y)

 fig = pyplot.figure() # make new figure instance
 subplot = fig.add_subplot(111)
 #  e.g.  pyplot.plot(x,y, marker='o', linestyle='--', color='r')
 subplot.plot(x,y, linestyle='-', color='black')
 currentPlot = subplot
 print('slopes for', label)
 eventHandle = fig.canvas.mpl_connect('button_press_event', calcSlopeOnclick)
 pyplot.xlim(min(x)-1,max(x)+1)
 pyplot.ylim(min(y)-1,max(y)+1)
 pyplot.show()

'''
```

```
Create a running linear fit of data and corresponding fitting error
returns pandas DataFrame of four columns: "x", "y", "slope" (for each point), "error"
(fitting error for each point)
'''
def processData(data):
 timeColumnIndex = "Time"
 dataColumnIndex = " Oxygen"
 firstRowIndex = 0
 count = 0
 x=[]
 y=[]
 for row in range(1,len(data[timeColumnIndex])):
  time = row - firstRowIndex # each row data point is 1 second apart
  value = float(data[dataColumnIndex][row]) # python float is 64 bit, usually
  x.append(time)
  y.append(value)
  count = count + 1

 # now do running linear fit
 fitMargin = 60
 dydx=[]
 err=[]
 for i in range(0,count):
  minI = max(0,i-fitMargin)
  maxI = min(count-1,i+fitMargin)
  slope, intercept, r, prob, sterrest = stats.linregress(x[minI:maxI],y[minI:maxI])
  dydx.append(slope)
  err.append(1-r)

 # do some smoothing to make manual interpretation easier
 smoothing_radius = 5
 smoothed = []
 for i in range(0,count):
  minI = max(0,i-smoothing_radius)
  maxI = min(count-1,i+smoothing_radius)
  smoothed.append(numpy.average(dydx[minI:maxI]))


 dataMap = collections.OrderedDict()
 dataMap['x']=panda.Series(x)
 dataMap['y']=panda.Series(y)
 dataMap['slope']=panda.Series(dydx)
 dataMap['error']=panda.Series(err)
 dataMap['smoothed_slope']=panda.Series(smoothed)

 return panda.DataFrame(dataMap)

def askForOutputFile(inputFile):
 # TODO: ask user for file
 return inputFile + "_processed.csv"

'''
Takes a pandas.DataFrame and a filename and saves a CSV formatted file
'''
def writeData(pandaDataFrame,file):
 pandaDataFrame.to_csv(file)

if __name__ == '__main__':
 print("Running Slope Finder")
 main()
 print()
 print("\nDone.")
```

APPENDIX G

OXYGEN PRODUCTION VERSUS BICARBONATE CONCENTRATION

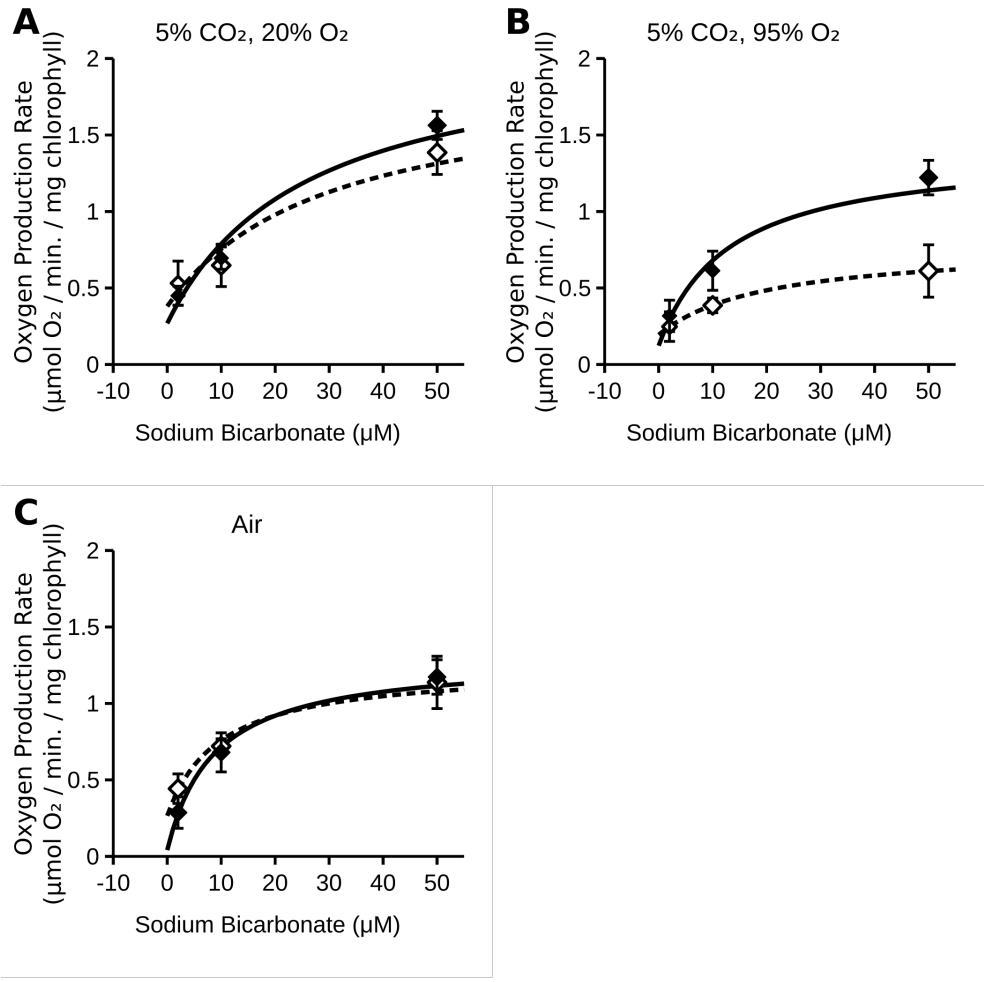

Figure 53: Oxygen production versus added sodium bicarbonate. *Oxygen production as a function of the sodium bicarbonate concentration in cuvette samples of turbidostat ePBR cultures. Oxygen production rates in strain CC-1009 (black diamonds, solid line) and CC-2343 (hollow diamonds, dashed line) were determined after the addition of sodium bicarbonate to concentrations of 2, 10, and 50 µM. The curved lines represent the best fit of the Michaelis-Menten formula to the data, with the assumption that the inorganic carbon concentration prior to the addition of sodium bicarbonate may be greater than zero (maximum rate of oxygen production, assayed at 5 millimolar sodium bicarbonate, is not shown). Error bars represent one standard deviation from 3 independent turbidostat cultures.*

ePBR Gas Source	Strain	V_{max}	SD	K_M	S_0	R^2
Air						
	CC-1009	1.3	0.21	8.4	0.27	0.9880
	CC-2343	1.2	0.26	7.6	2.1	0.9797
Normoxia						
	CC-1009	2.1	0.39	22	3.2	0.9770
	CC-2343	1.9	0.10	24	6.0	0.9534
Hyperoxia						
	CC-1009	1.4	0.16	12	1.1	0.9714
	CC-2343	0.77	0.13	15	5.0	0.9999

Table 3: Oxygen production versus sodium bicarbonate Michaelis-Menten parameters. *Oxygen production rates with 5 mM sodium bicarbonate in algae samples taken from various ePBR culturing conditions. Michaelis-Menten curve-fitting was used to estimate the effective K_M for sodium bicarbonate and the apparent residual inorganic carbon concentration prior to the addition of sodium bicarbonate (S_0). The coefficient of determination (R^2) for each fit is listed to provide context for the estimated K_M value.*

V_{max} - average O_2 production rate, in µmol O_2 / min. / mg chlorophyll

SD - one standard deviation of the Vmax data (N = 3)

KM - Michaelis-Menten affinity constant for sodium bicarbonate, in µM sodium bicarbonate

S_0 - apparent initial inorganic carbon concentration prior to the addition of sodium bicarbonate in µM sodium bicarbonate

R^2 - Coefficient of determination for the Michaelis-Menten fit used to derive the K_M value

APPENDIX H

GLYCOLATE EXCRETION ASSAY SCRIPT FILES

```
[ ECS-NPQ-qP (490 uE) with interrupts.txt ]

set_base_file
ref_channel(1)

!lt
!sat


record_events(1)
plot_clear
record_files(1)
note_query
record_script


number_protocols(5)
gain_slop(0.7)

'basic dirk
current_protocol(1)
in_channel(0)
adc_gain(bip10volts)
measuring_pulse_duration(20u)
m_number_loops(3)
m_intensity(0,0,0)
l_measuring_interval(2m,2m,2m)
m_pulse_set(250,250,250)
m_number_measuring_lights(1)
m_measuring_light(7)
m_detector_gain(3)
m_reference_gain(4)
baseline_start(241)
baseline_end(250)

'basic fluorescence
current_protocol(2)
in_channel(0)
adc_gain(bip10volts)
measuring_pulse_duration(20u)
m_number_loops(5)
m_intensity(0,0,0,0,0)
m_pulse_set(100,100,200,100,100)
m_measuring_light(8)
l_measuring_interval(5m,5m,5m,5m,5m)
M_detector_gain(5)
m_reference_gain(0)
baseline_start(1)
baseline_end(10)


'traces
number_traces(100)

current_trace(1)
save_mode(file_append)
time_mode(sequential)
trace_note(fluorescence)
trace_protocol(2)

current_trace(2)
save_mode(file_append)
time_mode(sequential)
```

```
trace_note(505 nm)
trace_protocol(1)

current_trace(3)
save_mode(file_append)
time_mode(sequential)
trace_note(520)
trace_protocol(1)

current_trace(4)
save_mode(file_append)
time_mode(sequential)
trace_note(535)
trace_protocol(1)

'start experiments


f_shutter(0)
stir(1)
#sat(1)=255
#lt(0)=0
#lt(1)=0
intensity(@lt(0))

' dark adaptation
intensity(0)
wait(1500)
far_red(1)
wait(300)
far_red(0)

'fM
sub(sinfl)
wait(30)

#lt(1)=28
intensity(@lt(1))
wait(30)

' 10 minutes in the light
sub(measurements)

' time to change things
stir(0)
wait(600)
stir(1)

sub(measurements)

' time to change things
stir(0)
wait(600)
stir(1)

sub(measurements)


#lt(1)=0

' dark recovery
intensity(@lt(0))
sub(dark_recovery)
```

```
far_red(0)

intensity(0)
stir(0)
end


'fluorescence induction
measurements|

lb(2,10)
sub(sinfl)
wait(51)
sub(sindirk)
wait(6)
sub(sindirk)
wait(6)
sub(sindirk)
wait(6)
sub(sindirk)
wait(6)

plot_raw(3)
le(2)

return

'fluorescence recovery
dark_recovery|
sub(sinfl)

lb(2,9)
far_red(1)
wait(112)
far_red(0)
sub(sinfl)
le(2)
return


'single fluorescence trace
sinfl|

current_trace(1)
current_protocol(2)
m_intensity(@lt(1),@sat(1),0,0,0)
m_far_red(0,0,0,1,0)

stir(0)
f_shutter(1)
wait(5)
m_trace
intensity(@lt(1))
stir(1)
plot_raw(1)

return


'single 520nm dirk
sindirk|
```

```
current_trace(3)
current_protocol(1)
m_intensity(@lt(1),0,@lt(1))

stir(0)
f_shutter(0)
wait(5)
m_trace
stir(1)

return
```

APPENDIX I

HYDROGEN PEROXIDE ASSAY

Hydrogen peroxide excretion is sometimes used as a measure of Mehler cycling activity in *C. reinhardtii* (as described in (Allorent *et al.* 2013)). When I tested this technique using NAP10 strain *C. reinhardtii*, I found that the culture produced hydrogen peroxide at a rate of 5.7 nmol H_2O_2/min./mg chlorophyll in an atmosphere of 100% O_2 (Figure 54). However, the hydrogen peroxide amounts produced by NAP10 were near the lower-limit of the sensitivity of this assay and I was unable to reduce the variability enough to make quantitative comparisons. This assay was not attempted with strains CC-1009 nor CC-2343.

The appearance of H_2O_2 in the media was assayed on samples collected during the photosynthetic measurements described above, using the Amplex Red fluorescence assay (ThermoFisher Scientific).Aliquots of 250 µL of algae suspensions were rapidly sampled and introduced into 3 mL capacity square fluorometer cuvettes, along with 12 µM Amplex Red (1.5 µL ice cold solution of 20 mM Amplex Red dissolved in dimethyl sulfoxide) and 1 unit of Type VI Horseradish Peroxidase (2.5 µL ice cold solution of 400 units/mL Horse Radish Peroxidase in 1M potassium phosphate buffer, pH 6.0). This cuvette was then incubated in the dark at room temperature for 5 minutes in the fluorimeter chamber and then the fluorescence spectrum was scanned from 575 nm to 700 nm with 550 nm excitation wavelength. The cuvette was then washed twice with sterile media and reused. The hydrogen peroxide

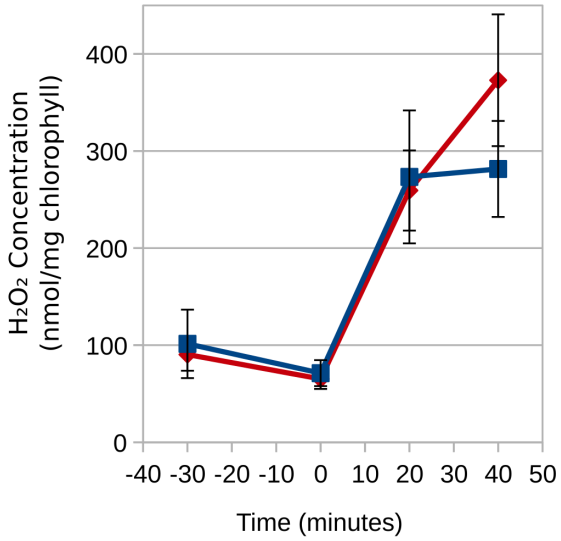

Figure 54: Hydrogen peroxide concentration in cuvette samples of normoxia cultivated* Chlamydomonas reinhardtii *strain NAP10. *Samples were taken from the ePBR turbidostats at time -30 minutes, given sodium bicarbonate to a concentration of 5 mM, and then incubated in the dark with air bubbling for 30 minute before the start of illumination at time 0 (490 µmol photons PAR/m^2/s illumination intensity). At time 20 minutes, the bubble gas source was either switched to oxygen (red symbols and line) or kept on air (blue symbols and line). Bubbling with oxygen for 20 minutes slightly increased the hydrogen peroxide concentration relative to air, but not to the point of being a statistically significant increase.*

signal was quantified by comparing the peak fluorescence intensities with a linear formula fit to a series of known hydrogen peroxide concentrations assayed as above after the final time point for the experiment has been assayed.

IDEA spectrophotometer script:

```
[ IDEA spec ECS-NPQ (490 uE).txt ]

set_base_file
ref_channel(1)

!lt
!sat


record_events(1)
plot_clear
record_files(1)
note_query
record_script


number_protocols(5)
gain_slop(0.7)

'basic dirk
current_protocol(1)
in_channel(0)
adc_gain(bip10volts)
measuring_pulse_duration(20u)
m_number_loops(3)
m_intensity(0,0,0)
l_measuring_interval(2m,2m,2m)
m_pulse_set(250,250,250)
m_number_measuring_lights(1)
m_measuring_light(7)
m_detector_gain(3)
m_reference_gain(4)
baseline_start(241)
baseline_end(250)

'basic fluorescence
current_protocol(2)
in_channel(0)
adc_gain(bip10volts)
measuring_pulse_duration(20u)
m_number_loops(5)
m_intensity(0,0,0,0,0)
m_pulse_set(100,100,200,100,100)
m_measuring_light(8)
l_measuring_interval(5m,5m,5m,5m,5m)
M_detector_gain(5)
m_reference_gain(0)
baseline_start(1)
baseline_end(10)


'traces
number_traces(100)

current_trace(1)
save_mode(file_append)
time_mode(sequential)
trace_note(fluorescence)
trace_protocol(2)

current_trace(2)
```

```
save_mode(file_append)
time_mode(sequential)
trace_note(505 nm)
trace_protocol(1)

current_trace(3)
save_mode(file_append)
time_mode(sequential)
trace_note(520)
trace_protocol(1)

current_trace(4)
save_mode(file_append)
time_mode(sequential)
trace_note(535)
trace_protocol(1)

'start experiments


f_shutter(0)
stir(1)
#sat(1)=255
#lt(0)=0
#lt(1)=0
intensity(@lt(0))

' dark adaptation
intensity(0)
wait(1500)
far_red(1)
wait(300)
far_red(0)

'fM
sub(sinfl)
wait(30)

intensity(@lt(1))
#lt(1)=28
wait(80)

' 10 minutes in the light
sub(measurements)

' time to change things
wait(600)

sub(measurements)

' time to change things
wait(600)

sub(measurements)


wait(60)

#lt(1)=0

' dark recovery
intensity(@lt(0))
sub(dark_recovery)
```

```
far_red(1)
wait(60)
far_red(0)
sub(dark_recovery)

far_red(0)

intensity(0)
stir(0)
end


'fluorescence induction
measurements|

lb(2,10)
sub(sinfl)
wait(51)
sub(sindirk)
wait(51)
le(2)

return

'fluorescence recovery
dark_recovery|
sub(sinfl)

lb(2,9)
far_red(1)
wait(112)
far_red(0)
sub(sinfl)
le(2)
return


'single fluorescence trace
sinfl|

current_trace(1)
current_protocol(2)
m_intensity(@lt(1),@sat(1),0,0,0)
m_far_red(0,0,0,1,0)

stir(0)
f_shutter(1)
wait(5)
m_trace
intensity(@lt(1))
stir(1)
plot_raw(1)

return


'single 520nm dirk
sindirk|

current_trace(3)
current_protocol(1)
m_intensity(@lt(1),0,@lt(1))
```

```
stir(0)
f_shutter(0)
wait(5)
m_trace
stir(1)
plot_raw(3)
plot_ref(4)

delta_a
plot_delta(2)

return
```

APPENDIX J

PERMISSIONS FOR USE OF COPYRIGHTED MATERIALS

Permission granted for reproduction of Figure 1 from *Rochaix, J.-D. (2011). Biochimica et Biophysica Acta (BBA) - Bioenergetics, 1807(3), 375–383*. RightsLink license #3979521430165.

Permission granted for reproduction of Figure 1 from *Stirbet, A., & Govindjee. (2011), Journal of Photochemistry and Photobiology. B, Biology, 104(1–2), 236–57*. RightsLink license #3963200417012.

Permission granted for reproduction of Figure 1 from *Baker, N. R., Harbinson, J., & Kramer, D. M. (2007). Plant, Cell & Environment, 30(9), 1107–1125*. RightsLink license #3977661036402.

Permission granted for reproduction of Figures 2, 4, 5, and 6 from *Lucker, B. F., Hall, C. C., Zegarac, R., & Kramer, D. M. (2014), Algal Research, 6, Part B, 242–249*. RightsLink license #4060000845495.

Permission granted for redistribution of *Lucker, B. F., Hall, C. C., Zegarac, R., & Kramer, D. M. (2014), Algal Research, 6, Part B, 242–249*. RightsLink license #4074261382376.

WORKS CITED

WORKS CITED

Adams R.M., Rosenzweig C., Peart R., Ritchie J.T., McCarl B.A. & others (1990) Global climate change and US agriculture. *Nature* **345**, 219.

Agostoni M., Lucker B.F., Smith M.A.Y., Kanazawa A., Blanchard G.J., Kramer D.M. & Montgomery B.L. (2016) Competition-based phenotyping reveals a fitness cost for maintaining phycobilisomes under fluctuating light in the cyanobacterium Fremyella diplosiphon. *Algal Research* **15**, 110–119.

Allahverdiyeva Y., Suorsa M., Tikkanen M. & Aro E.-M. (2014) Photoprotection of photosystems in fluctuating light intensities. *Journal of experimental botany*.

Allied Vision Technologies GmbH (2017) Camera Selection Guide.

Allorent G., Tokutsu R., Roach T., Peers G., Cardol P., Girard-Bascou J., … Finazzi G. (2013) A dual strategy to cope with high light in Chlamydomonas reinhardtii. *The Plant cell* **25**, 545–57.

Amazon (2016, November 27) Amazon Machine Learning. Retrieved from https://aws.amazon.com/machine-learning/

Amesz J., Hoff A.J. & Van Gorkum H.J. eds. (1986) *Current topics in photosynthesis*. Springer Netherlands, Dordrecht.

Anderson R.A. ed. (2005) *Algal culturing techniques*, 4th ed. Elsevier Academic Press, Burlington, MA, USA.

Araus J.L. & Cairns J.E. (2014) Field high-throughput phenotyping: the new crop breeding frontier. *Trends in Plant Science* **19**, 52–61.

Aro E.-M., Virgin I. & Andersson B. (1993) Photoinhibition of Photosystem II. Inactivation, protein damage and turnover. *Biochimica et Biophysica Acta (BBA) - Bioenergetics* **1143**, 113–134.

Asada K. (1999) The water-water cycle in chloroplasts: Scavenging of active oxygens and dissipation of excess photons. *Annual review of plant physiology and plant molecular biology* **50**, 601–639.

Attaran E., Major I.T., Cruz J.A., Rosa B.A., Koo A.J.K., Chen J., … Howe G.A. (2014) Temporal dynamics of growth and photosynthesis suppression in response to jasmonate signaling. *Plant Physiology* **165**, 1302–1314.

Austic G. (2016, December 12) PhotosynQ Blog. Retrieved from https://blog.photosynq.org/

Badger M.R., von Caemmerer S., Ruuska S. & Nakano H. (2000) Electron flow to oxygen in higher plants and algae: rates and control of direct photoreduction (Mehler reaction) and rubisco oxygenase. *Philosophical transactions of the Royal Society of London. Series B, Biological sciences* **355**, 1433–46.

Bailleul B., Cardol P., Breyton C. & Finazzi G. (2010) Electrochromism: A useful probe to study algal photosynthesis. *Photosynthesis research* **106**, 179–89.

Bainbridge R. (1957) The size, shape and density of marine phytoplankton concentrations. *Biological Reviews* **32**, 91–115.

Baker N.R. (2008) Chlorophyll fluorescence: A probe of photosynthesis in vivo. *Annual Review of Plant Biology* **59**, 89–113.

Baker N.R., Harbinson J. & Kramer D.M. (2007) Determining the limitations and regulation of photosynthetic energy transduction in leaves. *Plant, Cell & Environment* **30**, 1107–1125.

Ballaré C.L. & Casal J.J. (2000) Light signals perceived by crop and weed plants. *Field Crops Research* **67**, 149–160.

Béchet Q., Shilton A., Park J.B.K., Craggs R.J. & Guieysse B. (2011) Universal temperature model for shallow algal ponds provides improved accuracy. *Environmental science & technology* **45**, 3702–9.

Becker E.W. (1994) *Microalgae: Biotechnology and Microbiology*. Cambridge University Press, New York.

Berry J., Boynton J., Kaplan A. & Badger M. (1976) Growth and photosynthesis of Chlamydomonas reinhardtii as a function of CO2 concentration. *Yearbook of the Carnegie Institution of Washington* **75**, 423–432.

Beudeker R.F. & Tabita F.R. (1983) Control of photorespiratory glycolate metabolism in an oxygen-resistant mutant of Chlorella sorokiniana. *Journal of Bacteriology* **155**, 650–656.

Biddington N.L. (1986) The effects of mechanically-induced stress in plants – a review. *Plant Growth Regulation* **4**, 103–123.

Blankenship R.E. (2002) *Molecular Mechanisms of Photosynthesis*, 2nd ed. Blackwell Science Ltd, Malden, MA.

Bonaventura C. & Myers J. (1969) Fluorescence and oxygen evolution from Chlorella pyrenoidosa. *Biochimica et Biophysica Acta (BBA) - Bioenergetics* **189**, 366–383.

Briantais J.-M., Vernotte C., Picaud M. & Krause G.H. (1979) A quantitative study of the slow decline of chlorophyll a fluorescence in isolated chloroplasts. *Biochimica et Biophysica Acta (BBA) - Bioenergetics* **548**, 128–138.

Buhr H.O. & Miller S.B. (1983) A dynamic model of the high-rate algal-bacterial wastewater treatment pond. *Water Research* **17**, 29–37.

Calkins V. (1943) Microdetermination of glycolic and oxalic acids. *Industrial & Engineering Chemistry Analytical Edition* **15**, 762–763.

Checchetto V., Teardo E., Carraretto L., Leanza L. & Szabo I. (2016) Physiology of intracellular potassium channels: A unifying role as mediators of counterion fluxes? *Biochimica et Biophysica Acta (BBA) - Bioenergetics* **1857**, 1258–1266.

Chylla R.A., Garab G. & Whitmarsh J. (1987) Evidence for slow turnover in a fraction of Photosystem II complexes in thylakoid membranes. *Biochimica et Biophysica Acta (BBA) - Bioenergetics* **894**, 562–571.

Cirulis J.T., Scott J.A. & Ross G.M. (2013) Management of oxidative stress by microalgae. *Canadian journal of physiology and pharmacology* **91**, 15–21.

Coale K.H., Johnson K.S., Fitzwater S.E., Gordon R.M. & others (1996) A massive phytoplankton bloom induced by an ecosystem-scale iron fertilization experiment in the equatorial Pacific Ocean. *Nature* **383**.

Cramer W.A., Soriano G.M., Ponomarev M., Huang D., Zhang H., Martinez S.E. & Smith J.L. (1996) Some new structural aspects and old controversies concerning the cytochrome b 6 f complex of oxygenic photosynthesis. *Annual review of plant biology* **47**, 477–508.

Crane F.L. (1959) Internal distribution of coenzyme Q in higher plants. *Plant Physiology* **34**, 128–131.

Cruz J.A., Avenson T.J., Kanazawa A., Takizawa K., Edwards G.E. & Kramer D.M. (2005) Plasticity in light reactions of photosynthesis for energy production and photoprotection. *Journal of experimental botany* **56**, 395–406.

Cruz J.A., Sacksteder C.A., Kanazawa A. & Kramer D.M. (2001) Contribution of electric field (Δψ) to steady-state transthylakoid proton motive force (pmf) in vitro and in vivo. Control of pmf parsing into Δψ and ΔpH by ionic strength. *Biochemistry* **40**, 1226–1237.

Davis G.A., Kanazawa A., Schöttler M.A., Kohzuma K., Froehlich J.E., Rutherford A.W., … Kramer D.M. (2016) Limitations to photosynthesis by proton motive force-induced photosystem II photodamage. *eLife* **5**, e16921.

Demmig-Adams B. & Adams W.W. (1996) The role of xanthophyll cycle carotenoids in the protection of photosynthesis. *Trends in Plant Science* **1**, 21–26.

Dietzel L., Bräutigam K. & Pfannschmidt T. (2008) Photosynthetic acclimation: State transitions and adjustment of photosystem stoichiometry – functional relationships between short-term and long-term light quality acclimation in plants. *FEBS Journal* **275**, 1080–1088.

Domingos P. (2012) A few useful things to know about machine learning. *Communications of the ACM* **55**, 78–87.

Evans L.T. (1980) The natural history of crop yield: A combination of improved varieties of crop plants and technological innovations continues to increase productivity, but the highest yields are approaching limits set by biological constraints. *American Scientist* **68**, 388–397.

Fernández E., Llamas Á. & Galván A. (2009) *The Chlamydomonas Sourcebook*. Elsevier.

Finazzi G., Furia A., Barbagallo R.P. & Forti G. (1999) State transitions, cyclic and linear electron transport and photophosphorylation in Chlamydomonas reinhardtii. *Biochimica et Biophysica Acta (BBA) - Bioenergetics* **1413**, 117–129.

Fischer B.B., Wiesendanger M. & Eggen R.I.L. (2006) Growth condition-dependent sensitivity, photodamage and stress response of Chlamydomonas reinhardtii exposed to high light conditions. *Plant cell physiology* **47**, 1135–1145.

Fischer M. (2008) An algae bioreactor from recycled water bottles. *Instructables*.

Franck F., Juneau P. & Popovic R. (2002) Resolution of the Photosystem I and Photosystem {II} contributions to chlorophyll fluorescence of intact leaves at room temperature. *Biochimica et Biophysica Acta (BBA) - Bioenergetics* **1556**, 239–246.

Franklin B. (1961) Advice to a Young Tradesman, [21 July 1748]. In *The Papers of Benjamin Franklin, vol. 3, January 1, 1745, through June 30, 1750*. (ed L.W. Labaree), pp. 304–308. Yale University Press, New Haven.

Garling C. (2015) Racing towards a self-driving future. *Wired*. Retrieved from https://www.wired.com/brandlab/2015/04/racing-towards-self-driving-future/

Genty B., Briantais J.-M. & Baker N.R. (1989) The relationship between the quantum yield of photosynthetic electron transport and quenching of chlorophyll fluorescence. *Biochimica et Biophysica Acta (BBA) - General Subjects* **990**, 87–92.

Giordano M., Beardall J. & Raven J.A. (2005) CO 2 concentrating mechanisms in algae: mechanisms, environmental modulation, and evolution. *Annu. Rev. Plant Biol.* **56**, 99–131.

Goff S., Vaughn M., McKay S., Lyons E., Stapleton A., Gessler D., … Stanzione D. (2011) The iPlant collaborative: cyberinfrastructure for plant biology. *Frontiers in Plant Science* **2**, 34.

Golding A.J. & Johnson G.N. (2003) Down-regulation of linear and activation of cyclic electron transport during drought. *Planta* **218**, 107–114.

Goldschmidt-Clermont M. & Bassi R. (2015) Sharing light between two photosystems: mechanism of state transitions. *Current Opinion in Plant Biology* **25**, 71–78.

Google (2012, December 12) Google Cloud Platform. Retrieved from https://cloud.google.com/products/machine-learning/

Gorkom H.J. Van, Tamminga J.J. & Haveman J. (1974) Primary reactions, plastoquinone and fluorescence yield in subchloroplast fragments prepared with deoxycholate. *Biochimica et Biophysica Acta (BBA) - Bioenergetics* **347**, 417–438.

Govindjee (1995) Sixty-three years since Kautsky: Chlorophyll a fluorescence. *Functional Plant Biology* **22**, 131–160.

Hall C., Cruz J., Wood M., Zegarac R., DeMars D., Carpenter J., … Kramer D. (2013) Photosynthetic measurements with the IDEA spec: An integrated diode emitter array spectrophotometer/fluorometer. In *Photosynthesis Research for Food, Fuel and the Future SE - 38*. Advanced Topics in Science and Technology in China, pp. 184–188. Springer Berlin Heidelberg.

Healey F.P. (1977) Ammonium and urea uptake by some freshwater algae. *Canadian Journal of Botany* **55**, 61–69.

Hideg É., Spetea C. & Vass I. (1994) Singlet oxygen and free radical production during acceptor- and donor-side-induced photoinhibition. *Biochimica et Biophysica Acta (BBA) - Bioenergetics* **1186**, 143–152.

Hill R. & Bendall F.A.Y. (1960) Function of the two cytochrome components in chloroplasts: A working hypothesis. *Nature* **186**, 136–137.

Hughes W.S. (1928) On Haber's glass cell. *Journal of the Chemical Society*, 491–506.

Huisman J.E.F., Jonker R.R., Zonneveld C.O.R. & Weissing F.J. (1999) Competition for light between phytoplankton species: Experimental tests of mechanistic theory. *Ecology* **80**, 211–222.

Hundal T., Aro E.-M., Carlberg I. & Andersson B. (1990) *Restoration of light induced photosystem II inhibition without de novo protein synthesis*.

Irwin S. & Davenport J. (2002) Hyperoxic boundary layers inhabited by the epiphytic meiofauna of Fucus serratus. *Marine Ecology Progress Series* **244**, 73–79.

Jallet D., Caballero M.A., Gallina A.A., Youngblood M. & Peers G. (2016) Photosynthetic physiology and biomass partitioning in the model diatom Phaeodactylum tricornutum grown in a sinusoidal light regime. *Algal Research* **18**, 51–60.

Joliot P., Beal D. & Frilley B. (1980) A new spectrophotometric method for the study of photosynthetic reactions. *Journal de Chimie Physique et de Physicochimie Biologique* **77**, 209–216.

Joliot P. & Joliot A. (1984) Electron transfer between the two photosystems. I. Flash excitation under oxidizing conditions. *Biochimica et Biophysica Acta (BBA) - Bioenergetics* **765**, 210–218.

Kanazawa A. & Kramer D.M. (2002) In vivo modulation of nonphotochemical exciton quenching (NPQ) by regulation of the chloroplast ATP synthase. *Proceedings of the National Academy of Sciences of the United States of America* **99**, 12789–94.

Katoh S. & Takamiya A. (1964) Nature of copper-protein binding in spinach plastocyanin. *The Journal of Biochemistry* **55**, 378–387.

Kautsky H. & Hirsch A. (1931) Neue versuche zur kohlensäureassimilation. *Naturwissenschaften* **19**, 964.

Kiese S., Ebner H.G. & Onken U. (1980) A simple laboratory airlift fermentor. *Biotechnology Letters* **2**, 345–350.

Kitajima M. & Butler W.L. (1975) Quenching of chlorophyll fluorescence and primary photochemistry in chloroplasts by dibromothymoquinone. *Biochimica et Biophysica Acta (BBA) - Bioenergetics* **376**, 105–115.

Kliphuis A.M.J., Martens D.E., Janssen M. & Wijffels R.H. (2011) Effect of O(2) : CO(2) ratio on the primary metabolism of Chlamydomonas reinhardtii. *Biotechnology and bioengineering*.

Koch D.G., Borucki W.J., Basri G., Batalha N.M., Brown T.M., Caldwell D., … Wu H. (2010) Kepler mission design, realized photometric performance, and early science. *Astrophysical Journal Letters* **713**, L79–L86.

Kohzuma K., Dal Bosco C., Kanazawa A., Dhingra A., Nitschke W., Meurer J. & Kramer D.M. (2012) Thioredoxin-insensitive plastid ATP synthase that performs moonlighting functions. *Proceedings of the National Academy of Sciences* **109**, 3293–3298.

Kondo T., Johnson C.H. & Hastings J.W. (1991) Action spectrum for resetting the circadian phototaxis rhythm in the CW15 strain of Chlamydomonas: I. Cells in darkness. *Plant Physiology* **95**, 197–205.

Kramer D., Johnson G., Kiirats O. & Edwards G. (2004) New fluorescence parameters for the determination of Q(A) redox state and excitation energy fluxes. *Photosynthesis Research* **79**, 209–218.

Kramer D.M. & Crofts A.R. (1990) Demonstration of a highly-sensitive portable double-flash kinetic spectrophotometer for measurement of electron transfer reactions in intact plants. *Photosynthesis Research* **23**, 231–240.

Kramer D.M., Cruz J.A. & Kanazawa A. (2003) Balancing the central roles of the thylakoid proton gradient. *Trends in Plant Science* **8**, 27–32.

Kramer D.M. & Evans J.R. (2011) The importance of energy balance in improving photosynthetic productivity. *Plant Physiology* **155**, 70–78.

Kramer D.M. & Sacksteder C.A. (1998) A diffused-optics flash kinetic spectrophotometer (DOFS) for measurements of absorbance changes in intact plants in the steady-state. *Photosynthesis Research* **56**, 103–112.

Kramer D.M., Sacksteder C.A. & Cruz J.A. (1999) How acidic is the lumen? *Photosynthesis Research* **60**, 151–163.

Krieger-Liszkay A. (2005) Singlet oxygen production in photosynthesis. *Journal of experimental botany* **56**, 337–46.

Krieger A., Weis E. & Demeter S. (1993) Low-pH-induced Ca2+ ion release in the water-splitting system is accompanied by a shift in the midpoint redox potential of the primary quinone acceptor QA. *Biochimica et Biophysica Acta (BBA) - Bioenergetics* **1144**, 411–418.

Kuhlgert S., Austic G., Zegarac R., Osei-Bonsu I., Hoh D., Chilvers M.I., … others (2016) MultispeQ Beta: a tool for large-scale plant phenotyping connected to the open PhotosynQ network. *Royal Society Open Science* **3**, 160592.

L. Machta E.H. (1970) Atmospheric oxygen in 1967 to 1970. *Science* **168**, 1582–1584.

Lavergne J. & Trissl H.W. (1995) Theory of fluorescence induction in photosystem II: derivation of analytical expressions in a model including exciton-radical-pair equilibrium and restricted energy transfer between photosynthetic units. *Biophysical Journal* **68**, 2474–2492.

Lee D.Y. & Fiehn O. (2008) High quality metabolomic data for Chlamydomonas reinhardtii. *Plant Methods* **4**, 7.

Lehmann N., Rischer H., Eibl D. & Eibl R. (2013) Wave-mixed and orbitally shaken single-use photobioreactors for diatom algae propagation. *Chemie Ingenieur Technik* **85**, 197–201.

LI-COR Inc. (2016, May 14) LI-COR History. Retrieved from https://www.licor.com/corp/history.html

Liptay W. (1969) Electrochromism and solvatochromism. *Angewandte Chemie International Edition in English* **8**, 177–188.

Lucker B. & Kramer D.M. (2013) Regulation of cyclic electron flow in Chlamydomonas reinhardtii under fluctuating carbon availability. *Photosynthesis research* **117**, 449–59.

Lucker B.F., Hall C.C., Zegarac R. & Kramer D.M. (2014) The environmental photobioreactor (ePBR): An algal culturing platform for simulating dynamic natural environments. *Algal Research* **6**, **Part B**, 242–249.

Lund J.B., Blom T.J. & Aaslyng J.M. (2007) End-of-day lighting with different red/far-red ratios using light-emitting diodes affects plant growth of Chrysanthemum$\times$ morifolium Ramat.“Coral Charm.” *HortScience* **42**, 1609–1611.

Marc (2013) Culture your own phytoplankton. *Melev's Reef Inc.* Retrieved from http://www.melevsreef.com/node/1614

Marečková M., Barták M. & others (2016) Effects of short-term low temperature stress on chlorophyll fluorescence transients in Antarctic lichen species. *Czech Polar Reports* **6**, 54–65.

McMinn A., Pankowski A. & Delfatti T. (2005) Effect of hyperoxia on the growth and photosynthesis of polar sea ice microalgae. *Journal of Phycology* **41**, 732–741.

McPherson R.A., Fiebrich C.A., Crawford K.C., Kilby J.R., Grimsley D.L., Martinez J.E., … Sutherland A.J. (2007) Statewide monitoring of the mesoscale environment: A technical update on the Oklahoma mesonet. *Journal of Atmospheric and Oceanic Technology* **24**, 301–321.

Melis A. & Thielen A.P.G.M. (1980) The relative absorption cross-sections of Photosystem I and Photosystem II in chloroplasts from three types of Nicotiana tabacum. *Biochimica et Biophysica Acta (BBA) - Bioenergetics* **589**, 275–286.

Mesonet (2012, July 26). Retrieved from http://www.mesonet.org/

Michelet L., Zaffagnini M., Morisse S., Sparla F., Pérez-Pérez M.E., Francia F., … Lemaire S. (2013) Redox regulation of the Calvin–Benson cycle: something old, something new. *Frontiers in Plant Science* **4**, 470.

Microsoft (2016, November 27) Microsoft Azure. Retirieved from https://azure.microsoft.com/en-us/services/machine-learning/

Mirsky A.E. & Anson M.L. (1929) A description of the glass electrode and its use in measuring hydrogen ion concentration. *Journal of Biological Chemistry* **81**, 581–587.

Mittag M. (1996) Conserved circadian elements in phylogenetically diverse algae. *Proceedings of the National Academy of Sciences* **93**, 14401–14404.

Mittag M., Kiaulehn S. & Johnson C.H. (2005) The circadian clock in Chlamydomonas reinhardtii. What is it for? What is it similar to? *Plant Physiology* **137**, 399–409.

Mockler T., Yang H., Yu X., Parikh D., Cheng Y., Dolan S. & Lin C. (2003) Regulation of photoperiodic flowering by Arabidopsis photoreceptors. *Proceedings of the National Academy of Sciences* **100**, 2140–2145.

Moenne-Loccoz P., Heathcote P., Maclachlan D.J., Berry M.C., Davis I.H. & Evans M.C.W. (1994) Path of electron transfer in Photosystem 1: Direct evidence of forward electron transfer from A1 to Fe-SX. *Biochemistry* **33**, 10037–10042.

Moroney J. V & Tolbert N.E. (1985) Inorganic carbon uptake by Chlamydomonas reinhardtii. *Plant Physiology* **77**, 253–258.

Moroney J. V, Wilson B.J. & Tolbert N.E. (1986) Glycolate metabolism and excretion by Chlamydomonas reinhardtii. *Plant physiology* **82**, 821–6.

Morton J.F. (2007) The impact of climate change on smallholder and subsistence agriculture. *Proceedings of the National Academy of Sciences* **104**, 19680–19685.

Müller P., Li X.-P. & Niyogi K.K. (2001) Non-photochemical quenching. A response to excess light energy. *Plant Physiology* **125**, 1558–1566.

Munro W.A., Thomas C.L.P., Simpson I., Shaw J. & Dodgson J. (1996) Deterioration of pH electrode response due to biofilm formation on the glass membrane. *Sensors and Actuators B: Chemical* **37**, 187–194.

Murchie E.H. & Niyogi K.K. (2011) Manipulation of photoprotection to improve plant photosynthesis. *Plant physiology* **155**, 86–92.

Do Nascimento M., Sanchez Rizza L., Arruebarrena Di Palma A., Dublan M. de los A., Salerno G., Rubio L.M. & Curatti L. (2015) Cyanobacterial biological nitrogen fixation as a sustainable nitrogen fertilizer for the production of microalgal oil. *Algal Research* **12**, 142–148.

Nawrocki W.J., Santabarbara S., Mosebach L., Wollman F.-A. & Rappaport F. (2016) State transitions redistribute rather than dissipate energy between the two photosystems in Chlamydomonas. *Nature Plants* **2**, 16031.

Negi S., Barry A.N., Friedland N., Sudasinghe N., Subramanian S., Pieris S., … Sayre R. (2016) Impact of nitrogen limitation on biomass, photosynthesis, and lipid accumulation in Chlorella sorokiniana. *Journal of Applied Phycology* **28**, 803–812.

Nicholls D.G. (1974) The influence of respiration and ATP hydrolysis on the proton-electrochemical gradient across the inner membrane of rat-liver mitochondria as determined by ion distribution. *European Journal of Biochemistry* **50**, 305–315.

Ort D.R. & Melis A. (2011) Optimizing antenna size to maximize photosynthetic efficiency. *Plant physiology* **155**, 79–85.

Osprey S., Barnett J., Smith J., Adamson P., Andreopoulos C., Arms K.E., … Zwaska R. (2009) Sudden stratospheric warmings seen in MINOS deep underground muon data. *Geophysical Research Letters* **36**, L05809

Pandey J.K. & Gopal R. (2012) Dimethoate-induced slow S to M chlorophyll a fluorescence transient in wheat plants. *Photosynthetica* **50**, 630–634.

Park S.-Y. & Subbarao M. (2005) A multiview 3D modeling system based on stereo vision techniques. *Machine Vision and Applications* **16**, 148–156.

Peltier G. & Cournac L. (2002) Chlororespiration. *Annual Review of Plant Biology* **53**, 523–550.

Peng L., Lan C.Q. & Zhang Z. (2013) Evolution, detrimental effects, and removal of oxygen in microalga cultures: A review. *Environmental Progress & Sustainable Energy* **32**, 982–988.

Penttinen J.T. (2015) Wired Connectivity. In *The Telecommunications Handbook: Engineering Guidelines for Fixed, Mobile, and Satellite Systems*, 1st ed. pp. 105–114. John Wiley & Sons, Ltd., Chichester, United Kingdom.

Perrine Z., Negi S. & Sayre R.T. (2012) Optimization of photosynthetic light energy utilization by microalgae. *Algal Research* **1**, 134–142.

Pfündel E. (1998) Estimating the contribution of Photosystem I to total leaf chlorophyll fluorescence. *Photosynthesis Research* **56**, 185–195.

Phillips R.L. (2010) Mobilizing science to break yield barriers. **50**, S-99-S-108.

Photon Systems Instruments Photobioreactors (2016, November 27). Retrieved from http://psi.cz/products/photobioreactors/

Polle J.E.W., Kanakagiri S., Jin E., Masuda T. & Melis A. (2002) Truncated chlorophyll antenna size of the photosystems—a practical method to improve microalgal productivity and hydrogen production in mass culture. *International Journal of Hydrogen Energy* **27**, 1257–1264.

Pulz O. (2001) Photobioreactors: production systems for phototrophic microorganisms. *Applied Microbiology and Biotechnology* **57**, 287–293.

Raven B.J.A., Johnston A.M., Parsons R. & Kübler J. (1994) The influence of natural and experimental high O2 concentrations on O2-evolving phototrophs. *Biological Reviews* **69**, 61–94.

Roach T., Na C.S. & Krieger-Liszkay A. (2015) High light-induced hydrogen peroxide production in Chlamydomonas reinhardtii is increased by high CO2 availability. *The Plant journal : for cell and molecular biology* **81**, 759–66.

Roberty S., Bailleul B., Berne N., Franck F. & Cardol P. (2014) PSI Mehler reaction is the main alternative photosynthetic electron pathway in Symbiodinium sp., symbiotic dinoflagellates of cnidarians. *New Phytologist* **204**, 81–91.

Rochaix J.-D. (2011) Regulation of photosynthetic electron transport. *Biochimica et Biophysica Acta (BBA) - Bioenergetics* **1807**, 375–383.

Rodolfi L., Chini Zittelli G., Bassi N., Padovani G., Biondi N., Bonini G. & Tredici M.R. (2009) Microalgae for oil: Strain selection, induction of lipid synthesis and outdoor mass cultivation in a low-cost photobioreactor. *Biotechnology and Bioengineering* **102**, 100–112.

Sacksteder C.A., Jacoby M.E. & Kramer D.M. (2001) A portable, non-focusing optics spectrophotometer (NoFOSpec) for measurements of steady-state absorbance changes in intact plants. *Photosynthesis Research* **70**, 231–240.

Satagopan S. & Spreitzer R.J. (2008) Plant-like substitutions in the large-subunit carboxy terminus of Chlamydomonas Rubisco increase CO2/O2 specificity. *BMC Plant Biology* **8**, 85.

Schreiber U., Schliwa U. & Bilger W. (1986) Continuous recording of photochemical and non-photochemical chlorophyll fluorescence quenching with a new type of modulation fluorometer. *Photosynthesis Research* **10**, 51–62.

Sharma P., Jha A.B., Dubey R.S. & Pessarakli M. (2012) Reactive oxygen species, oxidative damage, and antioxidative defense mechanism in plants under stressful conditions. *Journal of Botany* **2012**.

Sicora C., Máté Z. & Vass I. (2003) The interaction of visible and UV-B light during photodamage and repair of Photosystem II. *Photosynthesis Research* **75**, 127–137.

Soletto D., Binaghi L., Lodi A., Carvalho J.C.M. & Converti A. (2005) Batch and fed-batch cultivations of Spirulina platensis using ammonium sulphate and urea as nitrogen sources. *Aquaculture* **243**, 217–224.

Spalding E.P. & Miller N.D. (2013) Image analysis is driving a renaissance in growth measurement. *Current Opinion in Plant Biology* **16**, 100–104.

Spalding M.H. (1990) Effect of photon flux density on inorganic carbon accumulation and net CO2 exchange in a high-CO2-requiring mutant of Chlamydomonas reinhardtii. *Photosynthesis Research* **24**, 245–252.

Spetea C. & Schoefs B. (2010) Solute transporters in plant thylakoid membranes: Key players during photosynthesis and light stress. *Communicative & Integrative Biology* **3**, 122–129.

Spurgeon C.E. (2000) *Ethernet: The Definitive Guide*, 1st ed. (eds M. Stone & C. Toporek), O'Reilly Media, Inc., Sebastopol, California.

Stirbet A. & Govindjee (2011) On the relation between the Kautsky effect (chlorophyll a fluorescence induction) and Photosystem II: Basics and applications of the OJIP fluorescence transient. *Journal of photochemistry and photobiology. B, Biology* **104**, 236–57.

Su Y., Mennerich A. & Urban B. (2011) Municipal wastewater treatment and biomass accumulation with a wastewater-born and settleable algal-bacterial culture. *Water Research* **45**, 3351–3358.

Subramanyam R., Jolley C., Brune D.C., Fromme P. & Webber A.N. (2006) Characterization of a novel Photosystem I–LHCI supercomplex isolated from Chlamydomonas reinhardtii under anaerobic (State II) conditions. *FEBS Letters* **580**, 233–238.

Sueoka N. (1960) Mitotic replication of deoxyribonucleic acid in Chlamydomonas reinhardi. *Proceedings of the National Academy of Sciences* **46**, 83–91.

Suetlemeyer D., Biehler K. & Fock H.P. (1993) Evidence for the contribution of pseudocyclic photophosphorylation to the energy requirement of the mechanism for concentrating inorganic carbon in Chlamydomonas. *Planta (Heidelberg)* **189**, 235–242.

Sullivan B.L., Aycrigg J.L., Barry J.H., Bonney R.E., Bruns N., Cooper C.B., … others (2014) The eBird enterprise: an integrated approach to development and application of citizen science. *Biological Conservation* **169**, 31–40.

Suorsa M., Järvi S., Grieco M., Nurmi M., Pietrzykowska M., Rantala M., … Aro E.-M. (2012) PROTON GRADIENT REGULATION5 is essential for proper acclimation of Arabidopsis Photosystem I to naturally and artificially fluctuating light conditions. *The Plant Cell* **24**, 2934–2948.

Suzuki L. & Johnson C.H. (2001) Algae know the time of day: Circadian and photoperiodic programs. *Journal of Phycology* **37**, 933–942.

Takahashi Y. & Katoh S. (1982) Functional subunit structure of photosystem 1 reaction center in Synechococcus sp. *Archives of Biochemistry and Biophysics* **219**, 219–227.

Tamburic B., Guruprasad S., Radford D.T., Szabó M., Lilley R.M., Larkum A.W.D., … others (2014) The effect of diel temperature and light cycles on the growth of Nannochloropsis oculata in a photobioreactor matrix. *PloS one* **9**, e86047.

Tcherkez G. (2016) The mechanism of Rubisco-catalysed oxygenation. *Plant, cell & environment* **39**, 983–997.

Tietz S., Hall C.C., Cruz J.A. & Kramer D.M. (2017) NPQ(T): a chlorophyll fluorescence parameter for rapid estimation and imaging of non-photochemical quenching of excitons in photosystem II associated antenna complexes. *Plant Physiology* **In press**.

Triantaphylidès C., Krischke M., Hoeberichts F.A., Ksas B., Gresser G., Havaux M., … Mueller M.J. (2008) Singlet oxygen is the major reactive oxygen species involved in photooxidative damage to plants. *Plant physiology* **148**, 960–8.

Trissl H.-W. (1997) Determination of the quenching efficiency of the oxidized primary donor of Photosystem I, P700+: Implications for the trapping mechanism. *Photosynthesis Research* **54**, 237–240.

Truchot J.P. & Duhamel-Jouve A. (1980) Oxygen and carbon dioxide in the marine intertidal environment: diurnal and tidal changes in rockpools. *Respiration physiology* **39**, 241–54.

Uchida K., Kudo T., Suzuki K.-I. & Nakase T. (1999) A new rapid method of glycolate test by diethyl ether extraction, which is applicable to a small amount of bacterial cells of less than one milligram. *The Journal of general and applied microbiology* **45**, 49–56.

Valeur B. (2001) Introduction: On the origin of the terms fluorescence, phosphorescence, and luminescence. In *New Trends in Fluorescence Spectroscopy: Applications to Chemical and Life Sciences*. (eds B. Valeur & J.-C. Brochon), pp. 3–6. Springer Berlin Heidelberg, Berlin, Heidelberg.

Velthuys B.R. & Amesz J. (1974) Charge accumulation at the reducing side of system 2 of photosynthesis. *Biochimica et Biophysica Acta (BBA) - Bioenergetics* **333**, 85–94.

Vredenberg W. & Pavlovič A. (2013) Chlorophyll a fluorescence induction (Kautsky curve) in a Venus flytrap (Dionaea muscipula) leaf after mechanical trigger hair irritation. *Journal of Plant Physiology* **170**, 242–250.

Van Wagenen J., Pape M.L. & Angelidaki I. (2015) Characterization of nutrient removal and microalgal biomass production on an industrial waste-stream by application of the deceleration-stat technique. *Water Research* **75**, 301–311.

Wang Y.-P. & Leuning R. (1998) A two-leaf model for canopy conductance, photosynthesis and partitioning of available energy I:: Model description and comparison with a multi-layered model. *Agricultural and Forest Meteorology* **91**, 89–111.

Weaver J.C. (1995) Electroporation theory. In *Plant Cell Electroporation and Electrofusion Protocols*. (ed J.A. Nickoloff), pp. 3–28. Springer New York, Totowa, NJ.

Whitmarsh J. & Govindjee (1999) The Photosynthetic Process. In *Concepts in Photobiology*. (eds G.S. Singhal, G. Renger, S.K. Sopory & K.-D. Irrgang), pp. 11–51. Springer Netherlands, Dordrecht.

Witt H.T.T. (1979) Energy conversion in the functional membrane of photosynthesis. Analysis by light pulse and electric pulse methods: The central role of the electric field. *Biochimica et Biophysica Acta (BBA) - Reviews on Bioenergetics* **505**, 355–427.

Wollman F.A. (2001) State transitions reveal the dynamics and flexibility of the photosynthetic apparatus. *The EMBO journal* **20**, 3623–30.

Yokthongwattana K. & Melis A. (2008) Photoinhibition and recovery in oxygenic photosynthesis: mechanism of a photosystem II damage and repair cycle. In *Photoprotection, photoinhibition, gene regulation, and environment*. (eds B. Demmig-Adams, W.W. Adams & A.K. Mattoo), pp. 175–191. Springer.

Zhu X.-G., Song Q. & Ort D.R. (2012) Elements of a dynamic systems model of canopy photosynthesis. *Current Opinion in Plant Biology* **15**, 237–244.